Optical Sources for Atomic Sensors

James Peter Kenneth Meiklejohn

A thesis presented for the degree of
Doctor of Philosophy

Cardiff University School of Physics and Astronomy
July 2025

Optical Sources for Atomic Sensors

Developing laser light sources for high-precision measurement applications

Abstract

This thesis presents work on novel Vertical Cavity Surface Emitting Laser (VCSEL) devices intended to better meet the application requirements of miniature atomic sensors. Atomic sensors require a laser light source that meets a number of specifications that are difficult to achieve with conventional VCSEL designs, requiring particular optical output power, polarisation stability, and Side-Mode Suppression Ratio (SMSR).

Increased optical power can be obtained by using arrays of multiple individual emitters. Optically coupling multiple single-mode cavities together is an approach that can scale the total single-mode output power, and results are presented from designs intended to achieve lateral optical coupling. Attempts to use angled ends to contain light in an in-plane mode between the emitters with a total internal reflection condition resulted in a small power change (less than 1% of the total optical power) indicating that there is a weak interaction between some pairs of emitters with a centre-centre distance of $12\,\mu\text{m}$. Material and fabrication variations lead to differences between the emission wavelengths of closely-spaced emitters, which makes fabricating laterally coupled emitters challenging, and the effects of these variations are quantified.

Conventional VCSELs use an oxide aperture to laterally define the optical cavity, but a defect in a photonic crystal structure can also be used to define the cavity, providing a different method for optical confinement that potentially supports a larger aperture size and so higher single-mode optical output power. Measurements from photonic crystal devices are presented, showing an increase in the single-mode aperture size to $4.25\,\mu\text{m}$, compared to $3\,\mu\text{m}$ for an oxide-confined device.

Multiphysics simulation of a VCSEL gives insight into the internal mechanisms that determine the operation and performance of a device. Simulations are used as a design tool to determine the effects of design changes, and to develop an understanding of the dominant mechanisms. Using the Harold VCSEL software package a simulation of a VCSEL is set up and validated by comparison with experimental results. It was found that modifications are required to the model to accurately represent the thermal resistance of VCSELs, as bulk material thermal conductivity values result in an underestimate of the thermal resistance by an order of magnitude in the vertical direction due to the effect of phonon scattering at material interfaces.

The high-temperature performance of VCSELs is shown to depend on the aperture size. Smaller emitters are shown to have better power conversion efficiency at elevated temperatures and higher turn-off temperatures than larger ones. This motivates the use of small apertures in arrays of VCSELs, and arrays of small emitters are shown to have favourable power scaling properties. The thermal conductivity per emitter goes from 0.21 to $0.17\,\mathrm{mW\,K^{-1}}$ when scaling from 1 to 4 emitters, suggesting that arrays of emitters defined in this way represent a viable route for scaling to higher optical output power.

Acknowledgements

I would like to thank the industrial sponsors of the project at NPL for funding and motivating this research. At Photon Design, I am grateful to Dominic, Joel, and Andrew for their support and discussions on the use of the Harold software. Thanks to the ICS team for all the assistance and training provided in the cleanroom, and to Terri and Sarah on the CDT.

Special thanks to Jack, Craig, Curtis, Rich, Dagmar, and Sai, for their help with experiments and data analysis. My thanks to Curtis for many insightful discussions about the inner workings of VCSELs, and to Craig, Jack, and Rich for assistance with the probe station which carried out many of the measurements in this thesis, and to Sara and Zhongming for their support in the cleanroom.

I will remember fondly everyone who made spending time in the TRH more entertaining, with many enriching and intellectually stimulating discussions taking place in the 2nd floor kitchen, among others, Arthur, Ben, Ben, Davey, Franco, Joseph, Kate, Katie, Kimberly, Laura, Rachel, and Wesley.

Thanks also go to my friends and housemates who helped make Cardiff a home over the past five years, and to the running and cycling communities who provided balance, (which occasionally tipped away from physics). I am grateful to Julia for her patience and flexibility with deadlines, and to my family for their unwavering support and encouragement over many years.

Finally, heartfelt thanks to Sam for enduring the presence of a very distracted student, and for offering the steadfast support, encouragement, and belief that helped bring this thesis to completion.

Contents

Glossary of terms

AlGaAs	Aluminium Gallium Arsenide
BCB	Benzocyclobutene
CSAC	Chip Scale Atomic Clock
CSC	Compound Semiconductor Centre
CTLM	Circular Transfer Length Method
CW	Continous Wave
DBR	Distributed Bragg Reflector
EEL	Edge-Emitting Laser
FCA	Free Carrier Absorption
FP	Fabry-Perot
GaAs	Gallium Arsenide
GNSS	Global Navigation Satellite System
HCG	High Contrast Grating
ICP	Inductively Coupled Plasma
ICS	Institute for Compound Semiconductors
IV	Current Voltage
IVBA	Inter Valence Band Absorption
HE	Hybrid Electric

LiDAR	Light Detection and Ranging
LI	Light-Current
LIV	Light-Current-Voltage
LR	Inductance Resistance
NPL	National Physical Laboratory
MBE	Molecular Beam Epitaxy
MOVPE	Metal-Organic Vapour Phase Epitaxy
PCE	Power Conversion Efficiency
PCSEL	Photonic Crystal Surface Emitting Laser
PVD	Physical Vapour Deposition
QW	Quantum Well
RIE	Reactive Ion Etch
RF	Radio Frequency
SCH	Separate Confinement Heterostructure
SEM	Scanning Electron Microscope
SIMS	Secondary Ion Mass Spectrometry
SMSR	Side-Mode Suppression Ratio
SRH	Shockley-Read-Hall
TE	Transverse Electric
TMM	Transfer Matrix Method
VCSEL	Vertical Cavity Surface Emitting Laser
VECSEL	Vertical Extended Cavity Surface Emitting Laser
VQF	VCSEL Quick Fabrication

Chapter 1

Background and motivation

1.1 Project aims

An atomic sensor uses the physical properties of atoms as a reference to enable high-precision metrology. The electronic transitions of the single valence electron in an alkali metal vapour can be used as a frequency standard or to measure rotation or magnetic field strength, due to the influence of the external environment on the energy levels of the electronic states of the electron. Atomic sensors are used for a diverse range of applications in communications, medical imaging, non-destructive testing, satellites, and navigation, and there is great interest in making atomic sensors smaller and more power-efficient as well as lower-cost to enable their use in a greater range of applications.

In an atomic magnetometer, a laser light source is required to excite and probe the energy levels of the electrons in the metal vapour. This source needs to have properties including optical power output greater than 1 mW, stable single-mode operation, narrow linewidth, long-term reliability, and high temperature operating. Vertical-cavity surface-emitting lasers (VCSELs) are of interest for this application because of their small size, circular beam profile, relative ease of fabrication, and possibility of polarisation-controlled single-mode operation.

A VCSEL is a type of semiconductor diode laser. Figure 1.1 shows how in a VCSEL an optical cavity is defined with epitaxially grown Bragg mirrors, and an oxide aperture controls where current is injected into the active region. The aim of the work carried out in this project is to develop novel VCSEL designs that better meet the application requirements of atomic clocks.

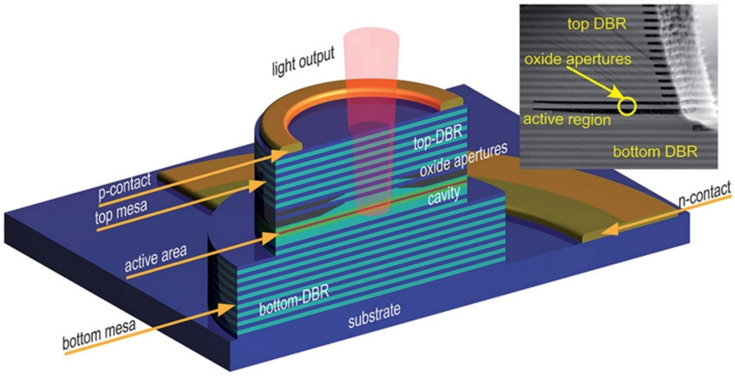

Figure 1.1: A typical oxide-confined VCSEL structure, from [1].

1.2 Atomic sensors

Since 1967 the SI second has been defined as 9192631770 periods of the ground state hyperfine transition of caesium [2], and this definition is used to define further units such as distance and mass [3]. Historically, this transition was measured using a resonant microwave cavity, which at the D1 transition frequency of 9.6 GHz has a minimum size of several centimetres [4]. Atomic magnetometers detect the Larmor precession of atoms in a magnetic field, which is a radio-frequency signal that depends on the field strength and orientation.

Different vapour cell configurations and buffer gases result in a complex relationship between the properties of the laser and the accuracy of the sensor. However, but in general, the linewidth and power are regarded as among the main obstacles to the improved performance of optical sensors. VCSELs were first used for atomic sensor applications in 2000 [5] by researchers at Sandia National Laboratories, and are widely recognised as the route to miniaturised devices over other types of lasers despite their lower output powers [4]. In 2007, the Chip-Scale Atomic Clock (CSAC) became commercially available [6]. Miniature atomic clocks have particular use for maintaining timekeeping in the event of a Global Navigation Satellite System (GNSS) outage, and are being developed for this application in the UK supply chain [7].

There is interest in a range of applications for the deployment of miniature atomic magnetometers, such as the detection of defects in metallic objects [8], as a new avenue for medical imaging through the analysis of electrical signals in the human brain and body (magnetoencephalography) [9], and the remote detection of chemicals through the detection of nuclear resonances [8]. An example of an experimental miniature magnetometer is shown in Figure 1.2, and it can be seen that a large part of the volume of the device is the optical elements.

Edge-emitting lasers have also been investigated for atomic sensor applications, but these devices are significantly larger with much higher power requirements [10][11]. High-performance optical sensors that are not constrained by size often use external-cavity diode lasers, which can achieve much lower linewidths than VCSELs, but these are larger and have complex mechanical alignment requirements [12]. VCSELs are therefore the preferred type of optical source for applications where size, weight and power (SWaP) are critical [13].

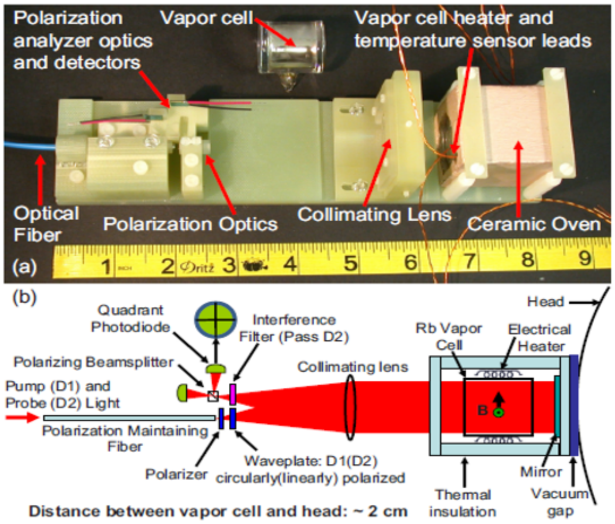

Figure 1.2: View and schematic of a miniature optical magnetometer, from [14].

The optical wavelength required from the laser is due to the atomic species used in the vapour cell of the atomic sensor, and for caesium, the two relevant wavelengths are 894.6 nm and 852.2 nm, corresponding to the D1 and D2 transitions [11]. The key requirements are the output wavelength, optical power, threshold current, and beam profile. The specifications are met marginally by currently produced VCSELs but the yield of devices that meet the specification is low, which increases cost and manufacturing complexity and presents a barrier to widespread use of optical sensors.

Recent work to design VCSELs for atomic sensors has been carried out by groups at Sandia National Labs [15], Ulm University [16], Institute of Semiconductors at the Chinese Academy of Sciences [17] as well as at Cardiff University, through the MagV, MacV, Kairos, and QFoundry projects [18]. These projects have highlighted the need to improve VCSEL performance, namely single mode power, which will improve the yield of devices that meet the application requirements. The emission wavelength is particularly critical for atomic sensor applications, and challenges on the yield of material at the target wavelength are due to limitations in the epitaxial growth [19].

1.3 Historical development of diode lasers

The semiconductor diode laser was developed simultaneously and independently by several different groups at IBM, General Electric and MIT in 1962 [20]. Much-improved performance was achieved with the double-heterostructure to reduce diffusion carriers out of the active region [21], and then the use of quantum confinement to localise carriers in the active region [22]. The first VCSEL was realised in 1979 by Iga at the Tokyo Institute of Technology [23][24]. Oxide confinement provides a means of controlling the flow of current to the active region of the device and so greatly improves the performance, and the first oxide-confined VCSEL was produced in 1994 [25]. Commercial applications followed with the use of VCSELs in short-range telecommunications, for CD players, and in short-range Light Detection and Ranging (LiDAR) applications such as for face detection in mobile phones [26]. Figure 1.3 shows a view of the VCSEL array used for the FaceID system in an Apple iPhone. VCSELs are most commonly produced in the 750 to 980 nm wavelength range using the GaAs-AlGaAs material system, but have also been created with longer wavelengths using dilute nitride (GaInNAs) quantum wells on GaAs, and InAlGaAsP on InP [27].

VCSELs are now used in applications as varied as 3D imaging [28], gas sensing [29], optical communications, and as non-linear systems in neural networks [30]. Many thousands of VCSELs can be manufactured and tested on a single wafer which makes them particularly suitable for a range of low-cost high-volume applications.

The edge-emitting laser (EEL) is the most widely used diode laser configuration. In an EEL, light is emitted out of a facet at the end of an optical cavity that is typically hundreds of microns long, which gives much higher optical powers due to the larger active region. This configuration makes the fabrication,

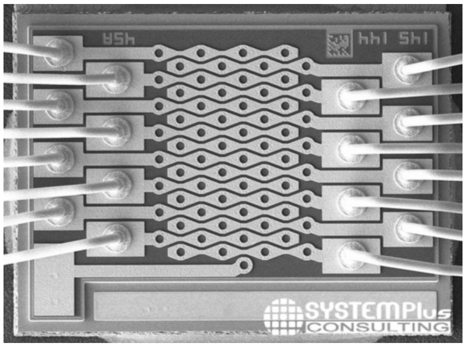

Figure 1.3: The VCSEL array from an iPhone, from System Plus Consulting [31].

testing, and integration more challenging compared to a VCSEL, due to the need to separate devices into bars to expose the facet, whereas VCSELs can be tested on-wafer. Photonic-crystal surface-emitting lasers (PCSELs) use in-plane amplification of light, which is outcoupled to vertical emission using a photonic crystal structure [32]. PCSELs provide higher single-mode output powers than VCSELs due to the larger active area, but at present, have significantly lower power conversion efficiencies than VCSELs or EELs [33].

1.4 Enhanced optical output power

The single-mode optical output power of a conventional oxide-confined VCSEL is limited by the maximum size of the aperture that will support only a single optical mode, and the small size of the device limits the maximum optical output power to a few milliwatts due to the effect of self-heating. Increasing the optical output power can be achieved by suppressing the lasing of higher-order modes, using arrays of individual emitters, or having multiple active regions by recycling carriers with tunnel junctions [34][35].

VCSEL arrays are a way to scale the output power of individual emitters, and arrays of VCSELs are used for applications such as illumination for LiDAR applications and materials processing. Output power densities of 2 to 5 $\mathrm{W\,mm^{-2}}$ are possible, with power conversion efficiencies (PCE) of over 50% [36]. Lateral coupling of multiple emitters is an approach that could give enhanced single-wavelength output power compared to single-emitter designs, and a number of different methods have been proposed to achieve coupling, using the evanescent part of the mode with emitters spaced close together or using guiding elements to guide the light [37].

A surface-relief can be used to introduce a mode-dependent loss. Material is etched off the cap layer to selectively vary the reflectivity of the mirror, increasing the loss of higher-order modes so as to prevent them from lasing. A cap etch can be used in conjunction with a grating to provide control of the polarisation [38].

Disorder-defined apertures use zinc diffused into the top mirror to define a region with lower optical reflectivity and higher free carrier absorption. This selectively suppresses the lasing of higher order modes compared to the fundamental mode, allowing larger oxide aperture sizes and measured single-mode optical output powers of 10 mA [39]. Photonic crystals are a different way of defining the refractive index profile to achieve optical confinement. In a photonic crystal, periodic changes in the refractive index give rise to a photonic stopband analogous to the stopband in a semiconductor material [40]. In a photonic crystal VCSEL, etched holes are used to define regions where the mode will and will not propagate, increasing the size of the aperture that can will support only a single lasing mode [41][42].

A stacked junction VCSEL consists of multiple active regions separated by tunnel junctions that recycle the carriers. This type of device has been commercialised at wavelengths at 980 nm for LIDAR applications [43], and studied at wavelengths including 850 nm [44]. The longer photon lifetime that arises from the larger size of the cavity compared to a conventional VCSEL suggests that these devices may also have favourable linewidth properties. Such devices also achieve excellent power conversion efficiency, with pulsed-power values of over 70% being reported, compared to less than 50% for conventional VCSEL designs [45].

1.5 Software simulation for understanding the physics

Due to the long turnaround time for growing, fabricating, and testing novel device designs, simulation tools are widely used for designing VCSEL structures. The physics of a laser device can be described by a series of coupled rate and continuity equations that describe the movement of carriers (holes and electrons), heat, and the profile of the optical field. Simulation codes are used to understand the dominant physical mechanisms in different operating regimes of the device, to predict the effect of design changes on the performance of the device, as well as to estimate the sensitivity of the performance to fabrication variations.

A number of codes are used for diode laser and for VCSEL simulation. There are commercially available codes such as COMSOL (Ansys), Crosslight (Crosslight Software) and Harold (Photon Design), and academic codes such as VENUS [46]. Different models are used for simulating the internal physics, and representing these in a numerical format requires approximations to make solving the equations tractable with the available computational resources. The physical parameters that describe these models, and the material properties of the semiconductor alloys, come from measurements presented in the literature. Parameters can also be found by optimising the fit between experimental results and simulation outputs [47][48].

1.6 Thesis structure

The aim of this thesis is to explore approaches to VCSEL design that better meet the application requirements for atomic sensors. Chapter 2 introduces the fundamental concepts of diode lasers and VCSELs in particular. Chapter 3 outlines the experimental methods used to design and fabricate devices and measure their characteristics.

Chapter 4 discusses the performance of novel VCSEL designs, exploring approaches that use lateral coupling, small arrays, and photonic crystal VCSEL to increase the maximum optical output power and aperture size of emitters. Chapter 5 discusses the use of a simulation code with VCSELs, showing how the simulation is set up and the sensitivity of a comparison between simulations and measurements to fabrication variations. Chapter 6 discusses the high-temperature performance of VCSELs, showing that at high temperatures small apertures have better performance, and showing that this effect is replicated in a simulation, and how this justifies the use of small emitters in an array. Chapter 7 discusses the conclusions and future work.

Chapter 2

Laser and VCSEL fundamentals

2.1 Basic operation of a laser

In a laser, optical amplification of light by means of stimulated emission in an optical cavity is used to produce coherent light, which has many useful properties. Stimulated emission occurs when a photon interacts with an excited state, leading to the emission of another photon with the same frequency, phase, and direction. An optical cavity can be used to reflect and contain an optical field so that it is repeatedly amplified. A mode of an optical cavity is a solution of Maxwell's equations that satisfies a round-trip condition in the cavity, so that light is reflected back in-phase with the same spatial profile. An optical mode contained in a cavity can be repeatedly amplified by stimulated emission to produce laser light, and the threshold gain condition describes the level of amplification required for a mode to overcome the mirror losses from the cavity and lase. The threshold gain g_{th} is given by

$$g_{\mathrm{th}} = -\frac{1}{2L_{\mathrm{g}}} \ln(R_1 R_2) \tag{2.1}$$

where L_g is the length of the gain medium and R_1 and R_2 are the mirror reflectivities. Gain in a laser media is due to population inversion, where higher-energy states are more likely to be occupied than lower-energy ones. This non-equilibrium condition is achieved by the electrical or optical injection of carriers into the gain region.

2.1.1 Electronic states of a semiconductor

A semiconductor crystal is a periodic structure, made of a single element (such as Si or Ge) or with two or more elements in the case of a compound semiconductor (such as GaAs or AlGaAs). In the periodic potential in a semiconductor crystal lattice, the solutions to Schroedinger's equation that describe the electron wavefunction are given by Bloch functions, which have the form

$$u(\vec{k}, \vec{r})e^{\vec{k}\cdot\vec{r}} \tag{2.2}$$

where $\vec{r}$ is the position, and $\vec{k}$ is the wavevector of the electron. The Bloch functions have the same translational symmetry as the crystal lattice. There are multiple solutions of the wavefunction for a given $\vec{k}$, corresponding to different energy bands within the structure. The function $E_{\mathrm{n}}(\vec{k})$ is the dispersion relation for an energy band and describes the energy as a function of $\vec{k}$ for a band denoted by n. The simplified band diagram of a direct-bandgap semiconductor such as GaAs is shown in Figure 2.1.

An electron in the valence band can be excited into the conduction band, where it is able to conduct, leaving behind a vacant state in the valence band known as a hole, that acts as a positively charged carrier. The conduction and valence bands are separated by the bandgap energy E_{g} and there are no energy states within this energy gap. The carrier concentration in a semiconductor can be increased by introducing dopant atoms with a different number of valence electrons, which increases the electrical conductivity. In an intrinsic (undoped) semiconductor at equilibrium the concentration of electrons and holes are equal. N-dopants introduce additional electrons into the conduction band band, and p-dopants increase the concentration of holes in the valence band.

Carriers respond to forces differently in the crystal lattice to how they would in a vacuum, and this is captured by the effective mass, denoted m^*. A parabolic band structure approximation can be used to describe the dispersion relation around $k = 0$ in direct-bandgap semiconductors, where the minimum in the conduction band and the maximum in the valence band line up. The effective mass of a carrier determines its mobility, which is a measure of the average (drift) velocity of the carrier under the influence of an electron field. The parabolic band approximation is given by

$$E(\mathbf{k}) = E_0 + \frac{\hbar^2\mathbf{k}^2}{2m^*} \tag{2.3}$$

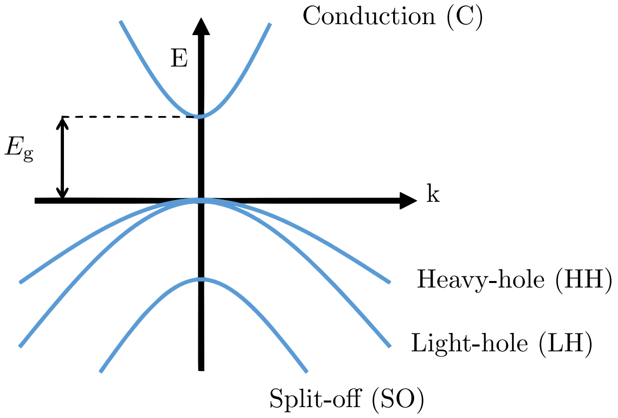

Figure 2.1: A simplified band structure of a direct-bandgap semiconductor, showing the conduction band and the the heavy-hole, light-hole, and split-off band. The energy difference between the conduction and valence bands is the bandgap E_{g}. Adapted from [49].

2.1.2 Diode structure

In thermal equilibrium, the occupation probability of an energy level is given by the Fermi-Dirac distribution. The Fermi-Dirac distribution is given by

$$f(E) = \frac{1}{1 + e^{\frac{(E - E_{\mathrm{F}})}{k_{\mathrm{b}} T}}} \tag{2.4}$$

where E_{f} is the Fermi energy, E is the energy of the state, k_{b} is the Boltzmann constant and T is the temperature. The function gives the occupation probability of an electron at a particular state with energy E. Holes are unoccupied electron states, so its probability distribution is given by $1 - f(E)$. The Fermi level is the energy at which a hypothetical state has a 50% chance of being occupied, and is the energy required to add one electron to the body. At thermal equilibrium, the Fermi level is the same throughout the structure.

Optical gain requires population inversion, where the carriers are more likely to be in the conduction band rather than the valence band, so that an incident photon is more likely to induce stimulated emission rather than absorption. This is achieved with carrier injection using a p-n or p-i-n junction, where an applied voltage causes electrons and holes to be swept into the junction from either side, where they can recombine.

In a p-n junction, a p and n-doped material are brought together in contact. A depletion region forms at the junction where electrons and holes recombine, ionising atoms on each side of the junction and creating an in-built electric field. A p-n junction is a diode, and permits the forward flow of current if a bias greater than the forward voltage is applied.

A p-i-n double heterostructure has a narrow bandgap intrinsic layer surrounded with wider bandgap p-doped and n-doped material on each side. Figure 2.2 shows the levels of the conduction and valence bands of the materials before and after they are brought together. The Fermi-level is close to the conduction band in the n-doped material and the valence band in the p-doped material. Band discontinuities at the interfaces arise due to misalignment of the energy bands. An advantage of the double heterostructure is that when forward biased, electrons and holes are confined to the narrower-bandgap intrinsic material due to the potential barrier, and so most of the recombination takes place in this region.

A separate confinement heterostructure (SCH) uses quantum wells or quantum dot layers to further localise the carriers. The lower dimensionality of these structures results in a modified density of states with discrete energy levels. Carriers are captured in the well, and this can be modelled using capture and escape time constants τ_c and τ_e [50].

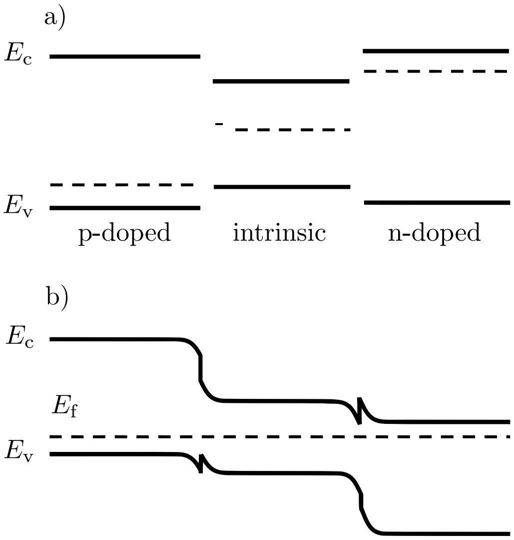

Figure 2.2: The band energies and the Fermi level for a) the p, i and n materials separately, and b) when they are brought together to form an unbiased p-i-n double heterojunction. The Fermi level E_f is indicated with a dashed line.

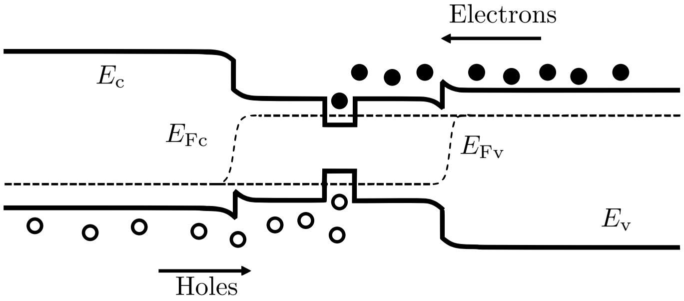

Figure 2.3: Injection of carriers with the SCH when it is forward biased, showing the bandgap of the material and the quasi-Fermi levels. Electrons, represented with solid circles, and holes represented with open circles, recombine in the quantum confinement region where the bandgap is narrowest. Adapted from [49].

2.1.3 Recombination and gain

In semiconductor, there are three radiative transitions: stimulated absorption, spontaneous emission, and stimulated emission. In a direct-bandgap semiconductor the minimum of the conduction band occurs at the same value of k as the maximum in the valence band. Electrons and holes can combine in a direct-bandgap semiconductor without any change in momentum, in contrast to an indirect-bandgap semiconductor which also requires a phonon to mediate the process, so direct-band semiconductors are much more suitable for light-emitting devices. The rate of spontaneous emission from valence-band electrons combining with holes in the conduction band is due to Fermi's golden rule, which describes the rate of transition between quantum states.

The k-selection rule is that transitions occur between states with the same wavevector due to momentum conservation, as the photon momentum is considered negligible. Many different transitions are possible between conduction and valence sub-bands. The k.p model is a perturbative method of calculating the band structure of a quantum well. The optical gain at a particular photon energy can be calculated by considering the strength of the interaction between the field with the states involved in the transition through a transition matrix element M_{T} and the density of transition pairs [51]. This describes a gain spectrum, which is the level of gain as a function of wavelength, for a particular injection level. The quantum wells in a VCSEL are designed so that the peak of the gain spectrum aligns with the cavity wavelength at the operating temperature and current. At high temperatures, the gain peak detunes from the cavity resonance wavelength, and so a higher current density is required to sustain the threshold gain. The gain detuning is due to the change in the bandgap E_{g}, which can be described by a Varshni model, given by

$$E_{\mathrm{g}} = E_{\mathrm{g},0} - \alpha_{\mathrm{g}} \frac{T^2}{\beta_{\mathrm{g}} + T} \tag{2.5}$$

where α_{g} and β_{g} are material constants.

2.2 Optical modes

The optical output of a laser is determined by the cavity modes that experience a gain above the threshold gain. The optical modes in an oxide-confined VCSEL are defined vertically by the Distributed Bragg Reflector (DBR), mirrors and laterally by the waveguiding effect of the oxide aperture. Figure 2.4 shows the

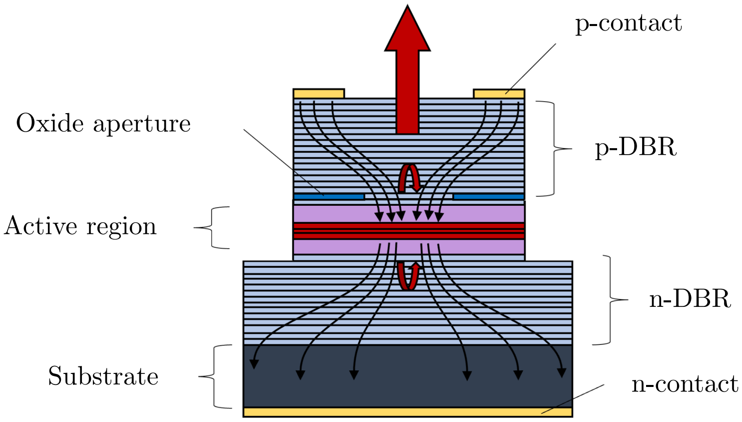

Figure 2.4: The structure of the VCSEL, showing the flow of the carriers through the active region and the propagation of the optical mode, indicated with the red arrows.

path taken by the carriers through the device and the location of the optical field in relation to the structure of the device. Light is outcoupled from the top mirror, which is slightly less reflective than the bottom because of the lower number of mirror pairs.

2.2.1 Optical properties

The refractive index of the $\mathrm{Al}_x\mathrm{Ga}_{1-x}\mathrm{As}$ alloy is a function of the composition, doping level, temperature, and excess carrier concentration. Different alloys in the AlGaAs material system provide the refractive index contrast that defines the optical cavity. The Adachi model [52] describes the refractive index below the band edge in terms of a simplified interband-transition model. Using parameters from [53], the properties of alloys in the AlGaAs material system can be described, with adjustments made for temperature and doping concentration. The Adachi model is given by

$$n(\lambda) = \sqrt{A_0 \left[f(\chi) + \frac{f(\chi_{S0})}{2} \left(\frac{E_0}{E_0 + \Delta_0} \right)^{\frac{3}{2}} \right] + B_0} \tag{2.6}$$

where χ and $\chi_{\mathrm{S}0}$ are functions of λ, and A_0 and B_0 are functions of the aluminium fraction x. The mirrors in a typical GaAs VCSEL use an alloy that alternates between 12% and 90% Al, with graded alloy interfaces to improve the carrier transport in the mirrors by removing sharp changes in the bandgap.

Wet oxidation with H_2O of an oxidation layer consisting of $Al_{0.98}Ga_{0.02}As$ results in the formation of a layer of Al_2O_3 oxide with an aperture in the middle that defines the active region of the device. This oxide material has a refractive index of ≈ 1.6, compared to the refractive index of the unoxidised material of ≈ 3.0.

At photon energies below the bandgap energy the absorption coefficient of a semiconductor is nominal, and all parts of the VCSEL except for the quantum wells are made from an alloy with a bandgap energy greater than the the energy corresponding to the lasing wavelength. The optical properties of the material change when the device is lasing. The temperature-induced refractive index shift is due to the thermo-optic effect, and the Drude model describes the refractive index shift with carrier density. As well as the refractive index shift with temperature, there is a thermal expansion coefficient of $5.73 \times 10^{-6}\,{}^{\circ}\mathrm{C}^{-1}$ for GaAs, but typically this effect has an order of magnitude smaller effect on the optical path length than the change in the material refractive index [54]. The wavelength shift of AlGaAs VCSELs with temperature is measured to be around $\approx 0.068\,\mathrm{nm\,K^{-1}}$, and this can be used as a measure of the cavity temperature [54].

2.2.2 VCSEL modes

Optical modes are self-consistent solutions to Maxwell's equations that satisfy particular conditions in free-space, in a waveguide or in a resonator. In a resonator, an optical mode satisfies a round-trip condition so that it is reflected back (possibly amplified or attenuated) but with the same spatial profile and phase. The quality factor Q describes how much of the energy remains after a round-trip in the resonator. An arbitrary optical field can be expressed in terms of the optical modes of a structure, and this is used as a method for calculating the propagation of fields.

2.2.3 Vertical mode profile

When light passes through an interface from a low to high refractive index material it undergoes a phase shift of π, but there is no phase change when going from a higher to a lower index material. In a in a DBR mirror alternating layers of higher and lower n material each with an optical path length of $\lambda/4$ the

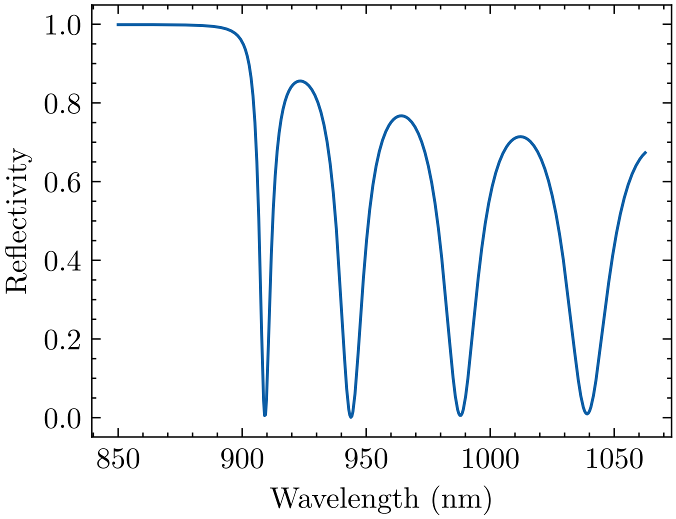

Figure 2.5: The stopband of the DBR top mirror in a structure with 20 mirror pairs, calculated using the TMM for an incoming plane wave. The reflectivity at the stopband wavelength is over 99.9%.

reflections at each interface destructively interfere at wavelengths of light at and around the stopband wavelength λ. The Transfer Matrix Method (TMM) is a method for calculating the propagation of light through a multilayered optical structure. Figure 2.5 shows the stopband of a VCSEL DBR at wavelengths at and above the stopband wavelength.

The vertical mode profile of a VCSEL can be determined using the TMM, or from a 3D calculation that also accounts for the scattering from the oxide aperture. Figure 2.6 shows the vertical profile of the mode plotted against the Al-fraction of the alloy, showing the quantum wells and the mirrors. The oxide aperture, with the highest Al-fraction, is at a node of the mode profile to minimise scattering and provide weaker confinement. The quantum wells are positioned at the peak of the mode to maximise the confinement factor Γ, which is the overlap between the mode intensity profile and the active region.

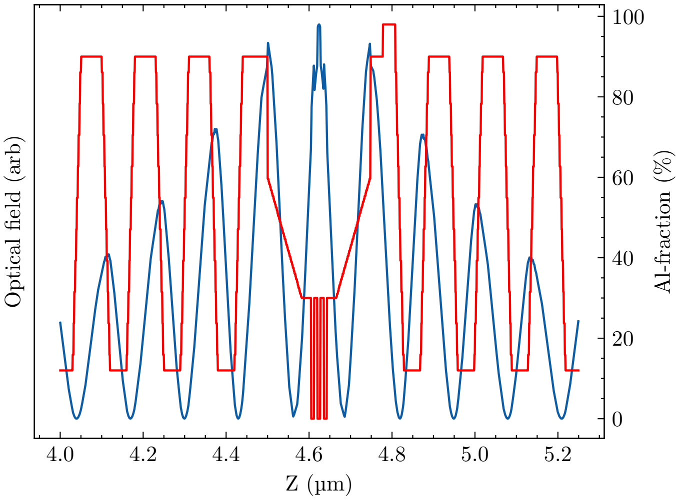

Figure 2.6: The vertical mode profile of a VCSEL (shown in blue), against the Al-frac in red showing the GaAs quantum wells where the Al-frac is 0%, and the oxide aperture where it is 98%.

2.2.4 Lateral modes in 2 dimensions

In an oxide-confined VCSEL the oxide aperture guides the flow of current, and provides the refractive index contrast that defines the transverse profile of the optical mode. Guiding carriers into the region of the optical mode means that oxide-confined VCSELs have low threshold currents and high quantum efficiencies. Using an effective-index approximation the refractive index profile of the VCSEL can be collapsed into one dimension, with the radial refractive index of a model given by the refractive index weighted by the vertical mode profile [55]. This approximates the VCSEL as a step-index fibre, the modes of which are the Gauss-Laguerre functions. The normalised frequency or V-number of a weakly guided optical fibre is given by

$$V = \frac{2\pi a}{\lambda_0}\sqrt{n_{\mathrm{co}}^2 - n_{\mathrm{cl}}^2} \tag{2.7}$$

for a core radius a and free-space wavelength of λ_0, where n_{co} and n_{cl} are the core and cladding indices respectively and r_{co} is the aperture radius. For a VCSEL with an oxide aperture at a null of the optical mode, using a weighted-index approximation the value of the core-cladding refractive index contrast $\Delta n \approx 2 \times 10^{-2}$. The single-mode condition of an optical fibre predicts a single confined mode if $V < 2.405$, and the number of guided modes is approximately $V^2/2$. For the $\Delta n = 0.02$ of a VCSEL, this predicts a single optical mode if the aperture diameter is $< 2.9\,\mu\text{m}$, which matches experimental observations.

In a circularly symmetrical VCSEL with weak optical guiding, the mode profile is approximated by the Gauss-Laguerre mode family. The fundamental mode has an intensity that is Gaussian, with a profile given by

$$S_{01}(r) \propto \exp\left\{-\frac{2r^2}{w_0^2}\right\} \tag{2.8}$$

where w_0 is the mode field radius or spot radius given by

$$w_0 = \sqrt{\frac{a\lambda}{\pi\sqrt{\bar{n}_{\text{co}}^2 - \bar{n}_{\text{cl}}^2}}} \tag{2.9}$$

.

2.2.5 Finding the optical modes in 3 dimensions

Finding the optical modes of a VCSEL is necessary to simulate the interaction between the carriers and the optical field. The cold-cavity modes are those calculated when there are no temperature or carrier-induced refractive index changes. Optical gain, carrier and temperature effects change the refractive index of the material in a lasing device, causing a change in the mode that can be described by a perturbation.

As the aperture size is reduced to a size comparable with the wavelength of the light, the use of a plane-wave approximation to find the mode profile breaks down. The spatial profile of the modes become three-dimensional, which changes the reflectivity of the DBR mirrors, and the overlap of the optical field with the active region [56]. The relative importance of the diffraction loss increases, and this eventually becomes the the dominant optical loss mechanism [57][58]. The wavelength of the modes blueshifts and the wavelength spacing between modes increases [59][60]. When designing VCSELs for atomic sensors, this blueshift must be accounted for in the epitaxial VCSEL design to achieve the target output wavelength.

A more comprehensive 3D model for the optical modes allows mixed TE and TM components. This better models the mode in the case of very small apertures. A number of different methods can be used to find the optical modes in three dimensions [55].

2.2.6 Thermal lensing and carrier-induced refractive index

The elevated temperature in the active region when the device is operating raises the refractive index profile from the cold-cavity case due to an increase in the bandgap energy, leading to thermal lensing where the optical confinement strength is increased. Increases in carrier density when the device is operating decrease the refractive index through free-carrier plasma and band-filling effects [61]. The refractive index contrast Δn, which defines the properties of the fibre and the guided modes, can be expressed in terms of the refractive index change due to heating and carrier-induced effects, as well as the cold-cavity oxide profile [62]. The Δn of the waveguide is given by

$$\Delta n = \Delta n_{\mathrm{ox}} + \frac{\partial n}{\partial N}\Delta N + \frac{\partial n}{\partial T}\Delta T \tag{2.10}$$

The thermal dependencies of the indices of refraction of GaAs and AlAs for wavelengths near 1 µm have been determined to be 2.7×10^{-4} to $1.4 \times 10^{-4}\,^{\circ}\mathrm{C}^{-1}$ respectively [63]. The gain and free carrier absorption have an effect on the real and imaginary parts of the refractive index. In VCSELs, carrier effects have a smaller effect on the refractive index than thermal effects.

The effect of thermal lensing is to reduce the effective diameter of the mode, and increase the far-field divergence angle. Measurements in [62] show that for both single and multi-mode apertures (of diameters 3 and 5 µm respectively), the effective diameter of the mode decreases by less than 0.2 µm for injection currents between 0 and 6 mA.

2.2.7 Polarisation

Circular oxide aperture VCSELs have transverse modes that are (almost) linearly polarised. Circularly polarised light is required for atomic clocks and magnetometers, and a quarter-wave plate is used to convert linearly polarised light. Slight anisotropies due to the crystal lattice and shape of the oxide aperture mean that the polarisation tends to preferentially align to the [110] and the $[0\bar{1}1]$ crystal axes [64].

However, switching between orthogonally polarised states can occur during operation, because there is no strong preference to fix the polarisation along a particular direction. Surface gratings of various designs [65], non-circular surface reliefs [38], and elliptical or otherwise non-circular apertures [66] are used to fix the polarisation direction.

2.3 Loss mechanisms

The quantum efficiency and maximum power optical output of a diode laser is limited by mechanisms by which carrier pairs combine non-radiatively, and by optical absorption. These losses increase with temperature, which causes the efficiency to drop at high internal temperatures and eventually leads to the thermal rollover and turnoff. When performing a device simulation, parameters describing these mechanisms are contained in material files derived from results in the literature.

The internal quantum efficiency η_{int} is the fraction of carrier pairs injected into the device that combine to emit a photon, and the external efficiency η_{ext} is the fraction of the injected carrier pairs that result in the emission of a photon that is eventually outcoupled from the device. The corresponding differential efficiencies are the slope of the efficiency at injection currents above the threshold current.

Non-radiative recombination is when an electron and a hole recombine in a process that does not result in the emission of a photon, and these mechanisms determine the internal efficiency of the device. The two main non-radiative recombination mechanisms are Shockley-Read-Hall (SRH) and Auger recombination. These mechanisms have different power law dependencies on the carrier density N, due to the number of carriers required for each transition to occur, and this can be used to identify their respective contributions by examining the behaviour of the device at low and high injection currents [51].

The leakage current J_{rest} accounts for carriers that are not captured by the wells but pass through the active region, and then recombine at the metal contacts [67]. A commonly used approximation used to describe the recombination currents as a function of carrier density N is the ABC model

$$\begin{aligned} J_{\text{total}} &= J_{\text{stim}} + J_{\text{rest}} + J_{\text{SRH}} + J_{\text{spont}} + J_{\text{Auger}} \\ &= J_{\text{stim}} + J_{\text{rest}} + AN + BN^2 + CN^3 \end{aligned} \tag{2.11}$$

Internal loss by free carrier absorption and scattering determine the external efficiency, which is lower than the internal efficiency. The non-radiative recombination and loss mechanisms are described in the following sections.

2.3.1 Shockley-Read-Hall recombination

SRH is a recombination mechanism mediated by an intermediate energy state between the conduction and valence bands. The SRH recombination coefficient A is due to the density of trap states in the material. Trap states are due to defects in the crystal lattice that lead to intermediate energy states between the conduction and valence bands. As given in [51], the recombination rate R_{nr} of excess carriers with concentration Δn can be calculated in terms of the capture rate and cross section per deep state, or more simply described by a time constant τ_{nr}

$$\frac{1}{\tau_{\mathrm{nr}}} = \frac{R_{\mathrm{nr}}}{\Delta n} \tag{2.12}$$

2.3.2 Auger recombination

Auger recombination is a 3-particle process where non-radiative carrier recombination takes place through an intermediate energy state. Most of the Auger recombination happens in the quantum wells due to the much higher carrier density. A model used for the coefficient C is presented in [68], using data from measurements of GaAs quantum wells at 870 nm, and is given by

$$C_{\mathrm{n,\ p}}(xT) = C_{\mathrm{n,\ p}}(x) \exp\left[\frac{aE_{\mathrm{g}}(x,y)}{k}\left(\frac{1}{T_0} - \frac{1}{T}\right)\right]. \tag{2.13}$$

Strain in quantum wells has been observed to reduce the Auger effect, and this effect can be employed in the design of quantum well lasers[69][70].

2.3.3 Leakage current

Leakage current in a quantum confined diode laser is due to carriers that pass through the active region, rather than recombining in the quantum wells. Thermal activation allows carriers to pass over the potential barrier in the SCH. Leakage occurs by both drift and diffusion over the heterobarrier, and increases superlinearly with carrier density and temperature [51]. Carriers that leak over the barrier can then recombine in the region where they are the minority carrier, or are swept to the metal contact [67].

2.3.4 Free carrier absorption

Free carrier absorption (FCA) occurs when a photon is absorbed causing a carrier to be excited from an already-excited state to another, unoccupied state in the same band. In the simplest approximation, the Drude model, free carrier absorption increases quadratically with wavelength [71]. Intervalence band absorption (IVBA) is a type of optical absorption that occurs within the valence band of a semiconductor material, specifically in the region between the heavy and light hole subbands. These effects introduce an absorption α_{FCA} that increases the optical loss of the mode, which increases the threshold gain requirement and reducing the quantum efficiency. Figure 2.7 shows the processes that are termed free carrier absorption.

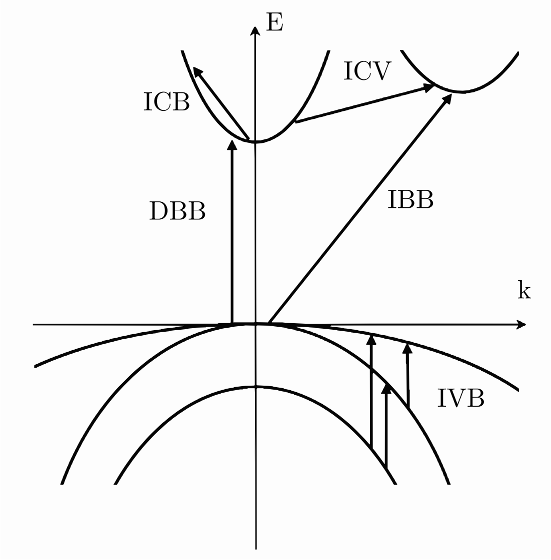

Figure 2.7: View of different FCA mechanisms, showing direct band-to-band absorption (DBB), indirect band-to band absorption (IBB), intervalence band absorption (IVB, or IVBA), intraconduction band absorption (ICV), interconduction valley absorption (ICB).

A number of different theoretical models give values for the FCA coefficients. A relationship in [72], using values from [73], gives the value of α_{fca} in terms of the hole concentration, p_{T}, and electron concentration, n_{T}

$$\alpha_{\mathrm{fca}} = k_{\mathrm{n}} n_{\mathrm{T}} + k_{\mathrm{p}} p_{\mathrm{T}} \tag{2.14}$$

where k_n and k_p are the free carrier absorption coefficients for electrons and holes. Intervalence band absorption (IVBA) can be described by an equation from [72]

$$\alpha_\mathrm{IVBA}(E_\mathrm{phot}) = \alpha_\mathrm{0p} \exp(-b_\mathrm{p} E_\mathrm{phot}) p \tag{2.15}$$

where α_{0p} and b_p are the IVBA coefficients and p is the hole density. [72] suggests that depending on the experimental results, the FCA effect in the quantum wells are between 1 and 10 times the bulk value. In [47] a thermally activated adjustment to Equation 2.14 is used to perform high-temperature simulations. There are also some theoretical or semi-empirical models for free carrier absorption, such as that given in [74].

2.3.5 Scattering loss

As well as diffraction losses from the oxide aperture, there is scattering α from material roughness and defects, and has been shown to affect the threshold current [75]. This has been shown due to diffusion of Si dopant atoms in the n-DBR [76], which is also shown to be a degradation mechanism. The scattering loss is of the order of $10\,\mathrm{cm}^{-1}$ [77].

2.4 Enhanced optical output power

Higher output power from VCSELs is an active area of research and there are a number of approaches to achieve this.

2.4.1 Arrays and lateral coupling

VCSEL arrays are a way of scaling the output power. The small size of individual emitters means that high power densities can be achieved, and the vertical emission of light makes VCSEL arrays suitable for a number of applications such as LiDAR illumination and materials processing.

The high power density of arrays means that significant effort is required to manage the thermal effects, which are the limiting factor for array performance [78]. Lateral coupling of multiple emitters is an approach that could give enhanced single-wavelength output power compared to single-emitter designs. A number of different methods have been proposed for achieving coupling, using the evanescent part of the mode with emitters spaced close together, or using guiding elements to guide the light [37].

Evanescent coupling requires the emitters to be within the range of the exponential decay of the mode field. In [79] evanescent coupling is used to reduce the output linewidth to 30% of that of a single emitter. Other approaches include external optical cavities [80][81], VCSELs connected with optical elements connecting them [82], and coupled cavities defined with photonic crystals [83]. Coupled VCSELs have also been proposed as a way to achieve higher modulation frequencies, due to the resonantly enhanced modulation response [84].

2.4.2 Higher order mode control

Single-mode lasing for larger-diameter apertures can be achieved by suppressing the lasing of higher-order modes, by selectively introducing loss to modes except for the fundamental one. A surface relief can introduce a mode-dependent loss. Material is selectively etched from the top mirror to vary the reflectivity, increasing the loss of higher-order modes to prevent them from lasing.

In an anti-phase surface relief design the top mirror is grown in such a way that reflections from the top mirror are initially out of phase, and then an etch is carried out in the centre of the mesa to make the reflections in-phase. This approach is more tolerant to fabrication variations as the growth thickness can be defined more accurately than the etch depth, and because the range of cap thicknesses where the reflectivity is reduced is considerably narrower than the range of thicknesses where the reflectivity is high. With this approach, using a 3 µm diameter surface relief and a 5 µm oxide aperture diameter, a maximum power of 6.5 mW with more than 30 dB of higher order mode suppression has been reported for an 850 nm VCSEL [85]. An anti-phase coating can also be selectively deposited on top of the device to achieve a similar effect, and this has been used to achieve over 7 mW of optical power [86].

Disorder-defined apertures use zinc diffused into the top mirror to define a region with lower optical reflectivity and higher free carrier absorption. This selectively suppresses the lasing of higher order modes compared to the fundamental mode, allowing larger oxide aperture sizes and measured single-mode optical output powers of 10 mW [39]. An anti-waveguide cavity design has been used to achieve 5.3 mW of optical power [87].

2.4.3 Stacked junctions

Extension of the device in the vertical dimension can be achieved by using a stacked junction VCSEL. This consists of two coupled cavities each containing active regions, and separated by a tunnel junction and a Bragg mirror stack. At present this type of device has been commercialised at wavelengths at 980 nm for LIDAR applications [43], and studied at wavelengths including 850 nm [44]. Such devices also achieve excellent power output efficiency, with values being reported as high as 60%, compared to less than 50% for conventional VCSEL designs. In the GaAs material system, a tunnel junction can be realised using highly doped GaAs layers, using dopant elements such as tellurium and magnesium for improved solubility [88][89].

2.4.4 Photonic crystal VCSELs

Photonic crystal-like structures are a different way of defining the refractive index profile that defines the optical mode. In a photonic crystal, a structure with periodic variation in the refractive index leads to a stop-band of wavelengths of light that cannot propagate in the crystal by analogy with a semiconductor crystal [40], and a "defect" or missing hole can act as a resonant cavity [90]. Holes etched into the top mirror of a VCSEL structure result in a modification to the refractive index profile, and this effect can be used to engineer a optical resonator that preferentially supports a single optical mode. Photonic crystal VCSELs can have higher single-mode optical power output than oxide-confined VCSELs because the confinement due to a photonic crystal is weaker than that of an oxide layer and so larger apertures can be single-mode. The typical minimum feature size of these devices is on the order of 1.5 µm and so photonic crystals can be fabricated with conventional i-line contact lithography processes [91]. A section view of a photonic crystal VCSEL is shown in Figure 2.8.

The photonic crystal can be simulated using a 2D approximation, with the gain, influence of the photonic crystal etch, and the increased scattering represented by real and imaginary refractive index values. These values can be found by fitting the measured properties of the modes to those in a simulated 2D waveguide structure.

The out-of-plane behaviour of the photonic crystal can be described using the plane-wave expansion as presented in [93]. A 2D hexagonal photonic crystal is described by two values a and b, which are the pitch between the centres of the holes and the hole diameter respectively.

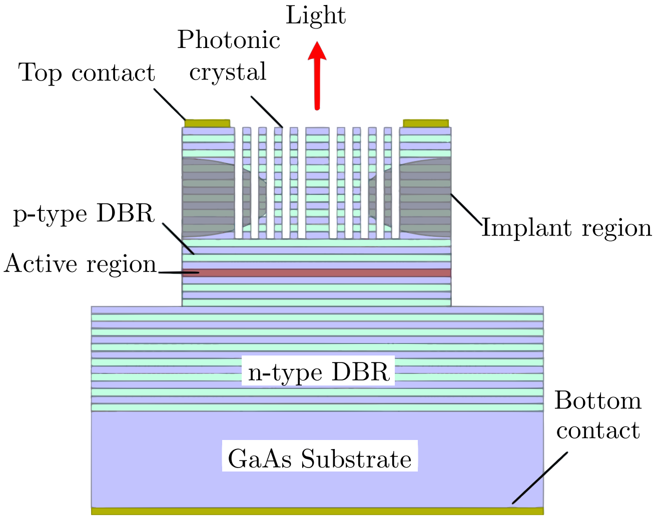

Figure 2.8: A sectional view (not to scale) of a photonic crystal ion-implanted VCSEL, showing the stacked implantation of the photonic crystal holes, adapted from [92]. There is no oxide aperture in the devices investigated here, but an aperture in the ion implantation region defines a path for the carriers.

Chapter 3

Experimental methods

In this chapter, the methodology for designing, fabricating, and measuring the characteristics of VCSELs is discussed. VCSEL epimaterial was designed at Cardiff University and grown at IQE and CSC. The device designs were created in a mask layout tool and transferred to a photomask for fabrication with a mask aligner. The devices were fabricated in the Institute for Compound Semiconductors (ICS) cleanroom at Cardiff University, and measurements of their performance and characteristics were performed in the labs of the Optoelectronics group. Figure 3.1 shows the outline of the fabrication process, which is discussed in the following sections.

A standard VCSEL process flow was used to fabricate the devices, but some additional methods were used to develop the novel aspects of the devices studied in this thesis. A simple method of simulating the oxide extent predicted by the Deal-Grove model was used to design a mesa shape to pattern closely-spaced multiple emitters. Different ion implantation regimes to provide lateral current isolation were investigated as a means for controlling the injection of current into different closely spaced emitters, to independently control their wavelengths. The temperature increase in a VCSEL when a pulse of current is applied is examined to determine the size of this increase as a function of pulse length and duty cycle. Pulsed measurements are used as an approximation to isothermal operation, and so in this way it is possible to determine how much heating is occurring with different regimes.

3.1 Mask design and layout

The designs were created in K-Layout, a freely available layout tool with a scripting interface. The limitations of the optical lithography process due to alignment tolerances and resist resolution mean that the smallest feature size used is around 2 µm. The mask layout was arranged for compatibility with on-tile probing, mounting on headers in groups, or singulation for packaging. Individual devices are arranged into groups of 100 devices with a pitch of 250 µm, with 16 such groups on a tile, as shown in Figure 3.2. Using e-beam lithography, the pattern was transferred to a chrome-plated quartz hard mask by Photronics for use in a mask aligner.

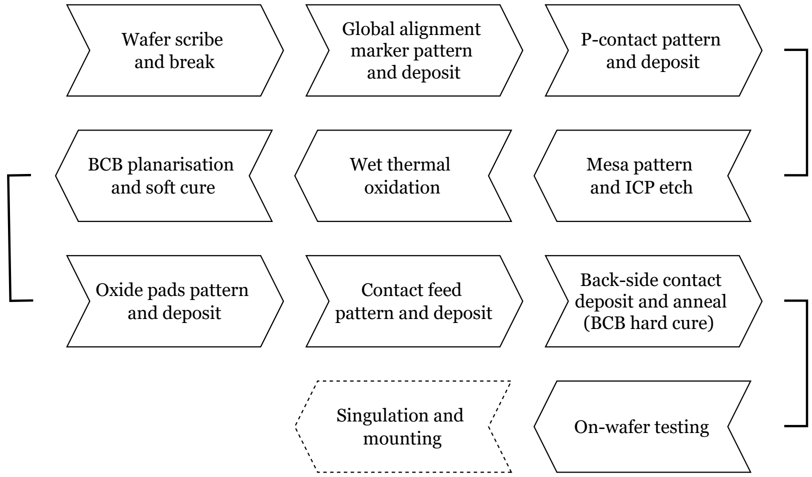

Figure 3.1: Simplified VCSEL process flow showing the order of steps.

Fiducial alignment markers are first patterned so that each subsequent fabrication process can be aligned with the same reference for the best possible overlay. Oxidation test structures are used to monitor the progression of the aperture oxidation with an infrared camera as discussed in Section 3.7, and etch depth test structures allow for the measurement of the depth of an etched feature with a profilometer as discussed in Section 3.5.

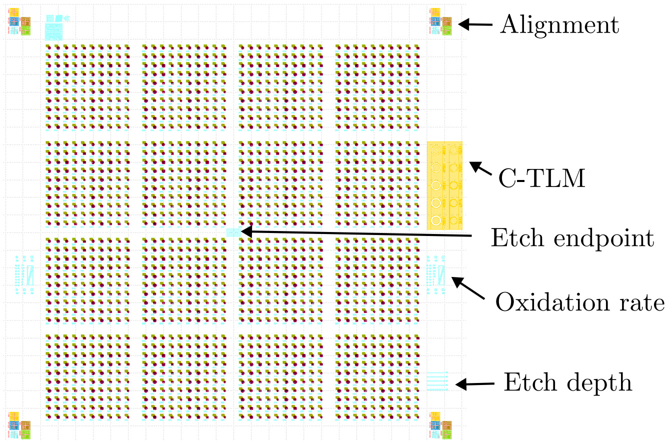

Figure 3.2: A view of the mask, showing the layout of the devices, and the other structures that are present. For the conventional process there are 6 optical alignment processes, plus an ion implantation or isolation etch step. There are 1600 VCSELs on this tile, but less than 1% of the area is occupied by devices (most of what can be seen is the contact pad.) The tile is 12.5 mm along each side.

3.2 Epitaxial growth

The epitaxial material is grown in a metallo-organic chemical vapour deposition (MOCVD) process in collaboration with the Compound Semiconductor Centre (CSC). Precursor gases are pumped into a chamber containing a heated substrate, and when the precursor gases make contact with the substrate they thermally decompose or “crack” after which the constituent atoms can adsorb onto the substrate and become part of the crystal lattice. Variation of the concentration of precursor gases changes the composition of the bulk material and the concentration of dopant species. The introduction of gases in the reaction chamber via a showerhead results in a very even distribution of process gases in the chamber, and the wafers are rotated on two axes. The layer thicknesses are monitored in-situ using a reflectometry measurement to target the desired cavity thickness.

3.2.1 Material and fabrication variations

Typical VCSEL applications do not have particularly stringent wavelength requirements compared to the typical variation across the wafer due to the growth process, whereas for atomic sensor applications the emission wavelength is very precisely defined. For this application, the epitaxy is specified to be within ± 2 nm of the target wavelength, while for data-communications ± 20 nm is acceptable. The optical output wavelength of a VCSEL is defined by the optical path length of the cavity and the dimensions of the oxide aperture, and so the output wavelength is due to both the epitaxy and the fabrication.

The material used for fabrication has to be selected from particular parts of the wafer. Prior to device fabrication, the properties of the wafer were mapped with a Nanometrics RPM PL Wafer Mapping System. The width of the mirror stopband and the wavelength of the dip in the stopband corresponding to the cavity resonance were measured with a spatial resolution of 2 mm. A grating with 300 lines/mm and a slit width of 0.025 mm splits the light onto a 1024-element CCD array, giving a precision in the wavelength measurement of 0.13 nm.

These measurements were taken at a substrate temperature of 26.6 °C, corresponding to the ambient temperature inside the measurement chamber. The intended internal operating temperature of the emitters is around 50-80 °C, and so the projected deviation of the cavity wavelength from the target wavelength of 852.2 nm (corresponding to the D2 line of caesium) can be calculated using the standard wavelength shift of $0.068\,\mathrm{nm\,K^{-1}}$ for this type of VCSEL.

The 3D cavity mode is at a slightly lower wavelength than this dip (on the order of 1 nm, but the effects of self-heating of the cavity region in operation increase the output wavelength by up to 0.5 nm, so these effects approximately cancel. A nominal target wavelength of 850.6 nm was therefore used to identify suitable material, with tuning to the target wavelength achieved by controlling the substrate temperature. Figure 3.3 shows the deviation of the measured wavelength of the dip in the reflectivity spectrum from this nominal target wavelength, showing that there are a number of areas of the wafer where on-specification material can be found, as well as large parts where the wavelength is > 10 nm out of specification.

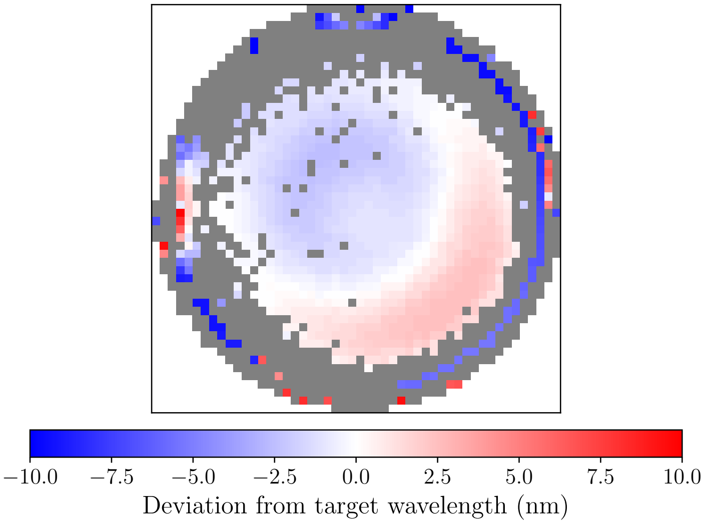

Figure 3.3: The variation across the wafer of the dip in the reflectivity spectrum, corresponding to the cavity wavelength of a plane-wave mode in one dimension. Regions shown in grey are outside the range of wavelengths of ±10 nm from the target cavity wavelength.

3.3 Sample and surface preparation

After identification of the desired material, the wafer is cleaved by scribing and then applying pressure so that the crystal separates along a crystal axis. The samples are cleaned to remove dust and organic residue using a combination of heated solvents (acetone, methanol and isopropyl alcohol) and ultrasonic cleaning. This series of solvents removes a broad spectrum of potential contaminants and is the standard cleaning procedure between fabrication steps.

An oxygen plasma asher is used to remove any other residue from the samples. Oxygen radicals in the plasma chemically react to produce an ash that is removed by the vacuum pump, and also make the sample surface hydrophilic, which promotes photoresist adhesion.

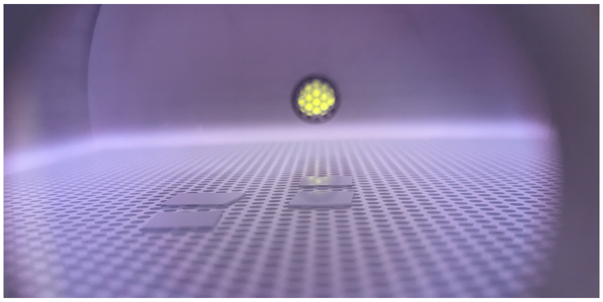

Figure 3.4: Samples in the oxygen asher, seen in the foreground sitting on a metal mesh. The oxygen plasma has a faint purple glow. At the back of the chamber can be seen the port where the oxygen radicals are injected into the chamber.

3.4 Lithographic pattern transfer

Contact lithography was used to transfer the pattern from the hard mask to the photoresist. Ultraviolet light projected through a hard mask in contact with the sample interacts with photoresist on the sample, which is then selectively removed by a chemical developer to expose parts of the semiconductor surface for etching or deposition. Accurate pattern transfer from the hard mask to the photoresist requires the correct combination of resist thickness, exposure dose, and development parameters.

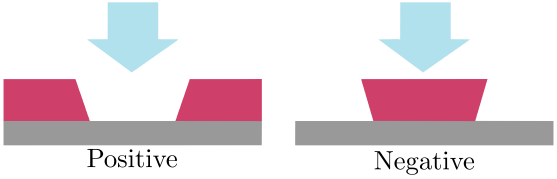

Figure 3.5: The resulting resist profile from positive and negative tone resists, with the exposed area on each resist is indicated with the blue arrow. The undercut in a negative-tone resist ensures a break in material deposited, so that there is a clean lift-off when the resist is stripped.

3.4.1 Resists and spin coating

Photoresists can have a positive or negative tone, which refers to the change in the solubility of the developer after they are exposed in the photolithography process. Negative tone resists become less soluble after exposure due to increased cross-linking of the polymer molecules, and can be used to produce resist profiles with undercut, which is useful for lift-off of deposited materials as the undercut introduces a break into the deposited film. Positive tone resists become more soluble after exposure and are suited for applications such as etch masking due to the stability of the resist profile. The typical resist profiles of positive and negative tone resists are shown schematically in Figure 3.5. The resist profile achieved is due to the exposure dose, post-exposure bake, and development time.

Spin coating is a method of applying a thin uniform coating to a flat surface using centrifugal force. The photoresist is applied as a liquid and then spun at a specific speed so that it is thinned and the solvents dry off to leave a film. For application of photoresist, the sample is first plasma ashed, and then dehydrated by baking at a temperature of 110 °C to remove water adsorbed onto the surface. An adhesion promoter (TI Prime) is spun on and a submonolayer is adsorbed onto the surface after activation with a short bake.

Photoresist is applied with a pipette, and care has to be taken not to introduce bubbles which will lead to non-uniformities in the coating thickness. The thickness of the resist film depends on the spin speed, as well as the sample size and type of spinner, which influence the air currents that dry the solvent. The manufacturer's data sheets give the relationship between the spin speed and the thickness [94]. A spin time of 45 s is sufficient for the solvents to dry, and spin speeds between 2000 and 6000 rpm are used for the different resists and thicknesses required. After the resist is spun on, a short bake of 2 min is used to remove more solvents and make the resist more mechanically stable for the lithography process.

3.4.2 Lithography

The pattern is transferred to the sample using a Carl Zuss MJB-4 mask aligner. A hard mask is brought into physical contact with the sample and then collimated UV light is projected through it onto the sample. The mask aligner provides a means to manipulate the x, y and θ of the sample, as well as the degree of force with which the sample is brought into contact with the mask.

Other lithography methods are also used in research and industrial applications. Electron beam (e-beam) lithography uses a focused beam of electrons scanned across the sample in a raster pattern, and because the shorter wavelength of electrons allows patterning of features smaller than can be achieved with UV light, e-beam lithography is used for sub-wavelength structures on VCSELs such as polarisation-control gratings. Projection lithography uses an image of the mask that is projected onto the sample, from a reticle (in the case of a stepper as used in high-volume production), or from a digitally controlled mirror as used in a maskless projection system.

The MJB-4 mask aligner has a mercury ultraviolet lamp that is normally set to provide 400 W of optical power. An i-line filter can be used to select only the 365 nm emission line of mercury, as better resolution can be achieved with monochromatic light. The intensity of the illumination is calibrated using a UV power meter. The required dose is obtained by setting the exposure time which is controlled by the shutter on the mask aligner, a typical exposure taking between 5 s and 1 min.

Alignment is achieved using the microscopes and translation stage, and the contact pressure is set by adjusting the height of the vacuum chuck that holds the sample. The presence of an edge bead in the resist on the sample can mean that the middle of the sample is not in contact, resulting in “nibbling” artefacts where there is optical interference between the sample and the mask. The sample can move as it is brought into contact with the mask, and so the alignment has to be done incrementally.

3.4.3 Resist development

After exposure, the resist is developed in a weak alkaline solution such as AZ726K (for negative tone resists) or AZ400K (positive tone resists). Agitation in the developer ensures a constant development rate. After the development, the dimensions of the transferred pattern and the quality of the alignment can be measured using an optical microscope with a length scale and artefacts examined, as shown in Figure 3.6.

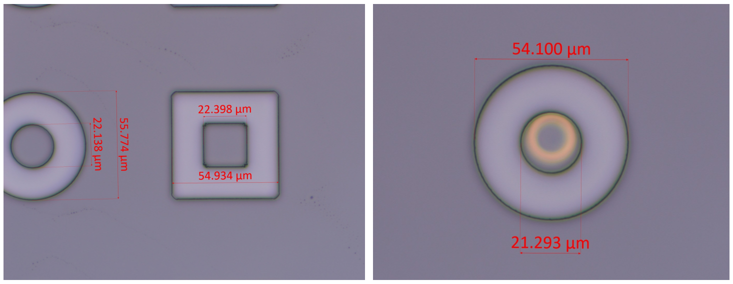

Figure 3.6: A developed sample, showing measurements of the dimensions of the photoresist etch mask prior to the etching process. These are within 1 µm of the nominal dimensions. The measurements can be compared to measurements of the etched sample. 'Nibbling' can be seen in the corners of the square feature due to improper contact between the sample and the mask. On the right, less than ideal overlay of the mesa etch exposure with the p-contact layer. If the overlay is not sufficiently good the resist can be removed and the lithography process restarted.

3.5 Dry Etching

Etching of the mesa structure is performed using an inductively coupled plasma reactive ion etching (RIE-ICP) tool from Oxford Instruments. Etch gases are injected in a specific ratio and ionised by inductive coupling from a varying magnetic field, which energises the electrons in the gas. An RF source varies the potential of the sample and accelerates ions towards the sample. Etching is caused by both the physical bombardment by accelerated ions and chemical reactions due to the radicals in the chamber [95]. RIE-ICP tools have better control of the plasma characteristics as the RIE and ICP power are controlled separately, and so can achieve higher plasma densities and lower chamber pressures. A schematic of an RIE-ICP tool is shown in Figure 3.7. Figure 3.8 shows how a vertical mesa profile can be achieved and the extent of the footing in the etch.

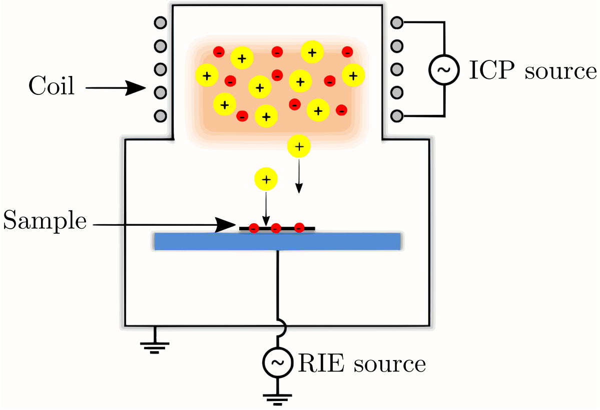

Figure 3.7: A RIE-ICP tool, adapted from [96]. The plasma is generated by the ICP source and accelerated by the RIE source.

To achieve the straight sidewalls desired in the mesa, a balance of chemical and physical etching is required. The etch used for the mesa uses the process gases Cl_2, BCl_3, N_2 and Ar, with 200 W of RIE and 500 W of ICP power, and this achieves an etch rate of around 1 µm/min. The AZ10-XT resist mask used for the etch is removed at a rate similar to that of the semiconductor, so a thick resist mask is necessary. The temperature of the sample is controlled by a flow of backside helium against a carrier wafer, and the sample is held in physical and thermal contact with the carrier with a small spot of Fomblin oil. The chamber has to be cleaned and conditioned before each run to remove any potential contaminants from the chamber walls and establish a known concentration of reactants in the chamber. After etching in the ICP, surface passivation is achieved by submersion in deionised water, and the resist is removed with NMP or TechniStrip MLO-07 resist stripper.

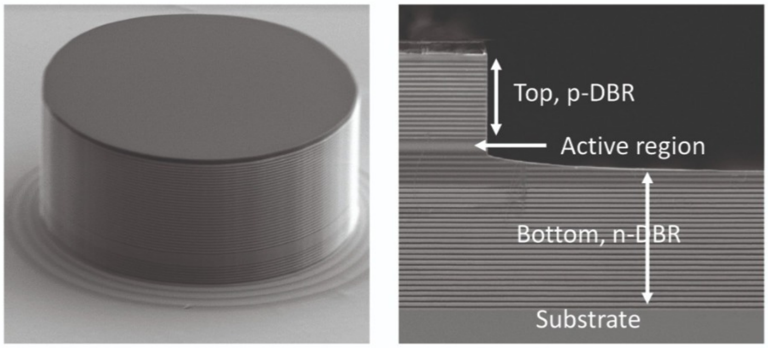

Figure 3.8: A VCSEL mesa etch performed in the ICS cleanroom using the Oxford Instruments RIE-ICP etch tool. On the left, the highly vertical profile of the etch is shown. On the right is shown a cross-section of the etch, with the sloped foot indicated. The foot of the etch is due to the profile of the resist and can be as high as several mirror pairs, so the etch is typically targeted to 4 mirror pairs below the active to ensure it is sufficiently deep. Figure from [97].

3.5.1 Endpoint monitoring of etching

The progress of the etch through the material can be monitored with an end-pointing laser to monitor the cycles of constructive and destructive interference from layers of differing dielectric constant. A laser with a wavelength of 670 nm, outside the stopband range of the DBR mirrors, is focused onto the sample and the reflected signal monitored with an infrared camera. This process can also be simulated approximately using the transfer matrix method, taking into account the high sub-bandgap absorption of GaAs, which is on the order of $1 \times 10^4\,\mathrm{cm}^{-1}$ [98]. A simulation assuming a constant etch rate with depth shows the characteristic profile of the cavity region, which is three smaller peaks for this type of VCSEL with a 1λ cavity. The mirror pairs are counted as they are removed to target the correct etch depth, as shown in Figure 3.9. The simulation can be a useful tool to interpret the end-point trace and stop the etch at the desired point in the structure.

3.5.2 Depth measurements with profileometer

A profilometer (DektakXT Advanced System) was used to measure the depth of the etch across the sample. This uses a stylus held with constant pressure above the sample, and as the sample is moved, the position of the stylus is monitored.

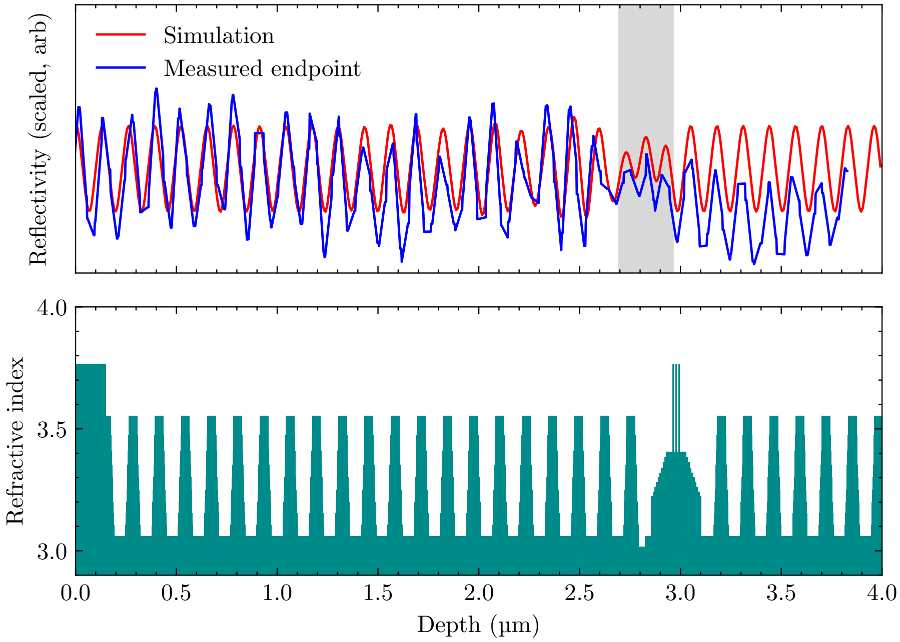

Figure 3.9: Comparison of the measured and simulated etch traces. The active region can be seen from the smaller peaks (shown in grey on the endpoint trace), which occur as the etch approaches the active region. The etch was targetted to stop on the 3rd peak after these smaller peaks, which corresponds to a depth of 2 mirror pairs below the active region.

The depth of a dry etch process can have an aspect ratio dependence. The endpoint monitoring square is much larger (500 µm square) than the width of the mesa etch, but they are assumed to be around the same depth, as the trench is much deeper than it is wide. In the case of the etched posts used for closely-spaced devices, the aspect ratio of the etch is around 1:1, at which point aspect-ratio dependence starts to become more significant. Narrow trenches were used to measure the etch depth of smaller features and estimate the dependence of the etch depth on the feature aspect ratio.

3.6 Material deposition

Metal layers are used for the nickel alignment markers, the p-contact, the feed, and the backside n-contact. A SiO_2 dielectric layer provides electrical isolation underneath the contact pad. Vacuum deposition is used to selectively apply these layers to the sample, with areas not intended for deposition masked off with a photoresist mask. Figure 3.10 shows a thermal evaporator, similar to one of the types used during this process.

Vapourisation of a material under vacuum conditions results in a long mean free path, and a sample placed at an appropriate distance from the material being evaporated receives a uniform and highly directional flux of incoming atoms. A uniform film is deposited over the sample, and when the resist mask is removed, material is selectively left on the sample.

A quartz crystal monitor tracks the rate of deposition by measuring the change in its resonant frequency with increasing mass. Some of the evaporators used for particular depositions have automatic control of the deposition rate, while others require manual control of the current to maintain the desired rate. Typically, a deposition rate of $0.1\,\mathrm{nm\,s^{-1}}$ gives uniform and consistent results. A very high vacuum is required (around 1×10^{-6} mbar or better) because of the tendency of oxygen to react with the metals at high temperatures and the very low vapour pressures of the evaporated materials. Turbomolecular pumps are used to achieve the required vacuum. Ti can also be used as a gettering agent to take oxygen up in the evaporation chamber prior to the deposition of the p-contact.

The deposition material is evaporated either thermally, using an electrical current to heat a crucible containing the deposition material, or with a focused e-beam that is magnetically deflected onto the target. Thermal evaporation is

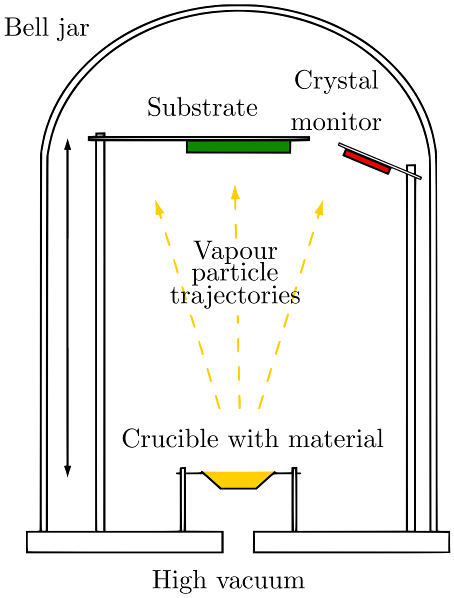

Figure 3.10: Schematic of a thermal evaporator, such as an Edwards thermal bell jar evaporator, adapted from [99].

possible for metals such as Ni and Au where the melting temperature is less than that of a steel or ceramic crucible. Ti and SiO_2 are evaporated using an e-beam steered magnetically onto a crucible containing the material for deposition.

Prior to contact deposition, the sample is deoxidised using a 5% ammonia solution to remove the native oxide and then immediately loaded into the evaporator and placed under vacuum. The p-contact is Ti-Pt-Au, with layer thicknesses of 10-20-60 nm respectively. The n-contact on the back-side of the sample is AuGe-Ni-Au, with thicknesses of 100-28-300 nm. The feed is a thick layer of gold, its thickness provides a surface for the probes to make contact and smooths any variation from the BCB planarisation. After deposition, the sample was placed in a resist stripper such as NMP 1165 or TechniStrip MLO-07 and agitation was used to complete the lift-off.

Ohmic contacts between the metal and the semiconductor are formed by a rapid thermal annealing (RTA) process that causes the metal and the semiconductor to interact at the interface [100]. The sample is annealed at a temperature of 385 °C for 3 minutes, with gradual ramping up and down of the temperature. The quality of the ohmic contact can be measured using circular transfer length method (CTLM) measurements.

3.7 Oxidation

Wet oxidation converts a layer of $Al_{0.98}Ga_{0.02}As$ into a ring of Al_2O_3 with an aperture in the middle using high-temperature water vapour in an inert N_2 atmosphere. The aperture controls the flow of carriers into the active region and optically confines the optical mode, and so it is critical to the performance of the device. The reaction rate is very strongly dependent on the reaction conditions, in particular the temperature and Al-fraction of the oxide layer, and so variations in the reaction conditions across the wafer are a major source of variation in device characteristics.

3.7.1 Chemical process

The oxidation layer in an $Al_xGa_{1\text{-}x}As$ VCSEL epistructure is an Al-rich layer, typically with an Al fraction of 98%. At high temperatures above 300 °C the main reaction taking place is

$$\mathrm{AlGaAs} + \mathrm{H_2O} \longrightarrow \mathrm{Al_2O_3} + \mathrm{AsH_3} + \mathrm{Ga}$$

but there are some other competing reactions [101]. The As products are volatile compounds and can be removed from the porous Al_2O_3 by nitrogen. There does not appear to be a mechanism for Ga to precipitate out of the structure during oxidation, and measurements suggest that it is present in the final oxide. The use of AlAs as an oxidation layer can lead to device lifetimes of only a few minutes, while $Al_{0.98}Ga_{0.02}As$ has much better longevity [102].

3.7.2 Deal-Grove diffusion model and rate dependence

The Deal-Grove model [103] describes the progression of the oxidation reaction in one dimension. The rate of oxidation is governed by the diffusion rate of the oxidising gas into the surface of the existing oxide, then diffusion of these species through the oxide, and then the reaction at the front with the unoxidised material. Figure 3.11 shows the mechanisms that determine the oxidation rate.

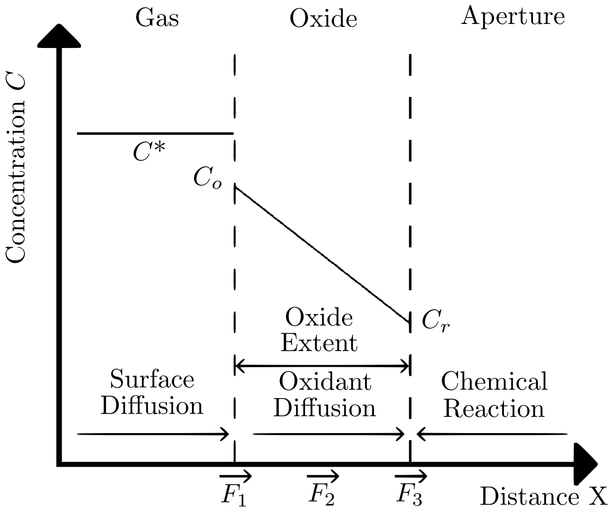

Figure 3.11: The three different processes that determine the oxidation rate. The fluxes F_1, F_2 and F_3 are equal, in the steady-state approximation in which the Deal-Grove model is applicable. The concentration C^* is the concentration in the reaction chamber, C_o is the saturation concentration of the reactants in the oxide, and C_r the concentration at the reaction. The diffusion is due to the concentration gradient between the surface and the reaction.

The model predicts different regimes where the progression rate depends on the diffusion process through the oxide, or on the chemical reaction process. The oxide extent initially grows linearly with time t when limited by the chemical reaction at the oxide front, and then with $\sqrt{t}$ when limited by the diffusion through the existing oxide. At a temperature of 420 °C as used in this process, the oxidation rate remains in the linear regime to an extent of 80 µm [104], which is much longer than the oxide lengths used in VCSELs. The rate depends exponentially on both the temperature and Al-fraction [102]. Figure 3.12 shows the dependence of the activation energy and oxidation rate on the composition. The sensitivity to these parameters means that achieving uniform oxide extents across a wafer is a major challenge in VCSEL fabrication.

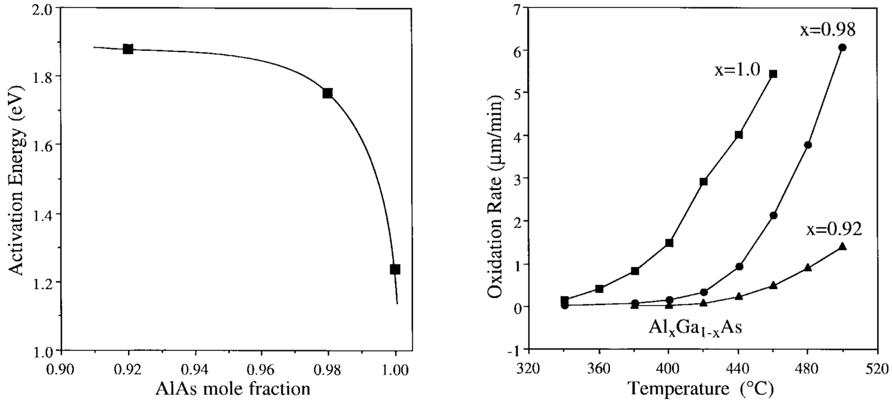

Figure 3.12: The dependence of the reacactivation energy of the reaction on the Al-fraction (left), and the dependence of the rate on the temperature, from [102].

3.7.3 Oxide properties

Measurements in [105] show that the oxide formed is a polycrystalline γ-phase Al_2O_3, with a grain size of an average of 4 nm, with no directional growth preference relative to the unoxidised lattice. The interface with the unoxidised AlGaAs material is a 10 nm to 20 nm amorphous layer. A conversion to fully-dense Al_2O_3 would be expected to lead to a 20% reduction in the volume of the oxide layer. Experimentally, a smaller shrinkage is observed, on the order of 7% [106]. This has a mechanical effect, and the strain is an important factor in the aging reliability of VCSELs. Dark line defects (DLDs) are one of the most prominent failure modes in oxide-confined VCSELs, and nucleate at the oxide layer before propagating to the active layer where they lead to a degradation of the laser performance [107].

Measurements of the resistivity of the oxide layer show it to be on the order of $10^{12}\,\Omega\,\mathrm{cm}$ [106]. The refractive index of γ-Al_2O_3 depends on the preparation method, [108] reports that it is in the region of $n = 1.45 \rightarrow 1.65$ for the emission wavelength of these VCSELs.

3.7.4 Oxidation equipment

The oxidation furnace in the ICS cleanroom is an Aloxtec conduction furnace. The temperature of the wafer is controlled by a heated chuck, and vacuum pressure is maintained to overcome the wafer bowing due to the compressive strain in the VCSEL stack compared to the substrate. Convection tube furnaces are used for higher-volume applications and allow multiple wafers to be processed simultaneously but without the ability to perform in-situ monitoring.

Figure 3.13: The Aloxtex conduction furnace used to perform the wet oxidation process on these VCSELs. The wafer is held by vacuum pressure against a heated chuck in the furnace. An infrared microscope image the sample during the processing.

Measurements of the oxide extent across nominally identical wafers carried out in a tube furnace and a conduction furnace performed in [109] show that most of the variation in the oxidation extent is due to the conduction furnace and the uneven heating of the sample. Improvements in the uniformity of the temperature and reaction conditions are possible using a rotating chuck, and a furnace of this type was used in parts of this project.

Figure 3.14: Measurement of the oxide extent using the infrared camera on the Alox. A machine vision software detects the edge of the mesa and the outside the oxide to determine the extent of the oxide. On the left is shown a circular test structure, which the measurement software can fit a circle to to determine the oxide extent in real time. On the right is shown a "multicellular" oxide aperture defined using etched posts.

3.7.5 In-situ oxidation monitoring

The oxidation changes the reflectivity of the DBR stack when imaged with a wavelength outside the stopband of the DBR, so the process can be monitored in-situ using an infrared camera focused on a test structure [110]. An infrared microscope camera illuminated with either a narrow source or a white-light broad spectrum shows a clear contrast between unoxidised material and the aperture.

Edge detection algorithms can determine the location of the interface between the oxidised and unoxidised material, as shown in Figure 3.14. This allows consistent measurements of the extent, and measurements in this way are accurate to within 0.5 μm compared to cross-sections imaged with a SEM or electrical measurements.

3.7.6 Simulation of oxidation shape

The Deal-Grove model is for a 1D structure, but for a structure with 2D geometry, if the oxidation process is carried out in the linear regime of the Deal-Grove model and is limited only by the chemical reaction rate at the oxide front rather than the diffusion of the water vapour through the existing oxide, the rate is constant. A simple model where the oxide propagates a fixed distance from each point on the boundary of the etch can therefore be used to show the intended oxide profile. In Figure 3.15 it is shown how the development of the oxidation

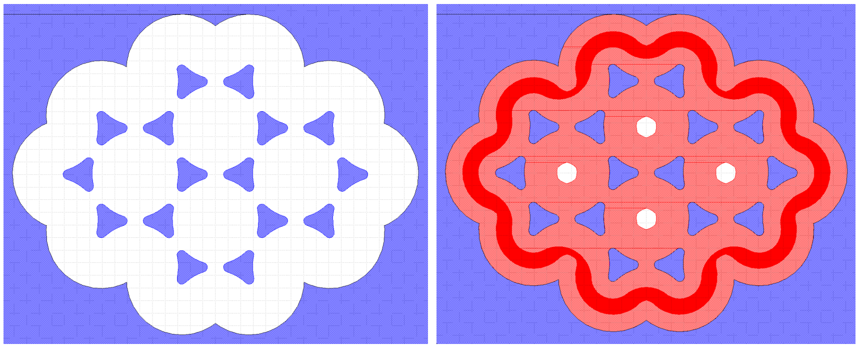

Figure 3.15: The simulation of the oxidation process. The left figure shows in blue the regions are where material is etched, and the white shows the mesa left behind. An arrangement of posts is etched into the mesa from which the oxide spreads to define the emission aperture. On the right is shown in red the simulated spread of the oxide. The nominal oxide extent for this design is 5.5 µm, leaving rounded hexagonal apertures.

front can be simulated in this way.

3.8 BCB planarisation and surface passivation

Benzocyclobutene (BCB) is a polymer used to planarise the structure after the oxidation so that the contact can be deposited across the mesa trench. The cured BCB does not dissolve in resist strippers, so it is compatible with subsequent lift-off steps. It also has the effect of sealing the sides of the mesa and passivating the sidewalls. BCB is spun on and then solvents are evaporated and the polymer molecules are cross-linked in a two-step curing process. This step is repeated twice so that the whole surface of the sample is covered with a BCB thickness of around 10 µm and the topography of the features is smoothed out. After this applications process, a reactive ion etching (RIE) O_2 / SF_6 etch is used to back-etch the BCB so that the p-contacts are exposed.

3.9 Ion implantation

The removal of material using an etch is a means of controlling where current can flow in the device. This can also be achieved by selective implantation of energetic ions into the material to change the electrical resistance, while preserving the optical and thermal qualities. Ion implantation in photonic crystal VCSELs defines a current aperture without using an oxide layer. The resistance between multiple closely spaced emitters in a laterally connected array can be increased to reduce their cross-pumping, so that their wavelengths can be individually controlled. This method was also used to create samples for investigating the gain spectrum using the segmented contact method, as discussed in 6.3.

Work was done to establish the lateral electrical resistance that can be achieved by ion implantation into VCSEL material. The key parameters of the implantation recipe are the dose of ions, the energy or energies of the implanted ions, and the annealing process. This process is intended to be compatible with the rest of the VCSEL fabrication, which has further high-temperature steps for the oxidation and contact annealing. It is difficult to effectively pattern a thick resist onto existing topography and so the ion implantation would ideally be one of the first steps in a fabrication process. The ion implantation was carried out at the UK National Ion Beam Centre (NIBC) in Surrey, with the assistance of Dr. Nianhau Peng.

3.9.1 Electrical isolation mechanism

Defects in the semiconductor crystal structure can be introduced by bombarding the material with energetic ions, which damage the crystal lattice, creating deep trap energy levels that prevent the movement of carriers. H+ (protons) are typically used because they do not lead to doping in the sample. Ion implantation using other species of ions is widely used as a method for introducing dopants into semiconductors [111].

The electrical conductivity of p-doped GaAs is approximately proportional to the doping concentration, and in the VCSEL structure the top layer is the most conductive, so as to make a good ohmic contact. An aperture to control the vertical movement of carriers can be defined with a single thin insulating layer (analogous to an oxide layer), but lateral isolation requires every layer of the sample to be insulating. Multiple implantation energies can be used to introduce vacancies into the structure at a range of depths.

3.9.2 Penetration depth

The penetration depth is determined by the energy of the ion, which is accelerated towards the target by an electric field. SRIM (Stopping and Range of

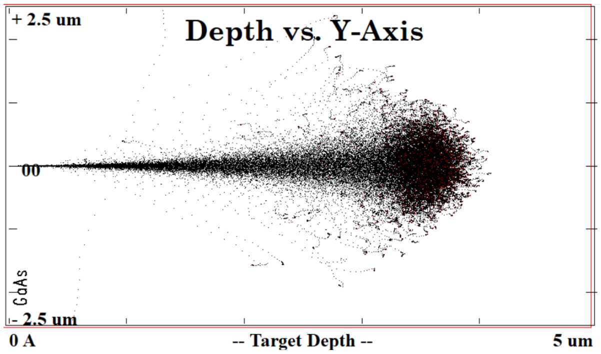

Figure 3.16: SRIM models the lateral straggle of the ions. As the ions travel through the material, they lose energy, and their interaction cross section increases so their mean free path decreases. Most of the damage is therefore due to the ions towards the ends of their travels.

Ions in Matter) [112] is a free software that can determine the relationship between the energy of the incoming ions and their travel distance and damage distribution in the target, and the extent of the lateral straggle, as shown in Figure 3.16. Srimulations were used to inform the range of energies for the ions and the thickness of the photoresist required to mask treatment with ions. The penetration depth of the ions into the sample with energy is shown in 3.17, and the resulting distribution of damage in 3.18.

SRIM models the interaction of the incoming ions with the atomic nuclei of the target material, so the key parameters are the atomic weight of the target elements (which for most parameters is much heavier than that of the H+ ions), the stoichiometry, and the density. For simplicity, a weighted average of the composition of the VCSEL was used as a target, and it was found that the implantation depth was not especially sensitive to the material composition.

To model the photoresist, PMMA was used, which has a density and elemental composition similar to that of most polymer-based photoresists. After calculating the energy required for ion implantation to the desired depth of around 3.5 µm in the sample, the resist thickness required to stop ions with that energy was found. A thick resist (AZ2070) spun on at 3000 rpm has a nominal thickness of 7 µm, and the actual thickness of the resist was measured as 7.6 µm using a profilometer.

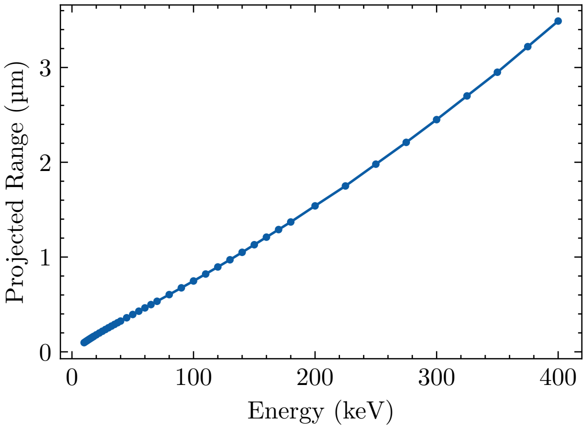

Figure 3.17: The relationship between the implantation energy and the penetration depth into the material. Energies of up to 400 keV are available with the equipment used for this implantation, at the NIBC higher implantation energies of up to 2 MeV. An implantation energy of 400 keV energy can achieve a penetration depth of around 3.5 µm, which is the depth of the active region in these devices.

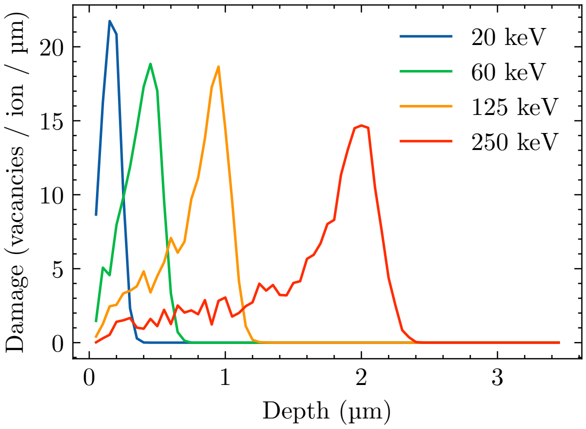

Figure 3.18: Multiple implantation energies can be used to introduce vacancies into the structure at a range of depths to achieve lateral isolation. Each ion creates a significant number of vacancies.

3.9.3 Dose

In an intact crystal lattice, the structure has a strong tendency to repair itself when a defect is introduced by an ion, leading to a non-linear relationship between the dose and the level of damage the sample is subjected to. The dose required also depends on the ion energy, as high-energy ions can cause secondary cascades of collisions by imparting enough energy to atoms in the target material. [113] contains experimental values for electrical isolation in p-doped GaAs. Figure 3.19 has values for the relationship between the dose and the sheet resistance of p-doped GaAs implanted with H^+ at an energy of 400 keV. Based on these results, a dose of $2 \times 10^{14}\,\mathrm{cm}^{-2}$ was used for all energies. SRIM calculations shown in Figure 3.18 estimate that each ion creates ≈ 10 vacancies / micron, with this dose of ions that corresponds to $2 \times 10^{18}\,\mathrm{cm}^{-3}$ vacancies, which is approximately the same as the density of dopants.

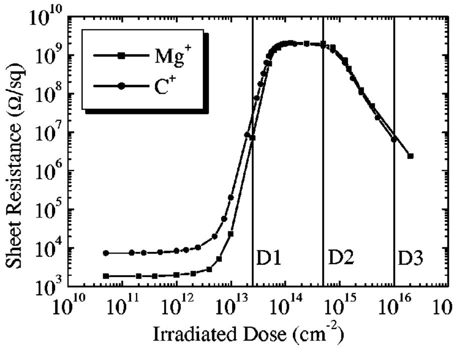

Figure 3.19: Dose measurements from [113], showing how the resistance increases with increasing dose, and then decreases again.

3.9.4 Annealing

The thick resist required to mask the implantation ions is patterned as one of the first steps, as the resist thickness and feature size would make it difficult to lithographically pattern the implantation region with existing topography on the sample. The subsequent contact anneal and wet oxidation processes happen at high temperatures, and so the ion implantation process has to be resistant to high temperatures. Annealing can partially restore the conductivity by repairing the ion-induced disorder in the crystal lattice, and so the dose of ions has to be sufficiently high that the effect of the implantation is not reversed by further

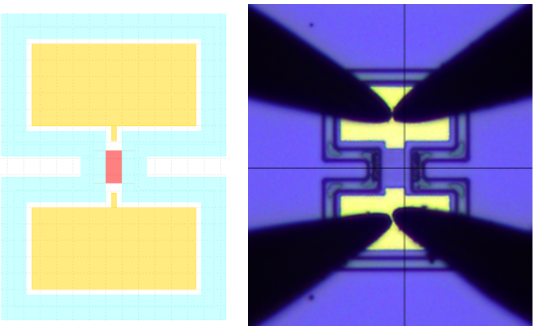

Figure 3.20: An ion implantation test structure, showing the design and a test structure. The bridge between the two contact pads is treated with the ion implantation (shown in red), the rest of the structure is masked off.

processing steps.

3.9.5 Test outline and motivations

Different implantation procedures were tested to show the effect of different implantation energies. A simple test structure consisting of two contact pads with an implantation region in the bridge that connects the contacts was designed, as shown in Figure 3.20.

The resistance of an area is due to the length to width ratio, so the increase in resistance can be found by fitting the inter-contact resistance as a function of the length/width ratio. The y-intercept of this fit represents the contact resistance. Implantation regions were designed with bridge widths between 10 and 25 µm, and lengths between 1 and 25 µm, representing the range of dimensions that might be relevant for closely spaced VCSEL emitters.

Using a 4-wire measurement of the IV from a voltage of $-2\,\text{V}$ to $2\,\text{V}$, the resistance can be found from the differential resistance. IVs measured in this way were linear, showing that the metal p-contact is fully ohmic, that there is no current path through the diode, and that there was a significant effect from self-heating changing the resistance of the material. IVs that were not linear, and where the resistance was anomalously high due to poor electrical contact, were filtered out from the analysis.

3.9.6 Change in resistance due to ion implantation

Using the formula for calculating the sheet resistance R_s from the resistance R through an area, R can be found in terms of the inter-contact resistance R_i and the sheet resistance.

$$R = R_{\mathrm{s}} \frac{L}{W} + R_{\mathrm{i}} \tag{3.1}$$

where L is the length of the implanted region and W is its width. The sheet resistance (with dimensions of Ohms) can then be found from the gradient, and the contact resistance, which should be the same for all samples, from the y-intercept.

Sample	**250 keV**	**125 keV**	**60 keV**	**20 keV**	$\Omega_{\mathrm{implanted}}/\Omega_0$
A	yes	yes	yes	yes	34
B	yes	no	no	no	2.6
C	no	no	yes	yes	1.9
D	no	no	no	yes	1.3

Table 3.1: The different treatment regimes and the resulting change in resistance.

The change in the resistance of sample A due to implantation is shown in Figure 3.21. With all four of the implantation energies, the resistance increase is much higher than for the other treatment processes.

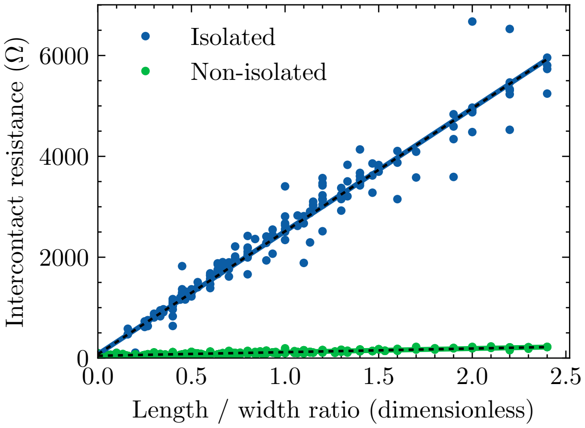

Figure 3.21: The increase in resistance due to implantation for sample A, where ions are implanted at the full range of energies. The sheet resistance increases from 72 Ω per square for the untreated material 2400 Ω per square for the isolated, an increase by a factor of 34.

3.10 Measurement of device characteristics

A number of performance characteristics determine the suitability of a VCSEL for an atomic sensor application. The LIV (Light-Current-Voltage) characteristics describe the electrical properties and the amount of optical output power for a given injection current. The properties of the lasing optical modes are their respective powers, wavelengths and beam profiles. The aim of this project is to find ways to increase the single-wavelength or single-mode optical output power of a VCSEL.

Measurements of the performance of the devices were largely carried out on-tile using an automated probe station, which allows simultaneous characterisation of a large number of devices with different design variations. A Cascade Summit 12000 200 mm semi-automated probestation moves the sample under investigation and provides temperature and environmental control. Electrical probes are brought into contact with the p-contact feed pads on the sample, and the back-side n-contact is held to the electrically conductive and temperature-controlled chuck by vacuum pressure. The devices to be investigated and the tests to be performed on each are defined in a LabVIEW program that controls the movements of the probestation and the operation of the test equipment. A sample in the probestation is shown in Figure 3.22.

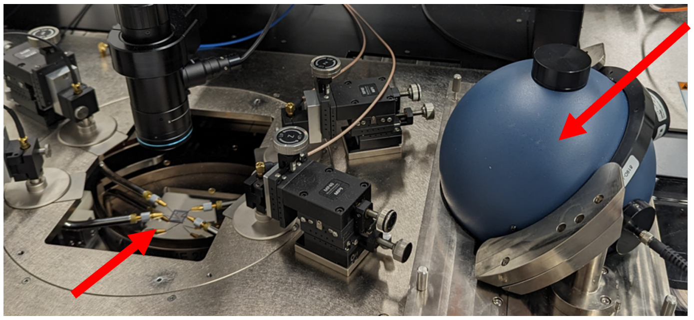

Figure 3.22: The probestation, showing the sample (indicated by left arrow) and integrating sphere that is placed over (right arrow.) The chuck manipulates the sample with a high degree of positional accuracy, bringing it into contact with the electrical probes.

3.10.1 Electrical measurements

The current-voltage (IV) characteristics of a VCSEL define how much current flows for a given voltage. The IV characteristics are due to both the ohmic series resistance and the potential difference across the diode. The series resistance of the VCSEL can be estimated from the asymptote of the differential resistance. In principle, the diode and series resistance can be modelled by the diode equation with an ideality factor, but this model with freely varying parameters typically does not describe the form of the experimentally measured IVs well.

A source-measure unit (SMU) controls either the current or the voltage, and then measures the other parameter. Laser diodes are typically tested with current sourcing, as the optical output power is normally reported as a function of current. 4-wire measurements are a way to accurately measure the voltage supplied to a device by removing the resistance associated with the leads and the probe contact with the feed, by using different set of probes is used to measure the voltage and to supply the current. A pulsed current source can also be used to approximate isothermal operation.

3.10.2 Measurement of optical power

The total optical power output can be measured using an integrating sphere. The output light from the VCSEL is coupled into a portal in the sphere, and then scattered repeatedly so that its intensity is averaged out over the whole inside surface of the sphere. A photodiode and optical power meter (Thorlabs PM100USB) measures the optical intensity, and based on the calibrated properties of the integrating sphere a true optical power for the VCSEL can be reported.

3.10.3 Optical spectrum

For this application, we are seeking devices that exhibit single-mode lasing. The side-mode suppression ratio (SMSR) is the ratio of the optical power in decibels between the first-order peak and the next higher-order peak. Light is collected for spectral measurements by coupling the VCSEL beam into a fibre, or tapping a fibre from an integrating sphere. Fibre-coupling captures more of the light, but different modes may be coupled selectively relative to others.

The optical spectrum can be measured with a spectrograph or optical spectrum analyser (OSA). A scanning OSA (here a Yokogawa AQ6373E) uses a moving diffraction grating as a monochromator with a very sharply defined passband. By scanning over the selected wavelength range, a selectivity as good as 0.02 nm can be achieved, with very good suppression of stray light, and in this way a true measurement of the SMSR can be performed.

A spectrograph (here an Andor Shamrock 750 with an iDus DU490A InGaAs photodetector) uses a grating in a fixed position to distribute the light onto a line camera in Czerny-Turner configuration, performing the measurement with a single exposure. This is much faster than a scanning OSA, as the measurement is performed in a single exposure with an integration time of a few seconds.

3.10.4 Threshold and rollover current

The threshold condition of a laser is when the round-trip modal gain is equal to the modal loss. The total amount of optical output power increases dramatically as the device transitions from a regime where most of the light is produced by spontaneous emission to one where stimulated emission dominates. Several methods can be used to calculate the threshold current. A method given in Blood [51] defines the threshold current as where the second derivative of the L-I is at a maximum. Other methods are to find the intercept of the straight-line part of the lasing L-I with the x-axis, or the intersection of fits to the spontaneous and lasing regimes. The optical output of a VCSEL below threshold is low due to the small spontaneous coupling coefficient β, so different methods of calculating the threshold current produce very similar results.

The thermal rollover is the current at which additional current injected into the device results in a decrease in the optical power, due to the effect of self-heating on the optical output power. The turn-off current is the temperature at which the optical output drops almost to 0.

3.10.5 Beam profile and divergence

An beam profiler (Ophir WB-I) was used to determine the divergence of the output beam. The divergence angle of a VCSEL is a property of the optical cavity. The quality of a beam can be expressed by a parameter M^2 that expresses its deviation from an ideal Gaussian beam.

3.10.6 Cavity temperature

The cavity temperature of a VCSEL can be measured from the wavelength shift of the fundamental mode. This is used for determining the self-heating and calculating the thermal resistance. The wavelength change with temperature $\partial\lambda/\partial T \approx 0.07\,\mathrm{nm\,K^{-1}}$, which is mainly ($\approx 90\%$) due to the change in refractive index with temperature, and to a smaller extent due to the thermal expansion of the stack ($\approx 10\%$) [54].

3.11 Pulsed measurements and heating

Pulsed measurements are used as a proxy to isothermal operation so that the characteristics of the device without the influence of temperature changes can be measured. Temperature increases have a number of effects on VCSEL performance, which are discussed further in Chapter 6. Typically, a repetition rate on the order of a microsecond is used with a duty cycle on the order of 1%. A pulsed current source (Keithley 2520), with impedance-matched coaxial cables and test probes, is used to maintain signal integrity [114].

The pulse length is chosen as a balance between maintaining the integrity of the pulse so that it is flat-topped, without causing self-heating. Parasitic capacitance and inductance are present in the coaxial cables and the connections of the experimental setup. The rise of the signal is measured on an oscilloscope connected in parallel with the VCSEL, which measures the potential across the device.

3.11.1 Simulation of heating during a pulse

Due to the very small pumped region of VCSELs, the heat density is very high and so the temperature gradients in the device are high. The thermal response time of the VCSEL is less than a microsecond [115], but pulses of this length cannot be achieved with sufficient integrity on the equipment used here.

An estimation of the heating due to a pulse can be made from solving the heat equation. In a medium with no convective flow, the evolution of the temperature distribution with time is given by Poisson's equation. In three dimensions this is given by

$$\nabla^2 T(\mathbf{x}, t) = \frac{1}{\alpha}\frac{\partial T}{\partial t}. \tag{3.2}$$

where the thermal transmittance α, combines the heat capacity c_p and thermal conductivity k along with the density ρ.

$$\alpha = \frac{k}{\rho c_p}. \tag{3.3}$$

Solving this for a pulse of heat with energy Q_p deposited instantaneously at the origin at time 0, the temperature distribution as a function of time elapsed since the pulse t_p is given by

$$T(r, z, t_p) = \frac{Q_p}{\rho c_p 8(\pi \alpha t)^{3/2}} \exp\left[-\frac{r^2 + z^2}{4\alpha t_p}\right] \tag{3.4}$$

For a constant $P(t) = P$ to represent a pulse of finite duration, Equation 3.4 can be integrated to construct the heating at a point as a function of time t after a power P is turned on, which is given by

$$T(r, z, t) = \frac{P}{4\pi k\sqrt{r^2 + z^2}}\left[1 - \operatorname{erfc}\left(\sqrt{\frac{(r^2 + z^2)}{4\alpha t}}\right)\right] \tag{3.5}$$

where erfc(x) is the complementary error function.

Using this relationship it is possible to estimate the highest temperature that is reached when a physical pulse of finite length is supplied to the device, which occurs at the end of the pulse. In this model, all the heat is generated at the origin, which results in a temperature of infinity at that point, whereas a more sophisticated model would have an extended heat source, but at radii greater than the size of the active region the results are approximately the same. 6 µm aperture device supplied with 6 mA of injection current corresponding to ≈ 10 mW of thermal power, a 10 µs pulse results in 10 °C of heating.

The heating due to different pulse lengths and duty cycles can be measured from the wavelength shift. Measurements of this are shown in Figure 3.23, and it can be seen that the heating is not a strong function of the duty cycle but is a strong function of the pulse length. As the pulse length increases the VCSEL approaches the steady-state condition, and this can be seen in the small change in wavelength as the pulse is increased from 10 to 20 µs. A 10 µs pulse results in a measured wavelength shift of around 0.8 nm, corresponding to a temperature increase of 11 °C, in good agreement with the (very approximate) estimate of the heating. The temperature change during the pulse means that the spectrograph measures a broadened spectrum, increasing the uncertainty in the peak wavelength.

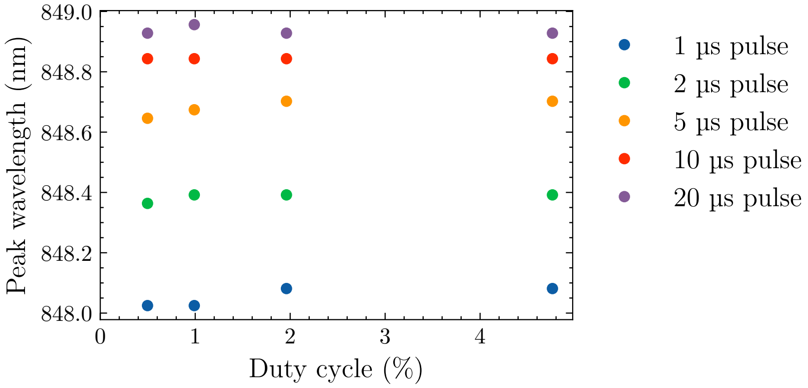

Figure 3.23: The measured wavelength as a function of pulse length and duty cycle.

Chapter 4

Experiments on multi-emitter VCSELs

Figure 4.1: A test structure which illuminates when a current is applied. On the left is shown the mask layout, the right two figures show fabricated structures which illuminate when current is applied.

4.1 Scaling of VCSEL output power by use of multiple emitters and photonic crystals

The overall aim of this project is to investigate VCSEL designs that better meet the application requirements for use in atomic sensors. Novel VCSEL devices were fabricated and characterised to investigate approaches that could provide higher single-wavelength optical output power than conventional oxide-confined single-mode VCSELs, which only marginally meet the application requirements, particularly in terms of optical power. Other approaches to enhanced single-mode power in VCSELs are discussed in Section 2.4.

Multiple nominally identical closely spaced single-mode emitters are explored as a route to scaling the optical output power. The optical cavity in a VCSEL has a high Q factor compared to an edge-emitting laser with mirror reflectivities above 99.5%, which means that a small amount of feedback between emitters from evanescent mode spreading can result in a supermode that is a combination of the individual cavity modes. Two different approaches to evanescent coupling were investigated, and the results are presented in this chapter. Closely spaced arrays of single-mode emitters are demonstrated as a route towards higher on-axis power. Using a pattern of etched posts, nearly circular oxide apertures can be defined, and the properties of devices fabricated in this way are presented here.

Photonic crystal VCSELs without an oxide aperture were also investigated. Photonic crystals are a different approach to optical confinement, permitting an increase in the lateral size of the active region of a single-mode device. Tests were performed on devices to understand the operation of a photonic crystal VCSEL and how they differ from oxide-confined ones. Future work will attempt to develop a photonic crystal VCSEL with tunnel junctions for carrier recycling, but this requires an understanding of the properties of the photonic crystal and the additional contribution to the refractive index profile from heating and carrier effects.

4.2 Dumbells and bow-ties

Novel “dumbell” and “bow-tie” devices were fabricated to investigate whether evanescent coupling, seen as a power enhancement or extended region of emission at the same wavelength, could be measured for certain combinations of the injection current supplied to each emitter. The designs have two emitters connected by a bridge region, as shown in 4.2. The bow-tie devices are inspired by other coupled devices [84], and by the use of angled facets to set up a total internal reflection condition for a laser cavity [116]. In [84], an arrangement of two VCSEL cavities has a characteristic resonance that is used to provide enhanced modulation performance The dumbell design was motivated by the aim of keeping the oxide apertures more similar in shape to conventional circular emitters, to preserve the Gaussian emission profile. In [79], very closely-spaced teardrop-shape apertures are used to achieve evanescent coupling. The emitter designs examined here have the apertures further apart, which reduces the mutual self-heating effect, and the aim of the experiments was to examine what coupling could be observed.

4.2.1 Design

The bridge provides a structure through which the two emitters are connected and can potentially couple, due to the containment of light in the cavity region of the structure by the DBR mirrors. The presence of the bridge in the mesa leads to a slight teardrop shape in the oxide aperture, which are sized to be single-mode with a nominal aperture diameter of 3 µm. A view of the devices is shown in Figure 4.2. Variations with different inter-emitter spacings, emitter dimensions, and with and without electrical isolation between them were fabricated.

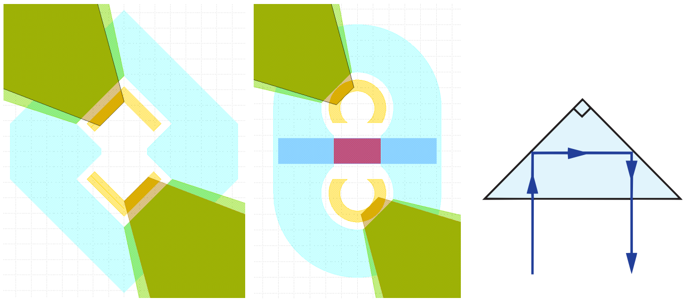

Figure 4.2: The mask design for the bow ties (left) and dumbells (centre). Shown in light blue is the mesa etch, which defines the shape of the mesa (in white). The electrical feed and p-contacts are shown connecting to mesa from above and below. (Right) how total internal reflection in a right-angled prism acts as a mirror, providing inspiration for the bow-tie design.

The critical angle θ_c for total internal reflection from light that goes from AlGaAs to the surrounding BCB polymer is less than 30°, so a right-angle prism supports total internal reflection. This means that there is the possibility of an in-plane optical mode confined by the DBR mirrors that passes through both aperture regions. Coupling between these in-plane modes and the vertical modes in the emitters sets up the possibility of a coupled super-mode. The intensity of the evanescent tails of the optical modes in each emitter can be calculated using a simulation software or estimated to decay with a characteristic length on the order of the aperture radius, which suggests that only a very low level of coupling will occur. However, due to the effects of material roughness and scattering from the oxide aperture, the amount of light scattered out of the cavity modes could be higher than this estimate. The right-angled ends were intended to enhance this effect if it was sufficiently strong.

4.2.2 Electrical isolation between emitters

Individual control of the injection current to each emitter can be used to vary the wavelength by variation of the self-heating of each emitter. For emitters on the same mesa, additional resistance between emitters is required to prevent significant cross-pumping through the p-DBR. Maintaining as much as possible the optical properties of the structure is desired so that the coupling between the emitters can take place. A similar procedure is used to control the flow of current for structures fabricated for measurements with the segmented contact technique [117].

In these devices, electrical isolation was achieved by a shallow etch into the p-DBR. The electrical conductivity is highest in the cap layer, so as to make a good ohmic contact. For p-doped GaAs, the electrical conductivity is approximately linear with the doping concentration, so the reduction in the inter-contact electrical conductivity can be estimated from the fraction of all the p-dopants that are removed in the top mirror.

Measurements of the inter-contact resistance for devices with and without the isolation etch show that the inter-contact resistance increases from 60 to $180\,\Omega$ with the etch. Above the diode turn-on voltage of $1.6\,\mathrm{V}$, the differential resistance of the VCSEL is around $50\,\Omega$, and so with the etch the inter-contact resistance is sufficiently high that there is independent control of the current injected into each aperture. A view of the isolation etch is shown in Figure 4.3.

4.2.3 Multiple current source optical power measurements

Measurements of the PIV properties were carried out with two current sources to power the emitters individually. This is similar to a measurement carried out on photonic crystal VCSELs, which observed a power enhancement in the regime where optical modes in two separate emitters couple into a single super-mode [83]. Variation of the injection current into each of the emitters is used to control

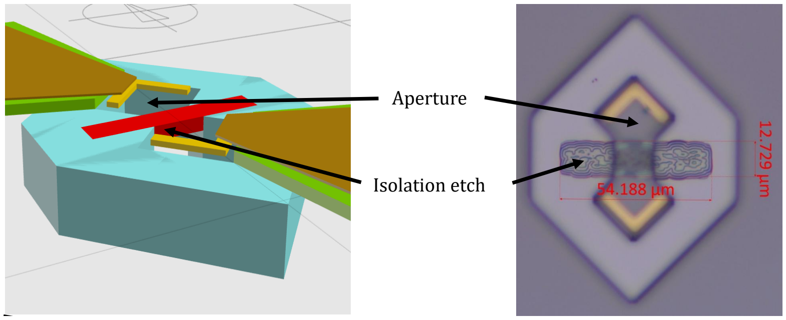

Figure 4.3: A view of the isolation etch in a bow-tie device. The mesa etch has been patterned in photoresist but the etch has not been carried out. The mesa etch penetrates through the active region, but the isolation only penetrates partly through the mirror. The partial removal of the p-mirror increases the electrical resistance by a factor of over 3, allowing a higher degree of control of the amount of current injected into each emitter.

the wavelength tuning, with a strong interaction seen when approximately the same injection current is applied to each emitter. The coupling between modes occurs when the wavelengths of both emitters are matched and so photons can be scattered between modes.

The amount of self-heating of each emitter varies as a function of the injection currents I_1 and I_2 to each emitter, and the optical output power of the emitter can be mapped out in the space of $I_1 - I_2$, as shown in Figures 4.5 and 4.6. Along diagonals where the current into each emitter is increasing at the same rate and so the emitters are heating at approximately the same rate, so if there is a coupling interaction between the optical modes in each emitter that is wavelength-dependent, it will persist along those lines. Measurements were performed with an additional current source that delivers a fixed I_2 while I_1 varies, before both sources are switched off and I_2 is incremented.

The optical output power as a function of current for a diode laser is approximately linear, due to pinning of the carrier concentrations when the device starts lasing. Subtracting this background optical power (by taking a fit of the linear part of the P-I) from the total measured power shows the changes in power due to interactions between the emitters.

To see the effect of the power enhancement, the difference in the measured power from the background trend can be plotted. The background trend is for the optical output power to increase approximately linearly with injection

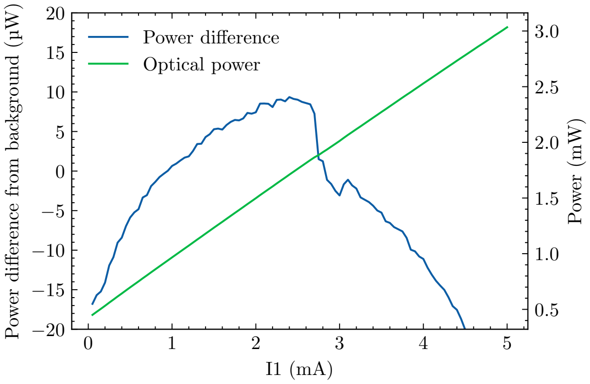

Figure 4.4: The power difference, which is the measured optical power minus a straight-line trend fitted to the data. As well as the background trend for the differential efficiency to reduce at higher currents due to self-heating, there are other features in the data which persist at different current combinations into each emitter. This measurement was taken at an I2 of 1.5 mA from the device shown in Figure 4.6, which intersects with a distinctive diagonal feature that results in an increase and then dip in the power at a current of around 3 mA.

current, with self-heating causing slight changes to the differential efficiency due to gain-tuning and leakage effects. This straight-line trend can be subtracted from the measured PI, as shown in Figure 4.4, to give a measure of the difference in power due to any coupling between the emitters.

The results of these experiments are shown in Figures 4.5 and 4.6. The measurement is performed in such a way that the current to one emitter is kept constant (I_2) and the other (I_1) is varied, and then the background is subtracted from each of these individual measurements. This means that there is an asymmetry in the resulting profile because of the order in which these processes are carried out.

A measurement artefact can be seen at some values, possibly due to an interaction between the current supplies, which are simultaneously trying to source a current through parallel emitters which have some electrical connection between them. Only a very weak interaction with a small power enhancement ($\approx 10\,\mu\text{W}$) was found for a small number of devices, so no analysis could be done of the effect of different mesa designs on the strength of the interaction. The magnitude of the power deviation is on the order of 10 µW, compared to a power output from each emitter of 1 mW. Analysis of other emitter designs

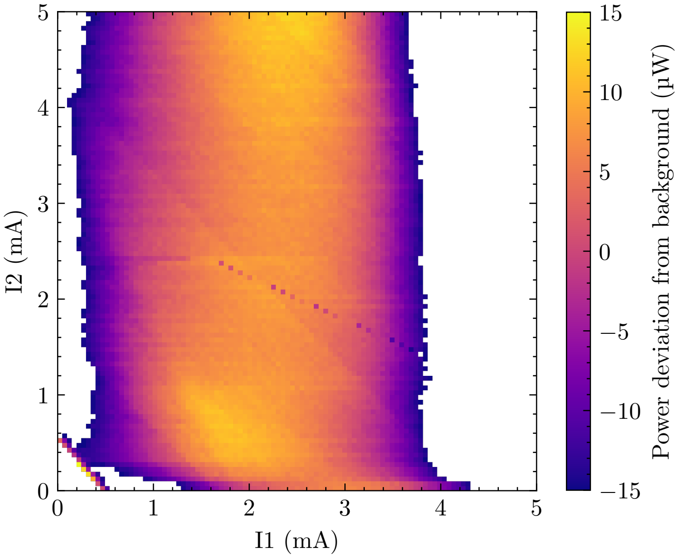

Figure 4.5: Device with no interaction seen between the emitters in the $I_1 - I_2$ space.

in the following sections suggests that differences in the emission wavelengths due to fabrication variations could be responsible for the low fraction of devices that show any interaction. The device shown in Figure 4.6 that shows an interaction is a bow-tie design with a centre-centre distance between the emitters of 12 µm, whereas other evanescently coupled emitter designs such as [79] have the emitters closer together (with an aperture centre-centre distance of up to 8 µm).

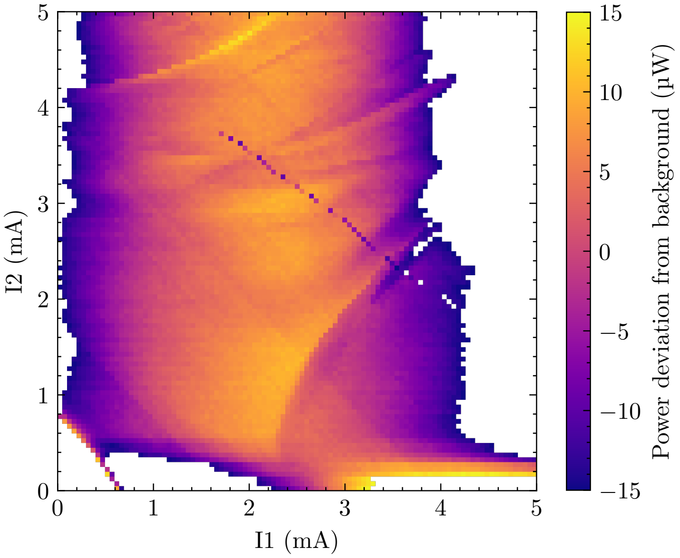

Figure 4.6: A device where an interaction is seen between the modes, with features along diagonals in the $I_1 - I_2$ space that correspond to the emitters heating at the same rate.

4.3 Closely spaced emitters - “multicellular”

The coupling strength of evanescently coupled emitters is dictated by the characteristic decay length of the optical intensity, which is approximately the radius of the emitter, around 1.5 µm for a single-mode device. To achieve stronger coupling between emitters, a design with more closely spaced emitters was proposed. This is achieved with etched posts patterned into a larger mesa, which define the front from where the oxide spreads. Arrays of emitters using etched posts have been demonstrated in other works, but with different post and aperture configurations to those here [118][119]. The emitters discussed here used a hexagonal arrangement of posts, with concave rounded edges on the posts to achieve a more-circular aperture shape.

In this section, emitters with a rounded hexagonal shape defined with rounded triangular etched posts are investigated, as this allows a close packing of nearly-circular individual emitters, which provides a way to investigate the possibility of evanescent coupling between emitters. The scaling of the thermal resistance and turnoff current with the number of emitters is discussed later in Section 6.5. These closely spaced emitter designs are referred to in this section as the

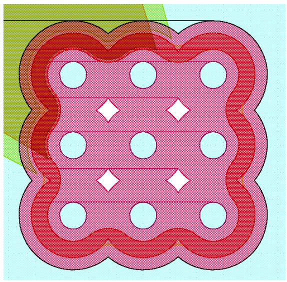

Figure 4.7: A square 4-emitter design. The rotational symmetry of the design means that all of the emitters have the same thermal resistance.

"multicellular" layout.

4.3.1 Device design

If the whole mesa is symmetrical, individual emitters have equal thermal resistance and so heat at the same rate, and the individual emitter wavelengths maintain the same separation (assuming stability of the parallel diodes). A symmetrical layout is possible for hexagonal arrays with 2 or 3 emitters, and for square arrays with 4 emitters (as shown in Figure 4.7). A 4-emitter hexagonal array (as shown in Figure 4.8) has nearly identical emitters, but is not rotationally symmetrical so the emitters in principle have different thermal conductivities. Hexagonal and square arrays also permit scaling to arbitrarily large arrays of identical emitters. There is no electrical isolation between the emitters in these designs due to the closer spacing, which does not leave any space for an isolation etch or implant. The multicellular designs are all common-contact designs.

The oxidation rate is limited by processes that occur at the oxide front, rather than by diffusion of the steam into the material at the etch boundary. This means that the oxide develops to the same extent from every point on the etch boundary. A rounded concave shape is used for the etched posts in the hexagonal layout, which transfers to a round aperture shape. The curvature radius is 0.5 µm, which is the smallest feature that can typically be patterned with i-line lithography.

These features are smaller than those present in other VCSEL etch designs. A thinner resist from a higher spin speed, higher exposure dose, and longer development time were used so that the smallest features had the correct di-

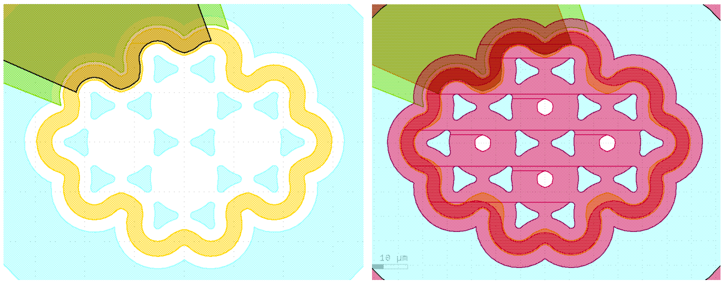

Figure 4.8: Hexagonal multiple-emitter layouts, showing the simulated oxide extent (in red) on the right, with the four apertures where the oxide has not reached. The etch is shown in light blue, and the gold ribbon around the edge is the p-contact. The use of etched posts to define the oxide shape allows the emitters to be placed more closely together. The overlap between the oxide fronts is a minimum of 1 µm to account for potential variations in the dimensions of the etch.

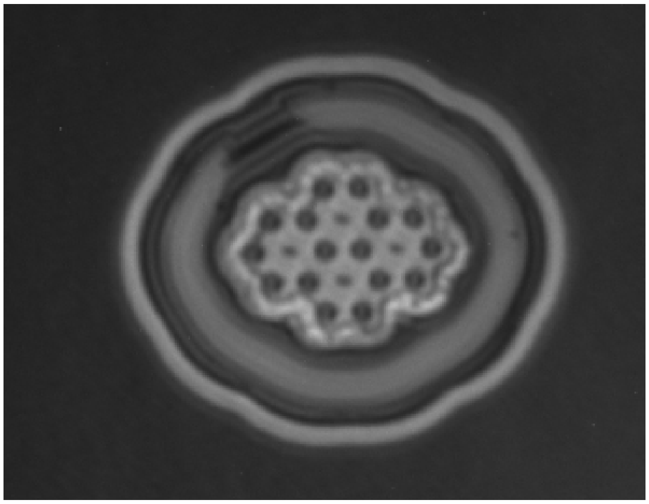

Figure 4.9: Infrared image showing the oxide apertures after oxidation. Oxidation test structures and a calibrated oxidation rate for a material from a SEM cross-section can be used to define the oxidation with an accuracy of ± 0.5 µm or better.

mensions. Etch tests were used to establish that the etch depth was sufficient to expose the oxidation layer in the structure. Dimensional measurements of the mesa structures verified that the dimensions of the etched features were transferred from the design. A shorter oxide extent of 5.5 µm was used in this design, whereas typical VCSEL designs use an oxide extent of around 10 µm. As the oxide front spreads in two directions, the overall size of the mesa is similar.

4.3.2 Individual emitter performance

The individual emitters have characteristics similar to those of a conventional single-mode emitter, with an optical spectrum dominated by a single Gaussian mode, and similar electrical properties despite the different p-contact design. The scaling properties with an increasing number of emitters can be investigated as 1, 2, 3, and 4-emitter designs were fabricated. The designs of a single-emitter multicellular device and a circular emitter with a short oxide extent are shown in Figure 4.10. The measurements of the optical spectrum were performed with a spectrograph and not an OSA, and so the SMSR is not representative, but both spectra are dominated by a single fundamental mode.

Both of the designs have a nominal oxide aperture of 3 µm aperture, which supports a single mode. Figure 4.11 shows a comparison of the optical spectra of the two designs. Figure 4.12 shows the IV and LI to rollover of the two designs. The multicellular device has a slightly larger thermal mass, so it rolls over at a higher injection current. The differential resistance of both designs is similar, and despite the multicellular design having the p-contact further from the aperture region, the differential resistance is slightly lower. Figure 4.13 shows the Gaussian emission profile of a single multicellular emitter at a current of 1 mA, corresponding to single-mode emission. The mode is Gaussian and on-axis with no obviously hexagonal features, suggesting that the oxide aperture is approximately circular.

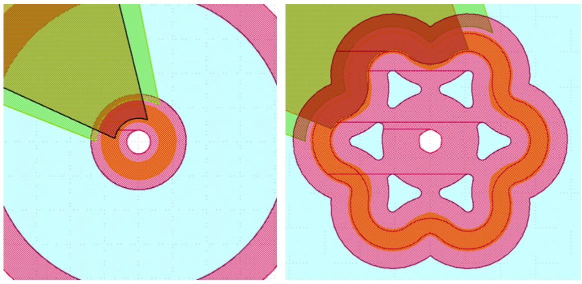

Figure 4.10: The design of a hexagonal-array single-emitter, and a conventional circular emitter with the same short oxide extent, with a nominal oxide aperture diameter of 3 µm and an oxide oxide extent of 5.5 µm.

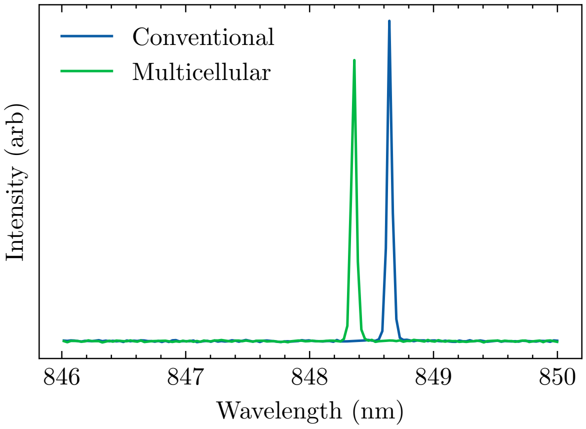

Figure 4.11: Comparison of the optical spectrum at 1 mA of equally-sized hole-defined and conventional mesa designs.

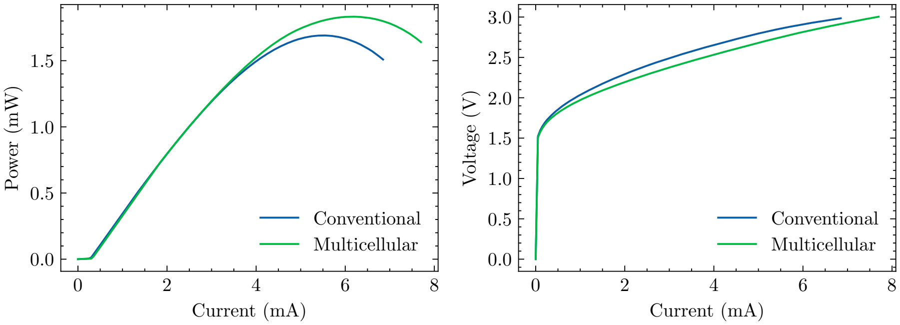

Figure 4.12: Comparison of the PI and IV of equally-sized hole-defined and conventional mesa designs.

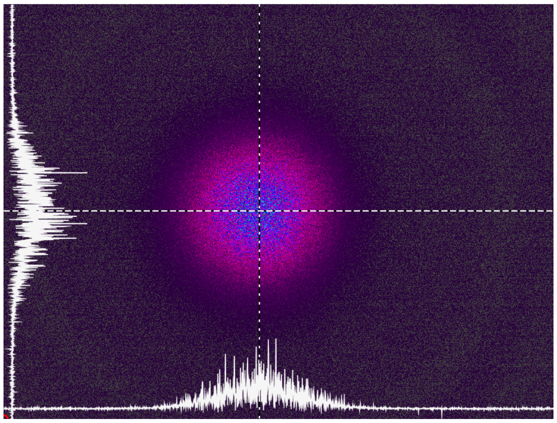

Figure 4.13: The far-field image of a single hexagonal emitter, at a current of 1 mA corresponding to single-mode output.

4.3.3 Spectra of multiple-emitter devices

When a multiple emitter device is supplied with an injection current of 1 mA to each aperture, the optical spectrum of a device shows that the individual emitters are lasing at different wavelengths. Any coupling interaction between the emitters is not sufficiently strong to make them lase at the same wavelength over an extended range of injection currents. This is due to material and fabrication variations between the emitters, and the instability of the arrangement of parallel diodes. Figure 4.14 shows the optical spectra of 2, 3, and 4-emitter designs with an average injection current of 1 mA supplied to each emitter. The spread of emission wavelengths does not appear to increase with increasing numbers of emitters, but is randomly distributed due to variations between emitters.

The wavelength range into which the laser power is concentrated is smaller for these designs than for equivalent-area larger emitters. The differences between the output wavelengths of each of the emitters, each of which is emitting primarily from the first-order Gaussian mode, is smaller than the wavelength differences between the different orders of mode present in a larger-aperture device, as shown in Figure 4.15. For a typical 4-aperture multicellular device with a nominal oxide diameter of 3 µm, the spread of wavelengths is within 1 nm, whereas for an equivalent-area 6 µm aperture diameter (28 μm^2 active area) the spread of optical modes is greater than 2 nm. The spectrograph resolution (0.03 nm) is limited so the optical output from each emitter cannot be resolved if the spacing of the emission wavelengths is close. Measurements of the far-field profile show that the emission is on-axis, as shown in Figure 4.16.

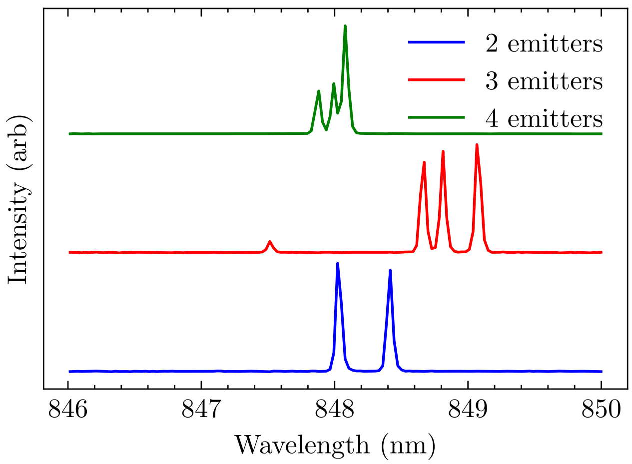

Figure 4.14: Spectra of 2, 3 and 4-emitter devices at 2, 3, and 4 mA, so that each emitter has an average injection current of 1 mA. The higher peak in the 4-emitter device is because two of the emitters are operating at the same output wavelength.

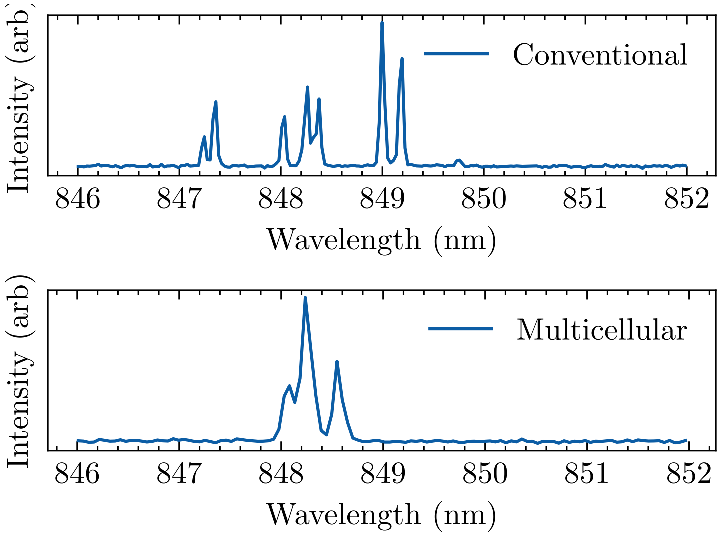

Figure 4.15: The spectrum from a 4-aperture multicellular device and equivalent-area conventional single-emitter device at a current of 4 mA, corresponding to single-mode emission in each of the emitters in the multicellular array. The spread of output wavelengths is less than half that for the multicellular design.

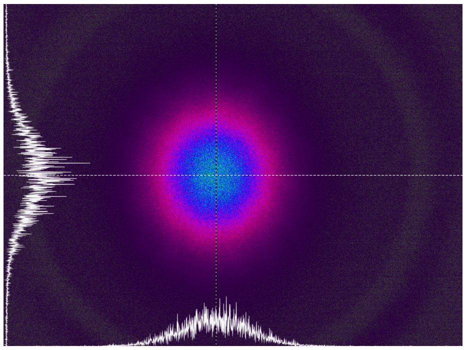

Figure 4.16: The far-field of a multi-emitter multicellular device is the sum of the Gaussian modes in each of the emitters, with the power concentrated on-axis.

4.3.4 Intersection of wavelengths

The multicellular devices have a single contact and so there is no way to individually control the wavelength of each emitter by modulation of the injection current. However, because of different current-wavelength tuning characteristics arising from small variations between the emitters, for some devices with two emitters the wavelengths of the individual emitters intersect at a particular current. A 2-emitter design as examined here is shown in Figure 4.17.

The properties of the optical output at the point where the emission wavelengths are equal can be investigated to look for a possible coupling effect. This was done for a 2-emitter device with a nominal aperture diameter of 3 µm where the output wavelengths were observed to intersect at a particular current. Preferential lasing of a coupled mode would manifest as a tendency for the output

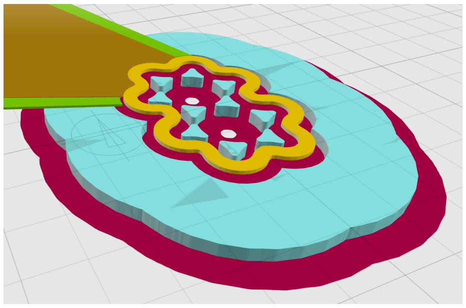

Figure 4.17: A two-emitter device as examined.

to be at a single wavelength over a longer range of currents, or a variation in the optical power from the linear background trend.

Figure 4.18 shows the evolution of the spectrum at a range of injection currents. At currents below and above an intersection current of 3 mA two peaks can be resolved, but at the intersection the emission wavelengths of both emitters intersect to within the resolution of the spectrograph. Figure 4.19 shows how an estimate of the width of the spectrum can be found by fitting a spline function to the spectrograph data. The spline provides a way of interpolating the data, which has a limited resolution compared to the width of the mode. This method means that separate peaks do not have to be resolved, as would be the case with fitting a Gaussian or Lorentzian function to each of the peaks. The FWHM can be found from the points in the spline fit that are equal to half the maximum of the spectrum.

Figure 4.20 shows the width of the spectrum as defined above, as a function of current. An extended region where the optical output of the device was narrower would indicate that a different mode, corresponding to preferential lasing of a coupled supermode between the cavities. A V-shaped profile would indicate that the peaks "pass through" each other with increasing current with no interaction. The flat bottom of this graph leaves open the possibility of some interaction between the modes. An interaction could lead to a reduction in the linewidth [120], but this cannot be measured using a spectrograph measurement.

Figure 4.21 shows the difference in the optical power from the background trend. The linear background trend in the P-I is removed by fitting a 5th-order polynomial to account for the slight effects due to temperature. This leaves the high-frequency components of the difference only, which have the characteristic of noise in the optical power measurement. The difference has the characteristic of measurement noise, and is 0.01% of the total measured optical power, putting a strong upper limit on the magnitude of any power enhancement due to a coupling effect for these devices.

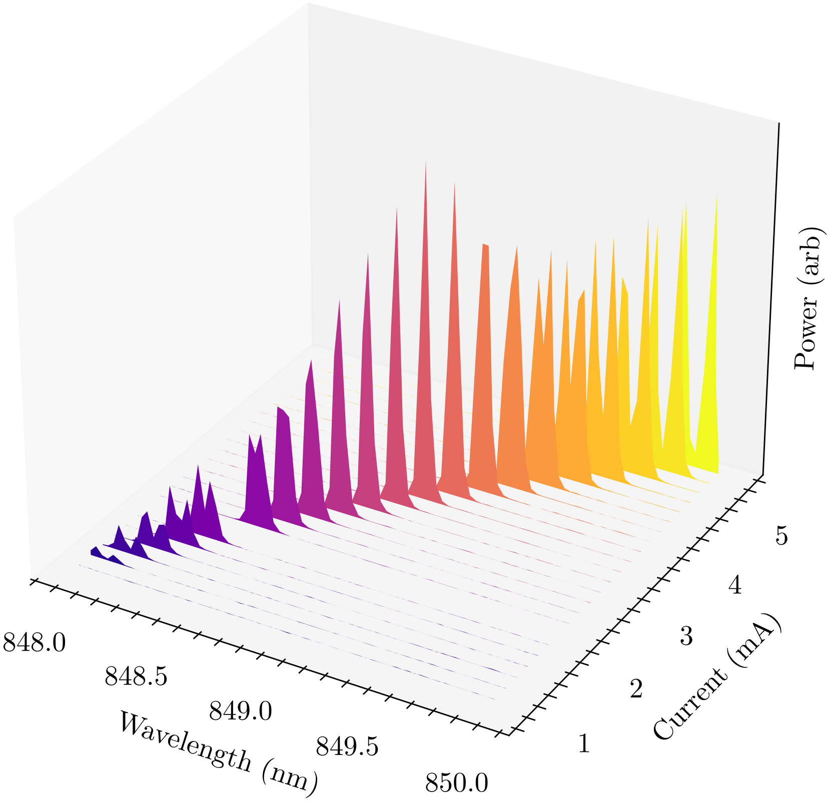

Figure 4.18: View of the optical power spectrum at a range of currents for the device illustrated in Figure 4.17.

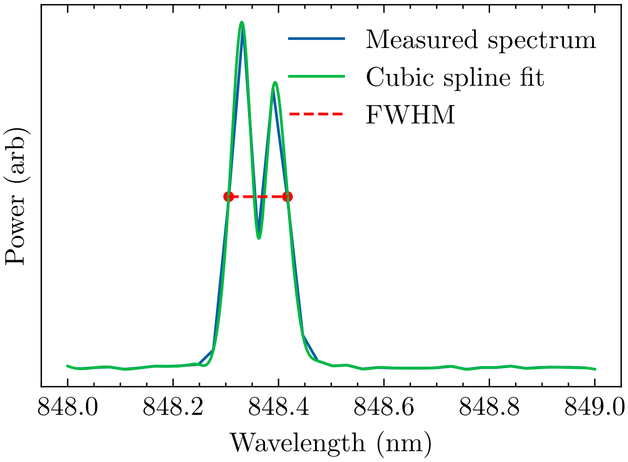

Figure 4.19: Estimation of the peak width from a cubic spline fitted to the optical spectrum.

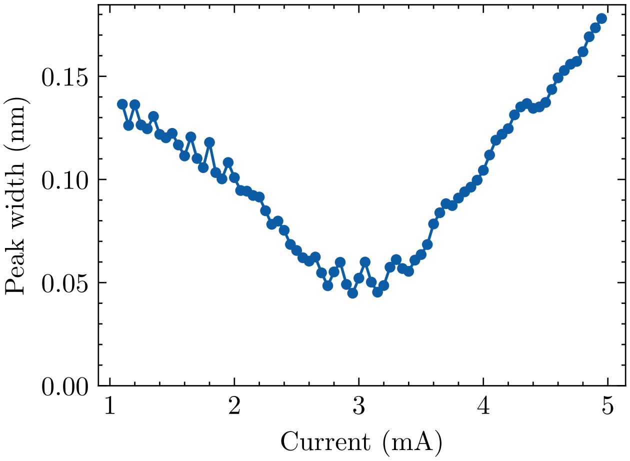

Figure 4.20: Measurement of the width of the spectrum of a 2-emitter 3 µm aperture device at a range of injection currents.

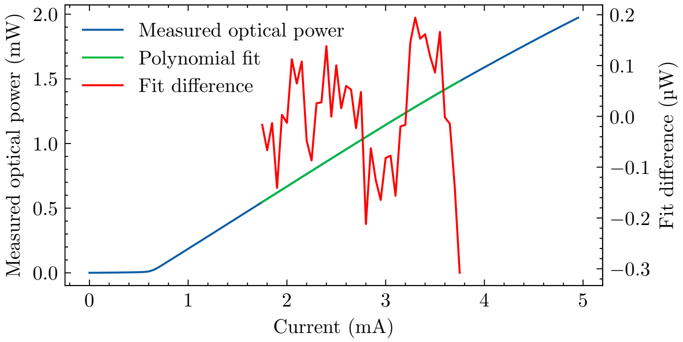

Figure 4.21: A PI measurement of this device through the region of the intersection shown above with the deviation from the background trend in the measured optical power. No change in the power is seen, suggesting that there is no coupling effect taking place.

4.4 Arrays of individual emitters

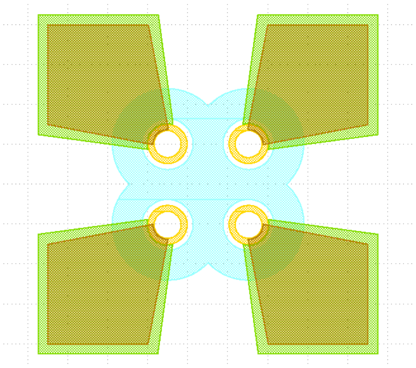

Figure 4.22: A view of the array design, with 4 conventional emitters spaced close together. The centre-centre separation between the emitters is 40 µm.

Variation between emitters means that each emitter in an array will lase at different wavelengths. An array design where the powered emitters can be selected for similarity after testing can result in a tighter spread of wavelengths, particularly if the injection currents to each emitter are controlled separately. An array design was fabricated with four individual emitters with separate contact pads in the same mesa trench, as shown in Figure 4.22.

The viability of this approach depends on the variation in the emission wavelength between closely-spaced emitters. This variation is due to material and fabrication variations that occur on a range of length scales. In this section, we discuss some of the considerations when two emitters are powered and the viability of this approach. This approach also requires a system for controlling the injection currents of multiple emitters so that they emit at the same wavelength, and the implementation of this was not explored.

4.4.1 Measurement of variation of closely-spaced emitters and tuneable range

The centre-centre distance of these array is 40 µm. Variations in the cavity wavelength happen at different length scales due to material and fabrication variations in the p-contact, etch dimensions, and material layer thickness and composition. These affect both the electrical resistance of the device, which changes its current-wavelength tuning coefficient, and the oxide aperture diameter, which affects the optical mode. From scans of the cavity wavelength over the wafer (discussed in Section 3.2.1) the gradient of the cavity wavelength over the part of the wafer these devices were fabricated from is on the order of $0.2\,\mathrm{nm\,mm^{-1}}$, so the expected variation between emitter wavelengths due to material variations is $\approx 0.008\,\mathrm{nm}$.

The tuneable range of each of the emitters is dictated by the current range over which the power output is at a useful level while retaining the single-mode characteristic. The resolution of the of the spectrograph is $0.03\,\mathrm{nm}$, and it is mounted on a vibration-isolating table to maintain its calibration between measurements. The temperature of the aluminium chuck the sample sits on is controlled with a PID and measured with an accuracy of $0.01\,^{\circ}\mathrm{C}$, and is sealed to prevent air currents from causing temperature instabilities when measurements are being taken. It is therefore possible to perform comparable measurements of wavelengths in different measurement runs, which is required to measure the four devices in each of the positions. The range of injection currents over which the device is single-mode and produces a useful amount of power is around $0.5\,\mathrm{mA}$. Given the current-wavelength tuning coefficient for these emitters of $\approx 1\,\mathrm{nm\,mA^{-1}}$, this means that around $0.5\,\mathrm{nm}$ of current tuning is possible. The spectra at a range of currents for a single emitter is shown in Figure 4.23. From fitting the wavelength as a function of dissipated thermal power, the thermal resistance of one of these emitters is measured as $6.6\,^{\circ}\mathrm{C\,mW^{-1}}$.

The distribution of the variation in the emission wavelengths between adjacent nominally-identical devices can be found. As shown in Figure 4.24, the distribution of wavelengths at an injection current of $1\,\mathrm{mA}$ has a median variation of $0.25\,\mathrm{nm}$. This is much larger than the difference expected due to the variation of the cavity resonance across the wafer, so this variation is attributed to differences in fabrication that affect the dimensions of the aperture and the ohmic resistance of the device. Fabrication with a larger sample (such as a whole wafer) or processes optimised for uniformity would lead to a smaller difference between emitter wavelengths.

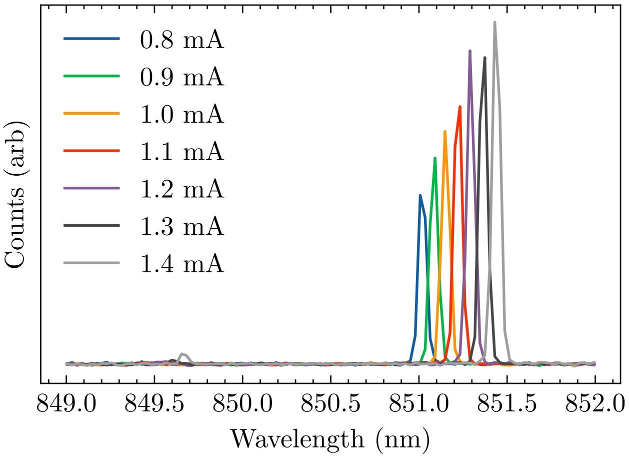

Figure 4.23: The thermal resistance of a single emitter is measured from the wavelength shift of the fundamental mode.

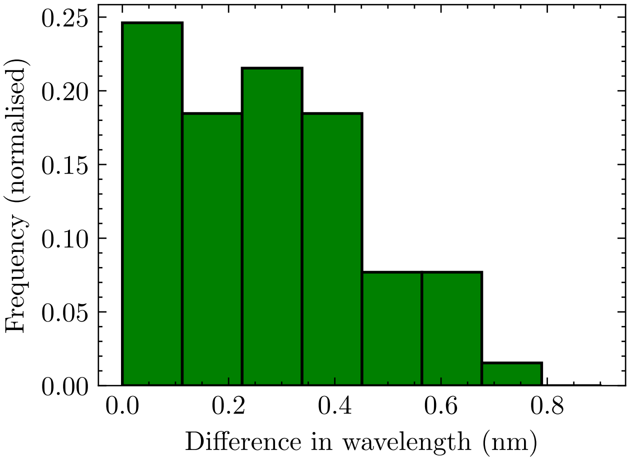

Figure 4.24: At a typical operating current of 1 mA, the variation between pairs of emitters in the same array is shown. These are 3 µm aperture diameter, nominally single-mode devices. The median wavelength variation between emitters is 0.25 nm.

4.4.2 Thermal influence of closely-spaced devices

The heating due to thermal interference between closely-spaced devices can be determined from a measurement of the change in the cavity wavelength due to heating when an additional nearby emitter is powered.

In Figure 4.25 a slight red-shifting of the cavity wavelength is seen when both emitters are powered due to the additional substrate heating. Fitting a peak function to both spectra, the measured shift is 0.023 nm, corresponding to a temperature increase of 0.3 °C. In this arrangement, each emitter has an injection current of 1.2 mA, corresponding to an optical power of 0.68 mW and a thermal power of 1.76 mW, and a temperature increase of 11.6 °C. The fraction of the temperature increase of one emitter that reaches another emitter less is 2.5%. The temperature increases with additional emitters are linear, so using all 4 emitters in an array results in an additional heating of less than 10%. This means that arrays of VCSELs such as these with a small number of emitters are not dramatically limited by thermal effects and arrays of this type are suitable for scaling. Typically VCSEL array used for applications such as material processing use large emitters, but the properties of emitters with a small number (< 10) emitters are less widely investigated [121].

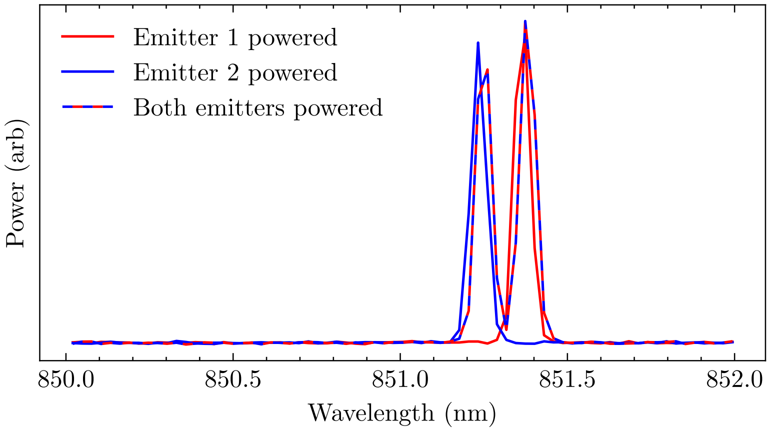

Figure 4.25: The change in the spectra when one or both emitters is powered is used to determine the heating influence that one emitter has on the other.

4.5 Photonic crystal VCSELs

The VCSELs discussed previously use an oxide aperture to guide the current and provide the optical confinement that defines the cavity modes. An ion-implantation-defined current aperture with photonic crystal mode control is an alternative way of defining the cavity modes and the active region. Devices of this kind were investigated at the University of Illinois Urbana-Champaign in collaboration with the group of Kent Choquette, and a view of such a device is shown in Figure 4.26.

In general, commercially produced VCSELs are oxide confined, as they retain a number a number of significant advantages over photonic crystal VCSELs including much better power conversion efficiency. However, there are many possible avenues for future exploration of photonic crystal VCSELs, such as coupled apertures [122], or using photonic crystals in conjunction with with stacked junctions, which have been shown to provide high power conversion efficiencies [123]. Related to but distinct from the photonic crystal VCSEL is the Photonic Crystal Surface-Emitting Laser (PCSEL), which uses a photonic crystal structure to outcouple light for vertical emission [32].

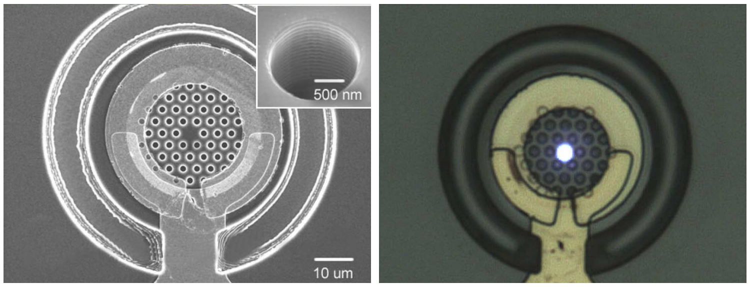

Figure 4.26: View of photonic crystal VCSEL as tested, with a SEM view of the fabrication and the photonic crystal holes, and the device showing the optical output. These VCSELs were produced by the group of Kent Choquette at the University of Illinois Urbana-Champaign. Adapted with permission from [91].

4.5.1 Simulation of photonic crystal modes

The lasing modes of the VCSEL are determined by the optical modes that are permitted by the photonic crystal. Simulations of the optical modes confined by the photonic crystal can be performed in a finite-element modelling software tool such as Lumerical, and this is typically performed in 2 dimensions as a full 3-dimensional simulation is intractable. Simulations previously carried out at the University of Illinois used representative values for the real and imaginary parts of the refractive index, as shown in Figure 4.27.

These refractive index values were arrived at from fitting experimental measurements of the optical spectra to simulations of the optical modes. The wavelength spacing between the fundamental and first higher-order modes as measured from the optical spectrum below threshold can be related to the respective effective indexes n_{eff} of these modes in a simulation. The introduction of a scattering loss increases the fundamental-first order splitting [42]. A fit of this splitting as a function of defect size was used to arrive at the imaginary index value of $0.0005i$ that represents the scattering. The threshold gain of $100\,\text{cm}^{-1}$ is represented by an imaginary component of the index of $-0.01i$ in the active region.

The real index value of 2 in the etched hole accounts for the partial extent of the etch into the stack, and so is effectively a weighted average of the refractive index experienced by the optical mode in the etch region. It was found that the characteristics of the device are not highly sensitive to the depth of the etch. The value of $\Delta n = 2 \times 10^{-3}$ corresponds to the index suppression due

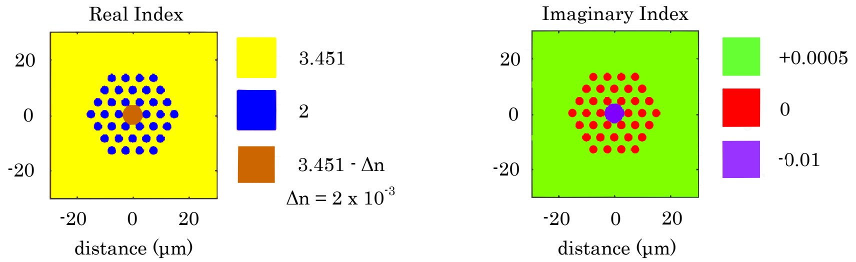

Figure 4.27: The real and imaginary parts of the refractive index in different parts of the waveguide model, adapted from [125].

to the threshold carrier density, of around $2 \times 10^{18}\,\mathrm{cm}^{-3}$. The effect of heating increases the refractive index, but measurement of the splitting is done at low currents to avoid thermal effects. These refractive index values have been used to model other photonic crystal designs, such as extended coupled arrays [124].

4.5.2 Measurements of device characteristics

Photonic crystal VCSELs with a range of hole centre-centre a and hole diameter b values were fabricated on epi-material with a nominal cavity wavelength of 940 nm. A range of emitter designs were fabricated on these samples, but here we discuss the results from single-hole defect devices with aperture sizes between 3.0 and 4.5 μm. Measurements were performed to establish the lasing performance of the devices for the purposes of making a comparison to conventional devices, and for establishing the maximum defect size which operates as a single-mode emitter. The LIV properties were measured using a photodiode attached to a microscope, and the optical output spectrum was measured using an optical spectrum analyser. The optical power measurement does not represent an absolute power as not all of the light is captured by the sensor.

4.5.3 PIV properties

Measurements of the PIV properties show a number of changes in the external efficiency, which were found to be repeatable for the same device. The optical power measurement is performed with a photodetector that measures the light collected by a lens placed in front of the emitter. The coupling efficiency from the emitter to the detector therefore changes as a function of the divergence angle,

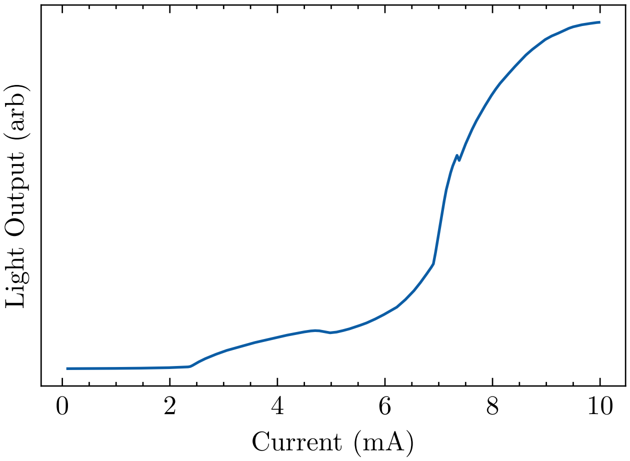

Figure 4.28: Optical output power for a device with a 4.25 µm defect size, showing a number of changes in the external differential efficiency. These are attributed to the measurement process, which changes the fraction of collected light as a function of divergence angle.

which changes with thermal lensing. These observed changes in the differential efficiency may not be real, and other investigations of photonic crystal VCSELs using an integrating sphere do not report such dramatic changes in the efficiency [126]. From the LIV, the dependence of the threshold current on the aperture size can be extracted. The LIV for a 4.25 µm aperture device is shown in Figure 4.28.

The threshold currents are much higher than those of oxide-confined VCSELs due to the larger active region that carriers flow through. The ion implantation aperture is $\approx 20\,\mu\mathrm{m}$ in diameter, much larger than the defect in the photonic crystal that confines the optical mode. This is because the lateral straggle of the implanted ions limits how the aperture can be defined. In contrast, an oxide aperture defines both the size and location of the optical modes and the path through which the current flows, so the apertures are the same size. The ion implantation aperture is larger than the mode to reduce the refractive index gradient from temperature and carrier effects. Figure 4.29 shows the threshold current as a function of defect size. The threshold currents are around an order of magnitude higher than those of oxide-confined devices due to the larger area through which current flows.

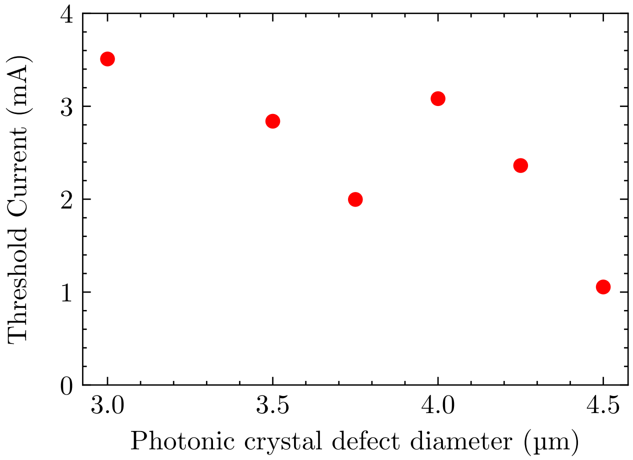

Figure 4.29: The threshold current as a function of defect size.

4.5.4 Sub-threshold spectrum measurements

Below threshold, spontaneously emitted light couples into a number of higher-order optical modes as well as the fundamental mode. However, only the fundamental mode lases due to the suppression by the photonic crystal of the higher-order modes. From the optical spectrum at injection currents below the threshold, the wavelength splitting of the modes can be measured, allowing the determination of the refractive indices used for the simulation of the optical modes. The fundamental Gaussian mode has the highest effective index, and so is the longest wavelength mode in the spectrum. At wavelengths higher than the fundamental mode, unconfined free-space modes can also be seen as “shoulders” in the spectrum, but these do not contribute to the optical output of the device. The measured far-field profile of this mode confirms that it is the fundamental Gaussian mode. A sub-threshold spectrum is shown in Figure 4.30, showing the mode splitting.

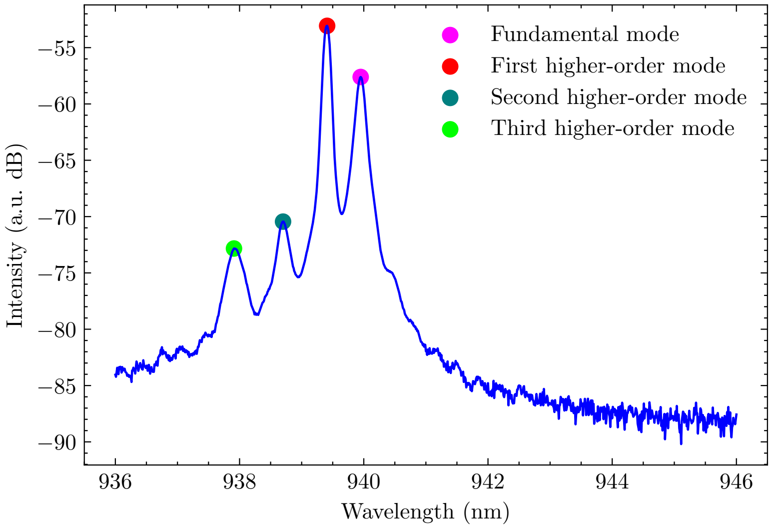

Figure 4.30: Sub-threshold measurements of the spectrum, showing the splitting of the fundamental and first-order mode. The free-space mode are shoulders in the spectrum at higher wavelengths than the fundamental mode.

4.5.5 Measurement of thermal resistance and effect of self-heating

These photonic crystal VCSELs have higher threshold currents than equivalent aperture-sized oxide-confined devices, so at threshold there is therefore more self-heating and higher carrier concentrations. Temperature and carrier-induced changes to the refractive index profile of the device therefore have a significant impact on the profile of the optical modes. The ion aperture is designed to be larger than the photonic crystal defect, so that the heating and carrier concentration are relatively constant over the region containing the optical mode, but the refractive index changes are still expected to have some effects on the mode profile. The wavelength of the optical mode below the threshold shows these effects.

Assuming that the power conversion efficiency of the device is low at currents below the threshold current, the thermal resistance of this device is calculated to be $1.2\,\mathrm{K\,mW^{-1}}$, from the fit of the wavelength shown in Figure 4.31. At the threshold current of 2.4 mA, there is 5.6 mW of electrical input power, corresponding to a temperature increase of 6.7 K. The refractive index change of

AlGaAs with temperature changes as

$$\frac{dn}{dT} \cong 3 \times 10^{-4}/\mathrm{K} \tag{4.1}$$

.

From the temperature increase at threshold, there is a refractive index increase in the cavity of $\Delta n \approx 0.002$. The threshold carrier density of an oxide-confined VCSEL is on the order of $3 \times 10^{18}\,\mathrm{cm}^{-3}$ [54], and for these devices it is assumed that the carrier density is larger but of the same order of magnitude. The refractive index change due to carrier concentration C is given by

$$\frac{dn}{dC} \cong 4 \times 10^{-21}/\mathrm{cm}^3 \tag{4.2}$$

This gives a refractive index shift of $\Delta n \approx -0.01$ for the threshold carrier density. The temperature and carrier effects on the refractive index are within an order of magnitude of each other and have opposite effects on the refractive index. As shown in Figure 4.31, the wavelength of the mode first dips due to index suppression from an increase in the excess carrier density, and then increases due to self-heating when the carrier density saturates. The diameter and vertical profile of the ion implantation has to be considered so that heating and carrier effects do not dominate the effect of the optical mode.

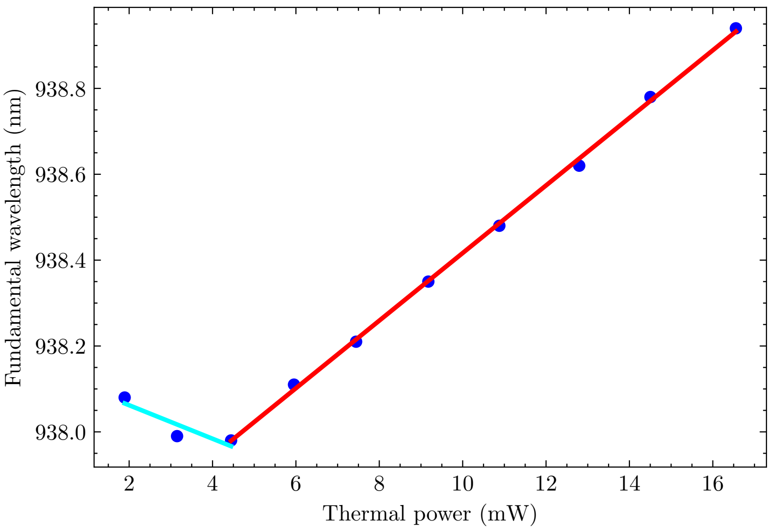

Figure 4.31: The wavelength of the fundamental mode as a function of total input electrical power for a 4.25 µm aperture device. A fit of the thermal resistance was performed using the data in the linearly increasing regime indicated with the red fitted line.

4.5.6 Side-mode suppression ratio

The side-mode suppression ratio (SMSR) of these devices is high compared to oxide-confined VCSELs over a wide range of currents due to the effective suppression of higher-order modes by the photonic crystal. SMSRs of over 40 dB were observed at a wide range of currents from threshold to 5x the threshold (the limit of the measured range, to prevent burning out or changing the properties of devices).

For the purpose of designing a photonic crystal we are interested in finding the largest defect size that supports a single mode. It was found that a 4.25 µm defect supports a single mode over the range of currents examinsed, but that a 4.5 µm aperture is multimode at higher currents in this range. This is smaller than the maximum defect size predicted by simulations of the photonic crystal, which can be understood to be due to the effect of thermal lensing increasing the confinement strength, due to the increase in the refractive index contrast between the cavity and the photonic crystal. However, it is larger than the aperture-size of a single-mode oxide-confined device, which is limited to 3 µm.

Figures 4.33 and 4.33 show the evolution of the optical spectra of 4.25 and

4.5 µm aperture devices respectively. At the highest currents investigated, it can be seen that the first higher-order mode of the 4.5 µm device is much more prominent than the equivalent mode in the 4.25 µm device. The SMSR changes as a function of injection current, due to the effects of carrier and temperature-induced refractive index changes, as shown in Figure 4.34 for aperture sizes between 3 and 4.5 µm.

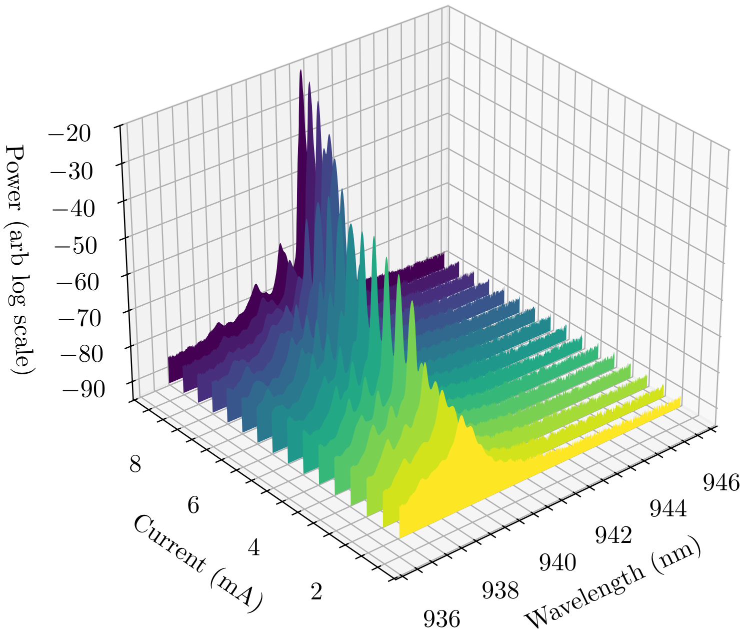

Figure 4.32: The optical spectrum of a 4.25 µm emitter at a range of currents.

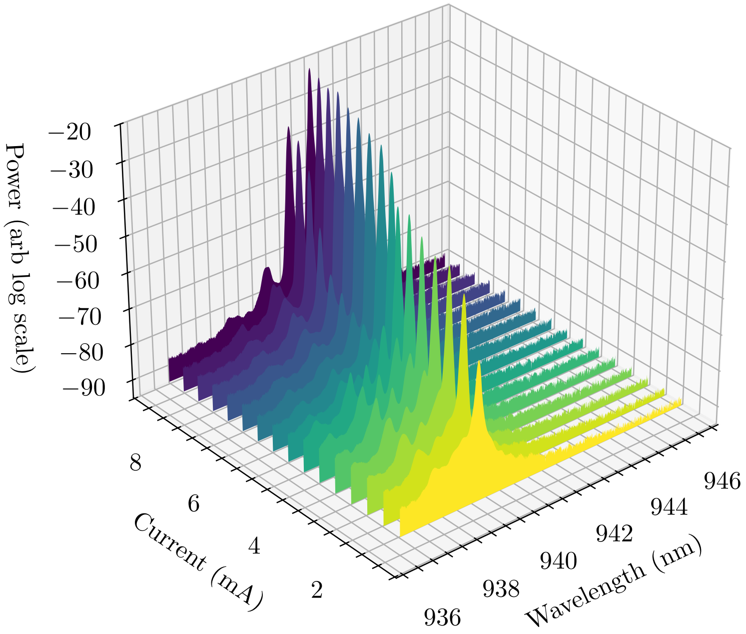

Figure 4.33: The optical spectrum of a 4.5 µm emitter at a range of currents.

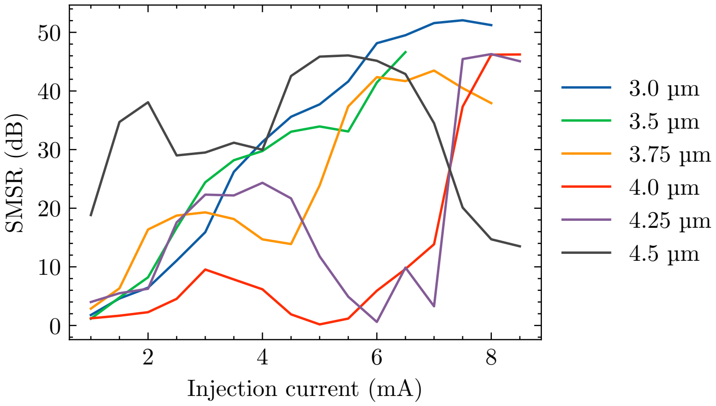

Figure 4.34: The SMSR as a function of injection current for a range of aperture sizes. The largest device has an SMSR that drops at higher currents, the other emitter sizes maintain their SMSR over the range of the measurement.

4.6 Conclusions

A number of routes to achieve higher single-mode or single-wavelength power than conventional emitters were investigated. Attempts to evanescently couple closely-spaced emitters together did not result in a stable mode-coupling interaction between their individual modes that provided enhanced single-wavelength power. An experiment similar to that on coupled photonic-crystal emitters in [83] was carried out with evanescently coupled emitters defined with oxide apertures. With two emitters spaced 12 µm apart, interactions between the emitters result in changes in the optical power from the background trend for certain combinations of injection current to each emitter. However, this effect is weak (leading to a change in the power of less than 1% of the total optical power) and was only observed for a small number of emitters. Evanescently coupled emission has been shown with more closely-spaced oxide-defined devices [79], with emitters spaced on the order of 5 µm apart. Diffractive scattering of light from the oxide aperture and angled mesa sidewalls to provide a total internal reflection condition were not sufficient to increase the distance over which useful evanescent coupling between emitters could occur. Larger structures have also been demonstrated, such as large multi-element emitters [127] and arrays using perpendicular facet elements to enhance the horizontal propagation [128]. A general review of methods for lateral coupling of VCSELs is given in [37].

Closely-spaced arrays of emitters can be defined using etched posts. Single-mode apertures were patterned less than 15 µm apart on a single mesa, and nearly-circular oxide apertures with similar properties to conventionally-defined apertures can be fabricated in this way. The optical output is over a range of wavelengths of less than 1 nm, compared to 2 nm for a single-aperture emitter outputting the same optical power from the same total active area. Measurements of the far-field profile show that the emission is on-axis, because the output of the emitters is not coherent there is no interference pattern. Measurements suggest that in devices of this type where the wavelengths align there is no, or only a very weak, evanescent coupling effect. A similar design to these etched post devices is presented in [119], which uses a multi-emitter design to achieve enhanced modulation speeds.

Multiple-emitter device designs have either a single contact where current is shared between all the emitters, or a separate contact for each emitter to allow the control of the distribution of current. Designs with a single power supply are simpler, but it is not possible to individually tune the emitters to bring them in and out of spectral alignment, where a resonance could occur. In cases where there are individual contacts for each emitter, electrical isolation by means of an etch or by ion implantation can be used to reduce the amount of current that passes between the emitters. An arrangement of diodes in parallel is unstable, with the current unevenly distributed between the diodes, which results in emission at a range of wavelength in VCSEL arrays. Material and fabrication variations, most significantly variations in the p-contact and oxide aperture, lead to emission at a range of wavelengths.

Variation between emitters can be determined from the difference in wavelength between adjacent nominally identical devices. From scans of the cavity wavelength across the wafer the expected variation between emitters is $\approx$ 0.001 nm, but a median variation of 0.25 nm is observed. This is attributed to fabrication variations, which present a challenge for fabricating multiple emitters that emit at the same wavelength. The variation in the measured cavity resonance of the material is orders of magnitude smaller than the wavelength of the fabricated emitters, which suggests that it is variations in the p-contact properties (which affect the electrical resistance and so the degree of heating) and the oxide aperture (which affects the profile and wavelength of the optical mode.)

Photonic crystals are a way of introducing loss for higher-order modes to maintain single-mode lasing for larger apertures at higher currents. Single-mode performance is achieved over a wide range of injection currents, but the higher threshold current means that the power conversion efficiency is low. High threshold currents in photonic crystal VCSELs [129] is one of the main challenges to their use in atomic sensors, and this high threshold is due in part to the need for a thermal lensing effect to set up a refractive index contrast that confines the mode more strongly. Using a photonic crystal allows the single-mode aperture size to be increased from 3 to 4.25 µm. Further work is required to establish what set of design parameters could lead to a photonic crystal VCSEL that better meets the application requirements of an atomic sensor, in particular the optical power and power conversion efficiency.

Chapter 5

VCSEL simulation and experimental validation

> I calculate the lasing modes with mathematical precision,
> and find a self-consistent solution to the rate equations.
> I estimate the gain and loss to meet the threshold condition,
> and calculate the output power, and the mode competition.
> The mirrors and the contacts, the quantum wells and dots,
> I understand the physics, and make a lot of plots.
> I labour for many hours, deep in mathematical cognition,
> so respect my license dongle, or find yourself in prison.
> In short, in matters thermal, electrical and optical,
> I am the very model of a modern laser vertical.
>
> \- *after Gilbert and Sullivan*

5.1 Simulation of semiconductor diode lasers

The operation of a semiconductor diode laser can be simulated by accounting for all of the physical mechanisms in such a device. The interacting electrical, thermal and optical behaviours of the laser can be described by a series of coupled equations that are solved numerically. The models these equations describe and the values of the material properties they refer to are necessarily approximations to reality. Numerically obtained solutions to equations are approximate due to the finite mesh size and the presence of boundary conditions, which are determined by the available computational resources. These factors mean that accurately simulating a laser diode is not straightforward.

Numerical simulations of diode lasers have been a subject of research interest since at least the 1980s [130]. Edge-emitting lasers have a rectangular geometry and can be approximately described with a 1D model, but most often a 2D x, y model is used. In contrast, VCSELs have a circular geometry, with the current flow and the profile of the optical modes determined by an oxide aperture and vertical emission of the output beam as shown in Figure 5.1, so an r, z coordinate system is best suited for VCSEL simulation.

Simulations are a valuable tool for understanding optoelectronic devices, where many physical mechanisms are taking place simultaneously. A simulation can be used as a tool for designing VCSELs by making it possible to predict the effects of design changes and reducing the number of iterations that have to be grown and fabricated. Simulations also provide a physical model that allows access to internal variables, explaining observed experimental effects, and improving our understanding of the physics of devices.

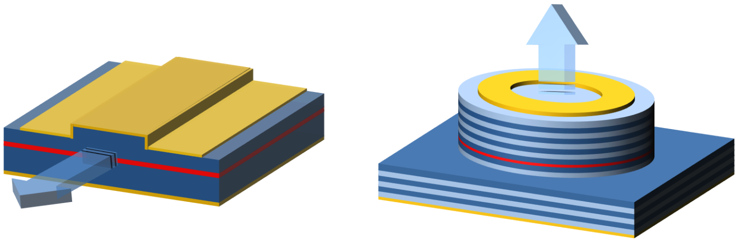

Figure 5.1: A comparison of an edge-emitting laser (left) and a VCSEL (right), from [131]. A 1D approximation can be used to describe the edge-emitting laser, or to simulate the effect of current spreading and heat dissipation an x, y coordinate system can be used. The circular geometry of the VCSEL is best solved in an r, z coordinate system.

In this chapter a process is outlined for setting up a multi-mode VCSEL simulation, and to discuss the validity and limitations of the simulation by comparison of simulated and measured results. We also want to critically discuss the capabilities and limitations of the software to inform its future development and testing. VCSELs used for atomic sensors have particular requirements on the device properties, such as emission wavelength and operating temperature, and simulations can be used to improve the understanding of VCSEL performance at the elevated operating temperature in an atomic sensor.

The software used, Harold VCSEL, performs a coupled electrical-thermal-optical simulation by finding a self-consistent solution to the electromagnetic, transport, and rate equations in a (r, z) coordinate system. Harold or HAROLD (**H**eterostructure **L**a**s**e**r** M**o**de**l** **D**iode) is a commercially available tool developed by Photon Design, and the VCSEL module is a development of a (x, y) solver designed for simulating edge-emitting lasers.

5.1.1 Comparison of simulations and measurements

Comparisons between measured and simulated results must be treated with some care. There are deviations from the nominal design in the fabricated VCSEL (such as the material composition and the dimensions of the oxide aperture), and in the measurement in the boundary thermal and electrical resistances between the sample and the probe equipment.

On-wafer measurements of the electrical (current and voltage) and optical (power and wavelength) properties of a VCSEL can be performed rapidly and in a highly repeatable manner with a semi-automated probestation, as discussed previously in Section 3.10. Using pulsed and continuous-wave (CW) current injection, these measurements can then be used to derive other device properties, such as the electrical series resistance and the thermal resistance.

Secondary ion mass spectrometry (SIMS) is used to find the alloy composition and dopant atom concentration of the measured material. Pulsed measurements can be used as an approximation to isothermal operation, which reduces the complexity of the simulation by removing the effect of temperature changes and allowing the thermal model to be studied in isolation from the electrical and optical models. The optical modes can be compared to near-field and far-field measurements of the mode profile and the optical spectrum.

5.1.2 Limitations of modelling

Due to simplifications and assumptions that must be made when performing the simulation, the results do not exactly match experimental results. We aim to establish which numerical or empirical values have the largest effect on the simulation and the effect that simplifications to the physical model have on the results. Convergence tests are performed on the numerical parameters to show that the simulation is numerically stable.

The limitations in the simulation and comparison of results are due to several factors, among others:

- Uncertainties in the material models for GaAs and $Al_xGa_{1-x}As$. The quantities are functions of doping concentration, wavelength, temperature, alloy composition, strain, and defect density, and the values used by Harold come from models (such as Adachi [52]) that are obtained from fitting a function to experimental data. The measurements are of small quantities of epitaxially grown material of potentially uncertain composition. A number of different models are published in the literature, and here we use the default models supplied by Photon Design which are based on the available literature.

- Empirical factors and approximate models that describe the internal losses of the device. The non-radiative recombination and scattering are described by models that may be semi-empirical or may use parameters extracted from experiments on different structures or at different wavelengths.

- Numerical restrictions, such as the artificial boundary conditions and the use of a finite numerical representation of the fields and distributions in the device, represent quantities that vary continuously over very small length scales. This introduces a tradeoff between simulation accuracy and the computational resources required, and it means that for a simulation to be carried out in a reasonable amount of time (up to a few hours), the size of the boundary and the fineness of the simulation mesh have to be constrained.

- The static cavity modes are calculated for a cold cavity without taking into account the change in the refractive index due to excess carrier density or thermal effects.

- The calculation of a limited number of cavity modes using a non-exhaustive search strategy.

- The use of bulk thermal conductivities to model the heat flow through the mirrors, whereas the literature suggests that the large number of material interfaces in a VCSEL increases the thermal resistance in the Bragg mirrors by as much as an order of magnitude from the bulk values.

The measurements are uncertain due to factors including:

- Variations from the nominal design in the growth and fabrication process of the device, such as the dimensions (from the etch and oxide extent, and crystal-axis dependent oxidation rate), layer thicknesses, material compositions and doping levels, electrical contact quality, and lithographically patterned feature size.

- Differences in the extent and structure of the oxide layers, due to crystal axis dependent etch rates (giving non-circular apertures), tapered oxide layers due to grading in the Al-fraction, and oxidation of other high-aluminium layers in addition to the oxide aperture layer.
- Uncertainties in the electrical and thermal contact with the substrate when performing on-wafer measurements, which can vary significantly due to particulate contamination and backside roughness.
- Uncertainty in the temperature of measured devices, due to the limitations of pulsed measurements and the difference in thermal resistance between simulated and measured devices.

5.1.3 Fitting of parameters

The internal loss mechanisms are outlined in Section 2.3. These mechanisms all have the effect of reducing the external quantum differential efficiency and increasing the threshold current, by causing non-radiative recombination of carrier pairs, or absorbing light into the lattice as heat. In VCSELs the principal losses are due to leakage current over the heterobarriers out of the active region, the free carrier absorption (FCA), and the Auger recombination. The leakage current is described in the simulation by the carrier transport model, which uses a thermionic emission model to calculate the carrier current between materials. Auger and FCA, as well as Shockley–Read–Hall (SRH), are described by material models and parameters from the literature. They can also be estimated by optimising the fit between simulations and LI measurements. In [48], a machine-learning approach is used to estimate and fit the Auger and FCA parameters to match experimental measurements and simulation outputs. In [47] the behaviour of VCSELs at high temperatures is used to find these values. However, in this chapter the default parameters are used, which have been found from experience to work with a range of devices that have been simulated with the software tools in the past.

5.2 Simulation domain and device model

The internal physics of a VCSEL are described by a number of relationships, which relate the internal quantities such as the carrier density, temperature, electric field, current flow, and optical field to each other. Harold finds a self-consistent solution to these equations for a set of operating conditions (injection current and temperature) by solving them numerically on a mesh. The mesh is adaptive, and so the step size is reduced around boundaries and interfaces, and different maximum step sizes can be specified in different parts of the structure. Convergence tests show that the default recommended mesh size settings are reasonable and achieve a balance between simulation time and reaching numerical convergence. A Harold VCSEL model is specified as an epitaxial structure on which operations such as depositions, material replacements, and etches are performed, and in this way it is possible to specify a complete model of a VCSEL with arbitrary device geometry.

In the latest version of Harold VCSEL (7.10) it is possible to have a different optical model mesh from the thermal/electrical meshes. The optical mode is confined to a much smaller area than the heat and current transport, so we can choose simulation regions that suit the characteristic dimensions of the optical mode and of the heat distribution into the substrate. This also allows us to use a thick and wide substrate (675 µm thick with a 2000 µm model radius, sufficiently wide that there is minimal heating on the outer edge). With the adaptive mesh means the radial mesh step increases from 0.1 µm or less in the active region to 10 µm towards the edge of the device. A view of the mesh is shown in Figure 5.2. Step sizes vary between 1 nm in the quantum wells and 50 µm in the substrate, and vary in both the r and z directions. The simulation time goes approximately as N^2 with the number of mesh elements, but some parts of the model such as the Schrödinger equation solver in the quantum wells and the thermionic emission calculation at the heterointerfaces require high resolution. Generally the z step is more important than the r as that is the direction of material variation and carrier flow.

As heat and carriers travel further from the device, the cross-section through which they pass increases quadratically, and so the dominant contributions to the electrical and thermal resistance are from the immediate vicinity of the active region.

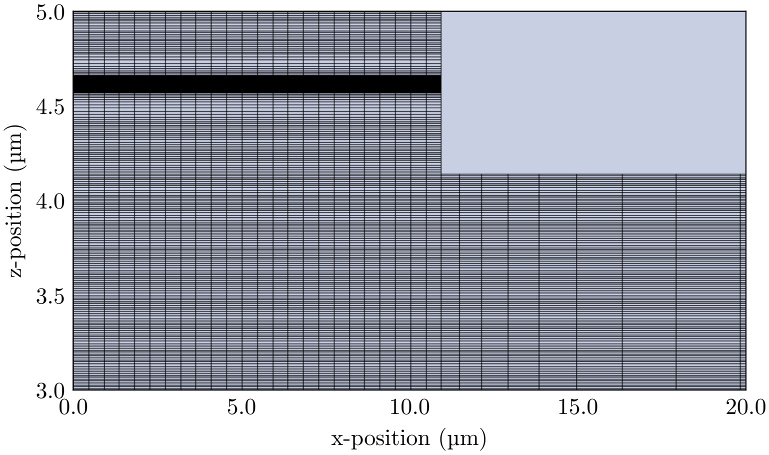

Figure 5.2: A view of the adaptive mesh on which the electrical and thermal models are solved, showing high density around the active region, and reducing density radially away from the active region.

5.3 Devices for investigation

The VCSEL design investigated here is an 852 nm AlGaAs structure, with 20 upper mirror pairs and 32 lower pairs. These are manufactured using the QuickFab process as described in [132]. Devices were fabricated in a range of aperture diameters from 4 to 12 µm, and measurements made at a range of temperatures using the probestation as described in Section 3.10. A view of a measured device is shown in Figure 5.3.

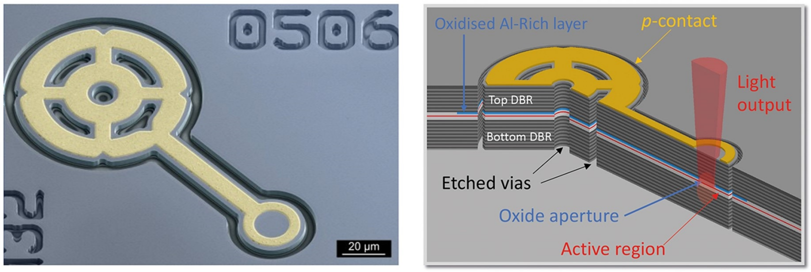

Figure 5.3: View of a measured device showing the layout of the design and the location of the optical output, from [97]. On the left is a SEM micro-graph with colour rendering, and the right a schematic region showing the optical output.

5.4 Electrical transport model and series resistance

The electrical model in Harold simulates the voltage-current characteristics of the device, which depends on the electrical series resistance in the contacts and Bragg mirrors and the recombination of carriers in the diode. In this section we discuss the series resistance and aim to establish the sensitivity of the series resistance to various uncertainties, such as contact dimensions, contact resistance, and doping levels. We want to establish that the carrier transport model in Harold works to model the flow of carriers through a large number of mirror layers with hetero-interfaces between them.

The electrical resistance of the p-contact and p-DBR are among the main contributors to the self-heating of the device and the overall power conversion efficiency. The electrical resistance of the p-DBR also affects how the current is injected into the aperture, particularly for larger apertures. Figure 5.4 shows the way the current is directed through the aperture. The arrows show the direction of current flow, which travels radially inwards and through the oxide aperture before spreading again in the substrate. Current-crowding is an effect where current is selectively injected into the edge of the aperture, selectively causing optical modes concentrated in the outside of the aperture to lase.

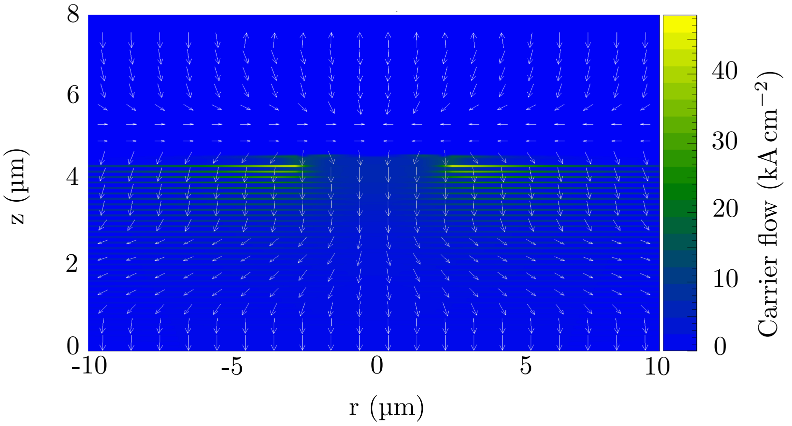

Figure 5.4: The simulation of the flow of carriers through the device.

A drift-diffusion model is used to calculate the current flow due to an electric field in the bulk, and a thermionic emission model (described further in [133]) is used to model current flow across heterointerfaces. The resistivity of a semiconductor decreases slightly at higher temperatures, but for the temperature changes that occur during pulsed measurements this effect is minimal. Comparing isothermal simulations with pulsed measurements means that temperature effects do not have to be considered.

The bulk electrical conductivity of a semiconductor can be approximated, assuming full ionisation of dopants, by

$$\sigma = q(n\mu_n + p\mu_p) \tag{5.1}$$

where σ is the electrical conductivity, q is the elementary charge, n and p are the electron and hole concentration and μ_n and μ_p the electron and hole mobilities respectively. Electrons typically have higher mobilities than holes (in AlGaAs by over an order of magnitude [134],) making the p-DBR more resistive than the n-DBR.

5.4.1 Measurement and simulation of series resistance

Pulsed Current Voltage (IV) measurements were performed using a Keithley 2520 Pulsed Laser Diode Test System, with optical power measurements also taken for comparison of the thermal rollover with CW measurements. A pulse length is chosen so that the voltage has fully risen, the required length depending on the capacitance of the device. As discussed in Section 3.11 although pulsed measurements are nominally isothermal, in VCSELs due to the small active region size heating of up to 10 °C occurs for typical pulse conditions. Figure 5.5 shows the magnitude of the changes in IV characteristics due to an increase in substrate temperature of 25 °C, and the corresponding change in the slope of the IV. This puts an upper bound on the amount of discrepancy between the isothermal simulation and the nominally isothermal pulsed measurement.

The IV characteristics of the VCSEL are the sum of the linear series resistance and the non-linear properties of the diode, so that

$$V_{\text{VCSEL}} = V_{\text{diode}} + IR_{\text{series}} \tag{5.2}$$

The Shockley equation describing the current-voltage relationship of an ideal diode is given by

$$I_d = I_s \left(\exp \frac{V_d}{nV_T} - 1 \right) \tag{5.3}$$

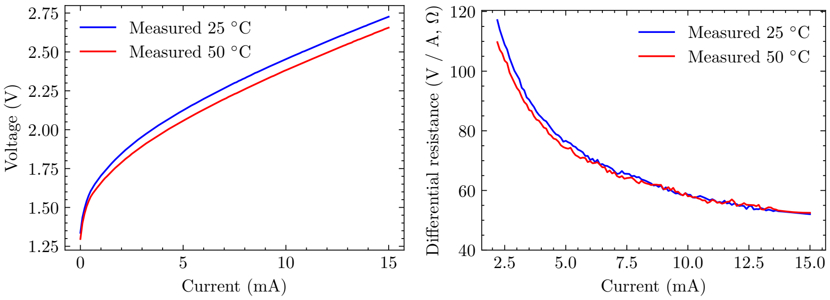

Figure 5.5: Measured pulsed IV relationships at substrate temperatures of 25 and 50 °C, and the derivative of the smoothed IV.

where I_d is the diode current, I_s is the reverse bias saturation current (or scale current), V_d is the voltage across the diode, V_t is the thermal voltage and n is the ideality factor, also known as the quality factor or emission coefficient. A simple model for the IV of a VCSEL is the sum of the diode resistance and the series resistance. The asymptote of dV/dI should represent the series resistance, as the differential resistance of the diode tends to 0, but this model does not fit the measured data well even with a freely varying ideality parameter in the fitting model. An indicative value for the series resistance to allow the comparison of different IVs can be found from the asymptote of the differential resistance, as shown in Figure 5.5.

5.4.2 Substrate and feed electrical conductivity

The IV characteristics are measured using a 4-wire measurement, which removes the resistance of the electrical leads and the contact resistance between the probes and the feed pad, so the measured voltage is between where the probes make contact and the metal chuck the wafer sits on.

To compare the simulated and experimental electrical resistances, we need the electrical resistance that is outside the simulation domain. The feed between where the probe makes contact is 300 nm thick 8 µm wide, and the relevant length is 100 µm between the probe contact point and the device. With the resistance of the feed line given by

$$R = \frac{\rho L}{A} \tag{5.4}$$

for length L and cross-section A, and a resistivity ρ of $2.44 \times 10^{-8}\,\Omega\,\text{m}$, this gives a feed resistance of ≈1 Ω. The gold feed is around 5000 times more conductive than the p-doped GaAs cap layer underneath it, and so it can be assumed that the current travels almost exclusively through the feed. Underneath the feed the material is fully oxidised and so there are no current paths except through the active region of the VCSEL.

The electrical resistivity ρ for n-doped GaAs is around $1 \times 10^{-6}\,\Omega\,\mathrm{m}$ for the $3 \times 10^{18}\,\mathrm{cm}^{-3}$ doped substrate used here. The n-contact electrical resistivity makes a negligible contribution to the electrical resistance of the device due to its much larger area than the p-contact. There is also a contact resistance between the chuck and the metal contact, with a resistivity that depends on the surface roughness of both surfaces and the applied pressure, but typical values are also much less than 1 Ω for the size of the contact and the contact pressure due to the backside vacuum [135].

In summary, from the substrate and feed that are inside the circuit of the 4-wire voltage measurement but outside the simulation domain, we can account for an additional resistance of less than 2 Ω, which is much less than typical device series resistances of 50-100 Ω.

5.4.3 Distribution of applied voltage through the device

At 0 V applied bias, there is an in-built potential in the device due to electron and hole diffusion across the diode. There is a further change in the potential at the ohmic contacts with the metal, but at 0 V bias in equilibrium the potential of the contacts is the same. When current is flowing through the VCSEL, the applied voltage through the device can be found by subtracting this zero-bias inbuilt potential from the potential at a given bias. Figure 5.6 shows the distribution of the applied electric field through the device as a function of bias current. This is found from the potential in the model at a height z corresponding to the top of that particular section.

When in operation, around three-quarters of the applied voltage in the VCSEL model is across the diode. The majority of the remaining applied bias is in the p-DBR, with smaller contributions from other parts of the device. This indicates that to accurately find the series resistance of the device, it is the electrical model for the p-DBR that is most relevant. Due to the large number of heterointerfaces between different mirror layers, simulating the resistance of this part of the structure is not straightforward.

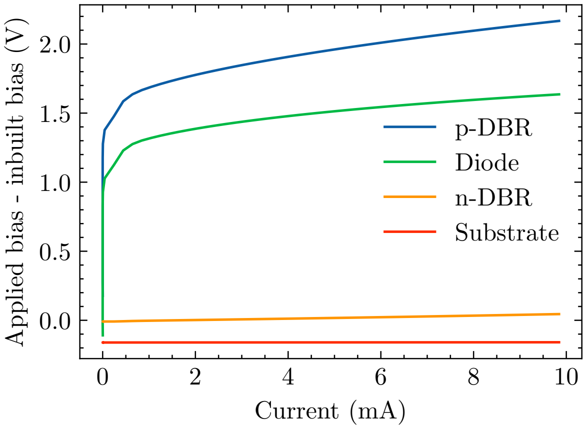

Figure 5.6: The distribution of the applied bias in different parts of the device, from a simulation output. Due to the way the bias is applied in the simulation, this does not consider the contact resistances. The interface between the metal contact and the substrate results in an inbuilt bias.

5.4.4 Measurement of device composition and effect on resistance

Most of the series resistance of the device is due to the mirrors, and in particular the p-mirror because of the lower mobility of holes in comparison to electrons. The bulk resistance of the semiconductor and the barrier due to the bandgap change at material interfaces are functions of the doping concentration and alloy composition. The actual material composition can be different from that specified in the design, and Secondary Ion Mass Spectrometry (SIMS) can be used to establish the actual level of dopant atoms and material composition.

SIMS uses an ion beam to sputter the material off the sample, and then the secondary ions are measured by mass spectroscopy. The SIMS measurement is performed by Loughborough Surface Analysis. An area of 33 µm square was ablated using Cs^+ ions, with a beam current of 10 nA and an energy of 10 keV. A CAMECA IMS 4f was used to measure the alloy composition (Al and As) and a CAMECA IMS 7f auto to measure dopant concentrations.

The instrument measures the rate at which different species are removed from the sample, and the data are reported in terms of counts per second for each species. The As count can be used as a baseline as the concentration of this species stays the same, in order to re-base the time-series data in terms of depth. The data is recorded with a time resolution of 8 s, which corresponds to a vertical resolution of 9 nm, and so the resolution is limited compared to the variation of the composition in the mirrors, the grading layers of which are 20 nm thick.

The difference between the specified and the actual doping concentration through the stack is shown in Figure 5.7. The doping is highest at the surface of the sample, but the measurement of the concentration here is not completely certain. However, this indicates that the doping could be significantly different. Figure 5.8 shows the doping concentration close to the surface, showing that the carbon concentration is much higher than the nominal value at the top, to improve the contact resistance. A small amount of silicon is also seen at the surface, possibly from organic contamination.

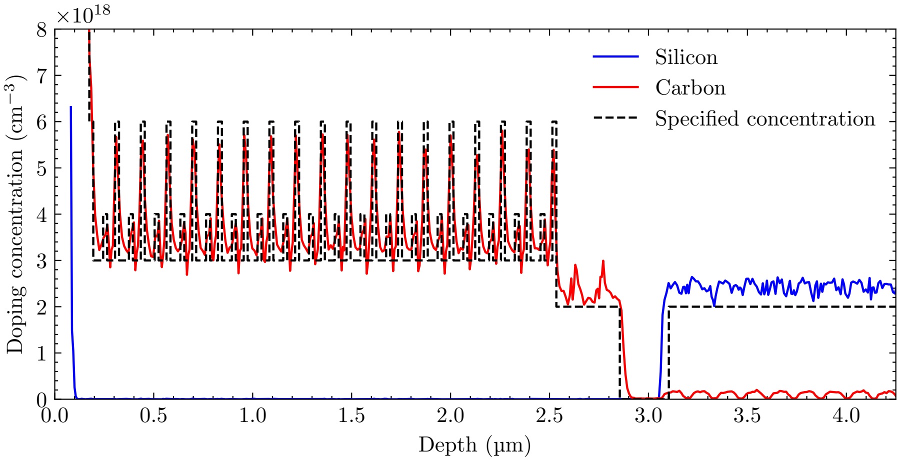

Figure 5.7: The concentration of the p-dopant carbon and n-dopant silicon compared to the specified doping concentration. Shown is the top mirror, and the nominally undoped (intrinsic) region containing the p-n junction, followed by the bottom p-mirror.

The error in the measurement of the doping is difficult to quantify as the error in the SIMS process is not known. From this data, we can find the total quantity of dopants in a section of the sample by integrating the data over the range shown in Figure 5.9, from a depth of 0.5 µm to 2 µm inside the p-mirror. The total amount of dopants in the structure is found to vary by 4% between the nominal design and the the measured concentration. Larger discrepancies are seen in other parts of the structure, such as in the region close to the junction.

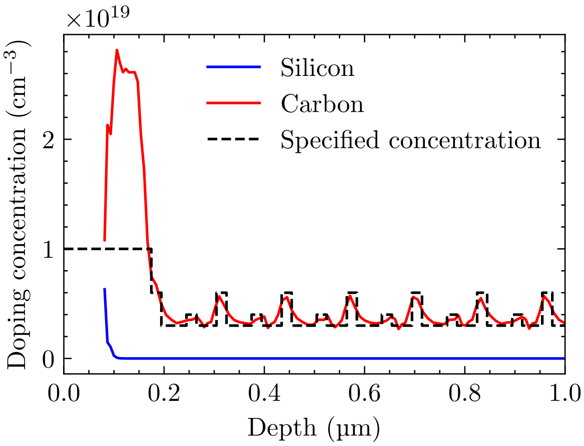

Figure 5.8: Measurements show a significant spike in dopants at the surface. This could be due to organic contaminants outgassing from the sample, or higher doping at the top layer (the design is specified as $>1 \times 10^{19}\,\mathrm{cm}^{-3}$ doping concentration in the cap layer.)

This suggests that except at the very top layer, the doping in the simulated structure can be taken to be the same as the design.

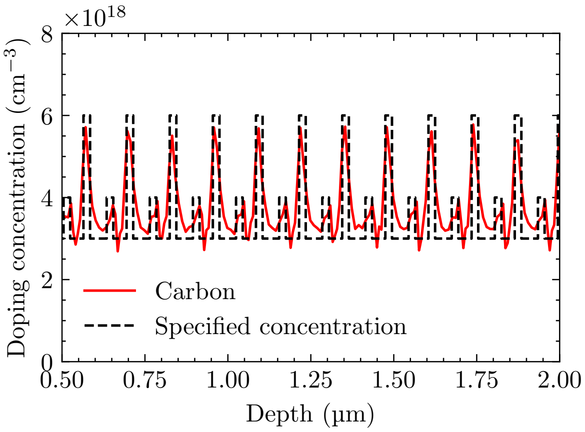

Figure 5.9: The doping in the p-mirror for the designed specification and the SIMS measurement.

5.4.5 Effect of variation of doping on series resistance

Increasing and decreasing the doping concentration by a factor of 1.25 in the model captures a wide possible range of doping concentrations, in particular at the material interfaces. The SIMS measurement does not have a high resolution compared to the steps in the doping concentration shown in Figure 5.9. As shown in Figure 5.10, an increase or decrease in the series resistance of $5\,\Omega$ is obtained from a 20% change in the doping concentration. Effects such as dopant diffusion, incomplete ionisation, and the amphoteric doping of Si in GaAs [136], mean that the doping concentration in the model could be different to the concentration of dopant atoms. The sensitivity to changes in the doping in the p-DBR is much higher than in the n-DBR due to the much higher mobility of electrons than holes in AlGaAs.

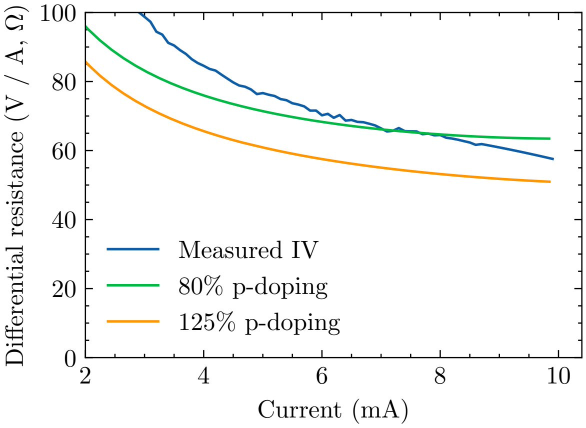

Figure 5.10: Changes in the VI due to variation in the doping concentration in the p-DBR, compared to a measured device.

5.4.6 Variation of contact resistance

The p-contact resistivity and dimensions also contribute significantly to the ohmic resistance of the device. The contacts are Ti-Pt-Au with a standard high-temperature anneal, and circular transfer length method (CTLM) measurements of the p-contact resistance show significant variation across the wafer of up to 50%. Additionally, the actual p-contact dimensions will be different from the nominal dimensions because the p-contact is patterned with a negative-tone photoresist which is intended to have some undercut to allow for good liftoff. A change in the dimensions also results from misalignment of the etch and p-contact lithography steps, with an expected misalignment on the order of 0.5 µm for by-eye optical alignment.

Simulations were carried out that vary the conductivity and the dimensions of the contact to establish the sensitivity to these parameters, and these results are shown in Figure 5.11. Changing the inner radius of the p-contact by 1 µm, or changing the resistivity by 50% changes the device series resistance by 2 Ω and 1.1 Ω respectively.

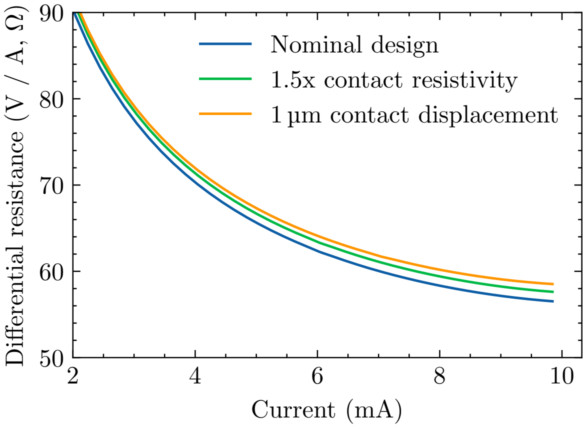

Figure 5.11: The change in dV/dI when the p-contact is changed by increasing the contact resistivity by a factor of 1.5, and increasing the inner diameter of the p-contact ring by 1 µm.

5.5 Cavity mode solver

VCSEL cavity modes are confined laterally by the oxide aperture and mesa etch, and vertically by the Bragg mirrors. VCSELs may be single-mode or multi-mode, depending on the size of the active region, the confinement strength, and the presence of mode selection features such as surface relief etches, grating, or induced disorder (as discussed in Section 2.4). In this section we discuss the optical mode solver in Harold.

The solver finds the 3D profile of the mode inside the device, and from this the far-field emission profile can be calculated. The confinement factor Γ of a laser mode is a measure of the overlap of the mode with the active region. It is usually defined as the fraction of the squared electric field that overlaps with the active region. The quality factor of a mode Q is a measure of the fraction of light that escapes from each round trip. The spontaneous emission coupling factor β is the fraction of spontaneously emitted light that couples into a mode. The top and bottom mirror reflectivities R_t and R_b are due to the number of layers, refractive index contrast, and optical absorption in the DBRs.

5.5.1 Harold mode solver

The VCSEL is represented as an optical fibre with sections of different lengths that have piecewise constant refractive index n. The fibre modes in each of these sections are found with the finite-difference method (FDM) fibre solver. The coupling between the fibre modes in adjacent sections is due to the overlap between modes in each of the sections.

In a circular fibre, the modes are described m, p quantum numbers, where p is the polarisation quantum number and the azimuthal quantum number m describes the cylindrical variation of the mode. $m = 0$ are the transverse TE modes, and $m > 0$ are the hybrid HE modes, with $m = 1$ the fastest-propagating fundamental mode using the convention in [137]. A VCSEL can contain both Transverse Electric (TE) and hybrid (HE) modes.

The cavity mode solver in Harold searches for cavity modes by splitting the cavity in two at an arbitrary location, finding the reflectivity matrices of the two sections, and using these to compute the round-trip reflection matrix of the whole structure. The eigenvectors of this matrix correspond to the coefficients of the amplitudes of the transverse modes used to represent the eigenmode. The mode wavelength is varied to achieve a round-trip phase relationship of $2n\pi$, and the gain required to achieve a round-trip gain of unity is found in order to give an indication of the threshold gain for that mode. This is similar to methods reported in the literature [138].

The mode solver can solve for different mode orders by investigating different bases of fibre modes m, p. This gives better modelling of the threshold and rollover, especially for large-aperture devices where more of the optical gain might be at the edge of the aperture due to current crowding. Different mode orders are shown in 5.12, showing how the higher-order mode fills a different part of the active region. The optical solver searches for a specified number of target cavity modes which are selected from a larger number of candidate modes by having the lowest lasing threshold for a simple step-function gain profile. The modes are calculated for a cold-cavity structure, and no accounting is made for the effects of carriers or self-heating on the refractive index. At high injection currents close to the thermal rollover, self-heating results in an increase in the number of confined modes in real devices.

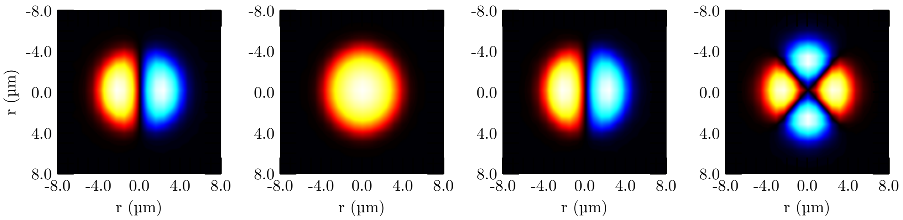

Figure 5.12: The E_x of the electric field for modes with $m = 0, 1, 2, 3$ from left to right. $m = 0$ is the purely TE mode. Red is positive and blue is negative.

5.5.2 Convergence tests on numerical parameters

Convergence tests can be used to demonstrate that the chosen numerical parameters are numerically stable. The parameters in the cavity mode search are:

- The number of transverse modes `maxtransversemodes` N used as the basis to represent the cavity modes. Bases of larger N require exponentially more time to compute because the size of the scattering matrix scales as N^2. For $N > 150$ the calculation time for a multi-mode simulation exceeds several hours. The required number of modes depends on the size contrast between the largest and smallest features (the mesa and oxide aperture), as higher-order modes can represent features with higher spatial resolution.

- The radius of the optical mode solver and the boundary conditions at the edge of the optical model. Depending on whether the simulation domain is inside or outside the mesa results, there are magnetic wall boundary or electric wall boundary conditions respectively. Convergence tests show that for a sufficiently large basis of N the same cavity modes are found. The solver radius should be chosen so that the electric field of the cavity mode is 0 at the edge of the solver domain, so for a typical optical mode with an exponential decay at the walls of a simulation domain 5x larger than the mode, the intensity of the optical field is less than 1% of that in the centre.

- The maximum refractive index contrast `maxdeltarix` when sections with graded composition are discretised into slices to make a refractive index model of the structure. Finer discretisation increases the size of the reflection matrix that has to be solved.

- The bases of m, p investigated. The bases investigate depend on the computational resources available - with 4 processor cores enabled, bases with $p = 2$ and m between 0 and 3 are calculated, as well as the $m = 0, p = 1$ basis.

- The number of cavity modes `maxcavitymodes` that the solver looks for. A reasonable approximation to the performance can be found using a single cavity mode, but different mode orders are concentrated on different parts of the structure. Many candidate modes (potentially several in each basis) are found and the ones with the lowest estimated threshold are used.

- The wavelength range of the search. Modes are typically spaced over a range of several nanometres. The fundamental modes has the highest group velocity and so the longest wavelength. The search space for physical candidate modes is therefore in a small range of wavelengths slightly shorter than the wavelength of the fundamental mode. Restricting the range of wavelengths reduces the computation time by preventing the solver from investigating non-physical modes.

- The resolution with which basis modes are represented `nres` when calculating the coupling between modes in adjacent sections to compute the scattering matrix.

- The number of refinements, which are additional iterations of the mode solver that improve the convergence accuracy.

- The `gainstepradius`, which is used to select candidate modes. The gain profile above threshold is approximated by a constant gain in the active region and a loss outside of that region.

These numerical parameters can interact in different ways to prevent the cavity mode solver from working as expected. Numerical convergence tests can be misleading as several parameters may not have converged, and the behaviour of the solver is unstable for bad choices of parameter. An incorrect choice of numerical parameters results in spurious modes as shown in Figure 5.14, in comparison to the correctly converged modes shown in Figure 5.12.

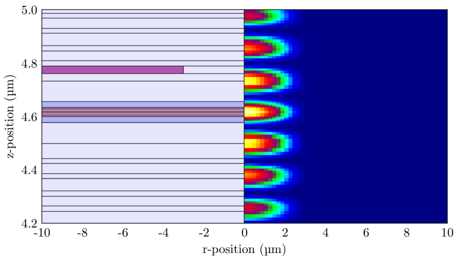

Figure 5.13: A correctly converged optical mode, which is concentrated in the cavity region defined by the oxide aperture. The structure is shown on the left, showing the oxide aperture that partially extends into the structure. The quantum wells below are at an anti-node of the optical mode to maximise the confinement factor, and the oxide aperture at a node to reduce the scattering loss.

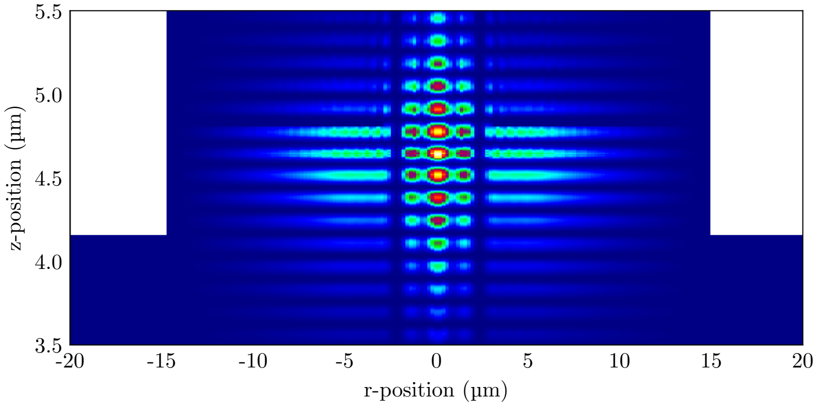

Figure 5.14: A typical spurious mode that arises from incorrect calculation of the coupling of light between different sections of the VCSEL. This happens either when the calculation or normalisation of the basis modes results in too high a numerical error, or the discretisation of the modes is too coarse for accurate calculation of the overlap. This type of mode typically has a mirror reflectivity that is unphysically high (greater than the upper limit for a plane wave), and as a consequence its threshold gain is low and so is selected as a lasing mode. Spurious modes have field components outside of the cavity.

5.5.3 Reflectivity and discretisation of a Bragg mirror

Epitaxially grown DBRs in VCSELs use graded layers to improve the electrical conductivity of the mirrors by removing a sharp change in the bandgap. Modelling the DBR with the Harold mode solver requires the refractive index profile to be discretised, with the discretisation step specified by the parameter `maxdeltarix`. The effect of discretisation of the DBR on its reflectivity as calculated by the optical mode solver and by the TMM is shown in Figures 5.15 and 5.16. The mirror contrast Δn between the mirror pairs of this design is ≈ 0.5. Different discretisation resolutions have a minimal effect on the mirror reflectivity, which means that a coarse discretisation can be used.

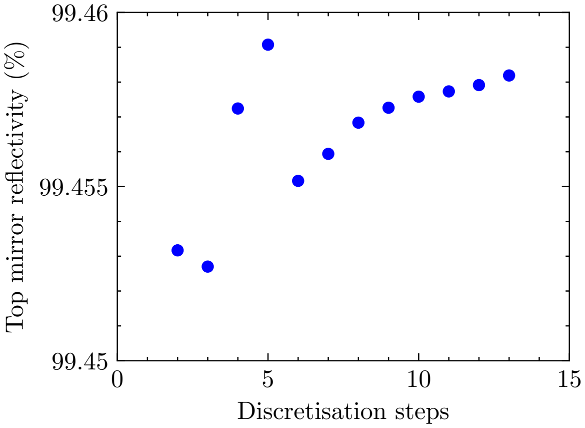

Figure 5.15: Change in the reflectivity of the top mirror as found by the optical solver for different numbers of discretisation steps.

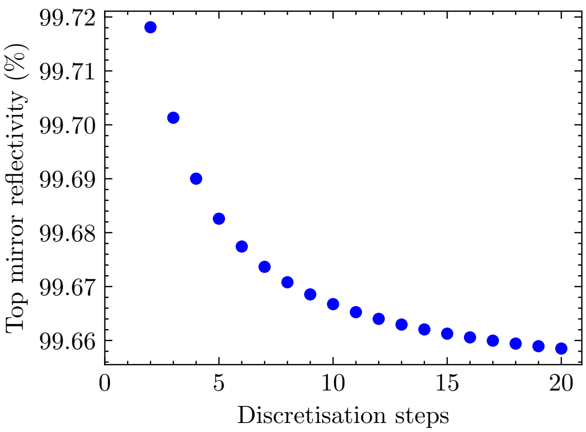

Figure 5.16: The change in the reflectivity of the top mirror from a plane wave calculated with the TMM for different levels of discretisation.

5.5.4 Number of transverse modes and resolution of representation

An arbitrary optical field in the structure can be represented in terms of a superposition of the fibre modes in each section. In terms of the forward (+) and backward (-) travelling propagating eigenmodes of each layer, the field is given by

$$\mathbf{E}(\mathbf{r}, z) = \sum_k \left\{ A_k^+ \mathbf{E}_k(\mathbf{r}) \exp(-\mathrm{j}\beta_k z) + A_k^- \mathbf{E}_k(\mathbf{r}) \exp(\mathrm{j}\beta_k z) \right\} \tag{5.5}$$

where β_k is the propagation constant (the effective index) of the mode [138]. A complete representation is over all values of k, but the vector of eigenmode coefficients A is truncated for the purpose of the calculation.

The coefficients of the optical mode in terms of the fibre modes can be considered as the spatial frequency components in r. A convergence test on the number of transverse modes N shows that at least 100 modes are needed to correctly find the higher-order cavity modes, with an oxide radius of 3 µm and a solver radius of 15 µm. Smaller values of N can result in non-physical modes being found because the scattering between sections is not properly calculated, which results in spurious reflections.

Figure 5.17 shows the coefficients of the fundamental mode in a section of the mesa close to the aperture, using $N = 60$ and $N = 120$, showing how a

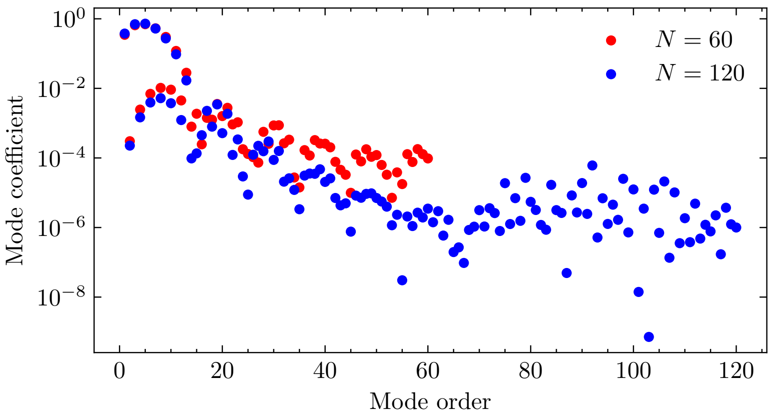

Figure 5.17: Components of the same fundamental $m = 1, p = 1$ mode, on a log plot. The same mode is represented differently when a different number of transverse modes N are available to the solver.

larger value of N results in different coefficients. The intensity of the cavity mode is mostly in the smallest order components ($N < 10$) but higher order components ($N > 100$) contribute to the profile. A larger basis represents the mode more accurately but uses considerably more computational resources, as the size of the scattering matrix grows as N^2. The main motivation for using a larger basis is to prevent the solver from incorrectly converging on spurious non-physical modes.

Running additional refining routines on the values of the coefficients does not result in a significant change in the values as shown in Figure 5.18, which means that the numerical routine is converging well and that challenges in finding the optical modes are due to limitations on the size of the basis.

Figure 5.19 shows how a fundamental and a higher-order mode have a different relationship between the order of the basis modes and the coefficient. Numerical convergence tests are required for different aperture and optical solver sizes.

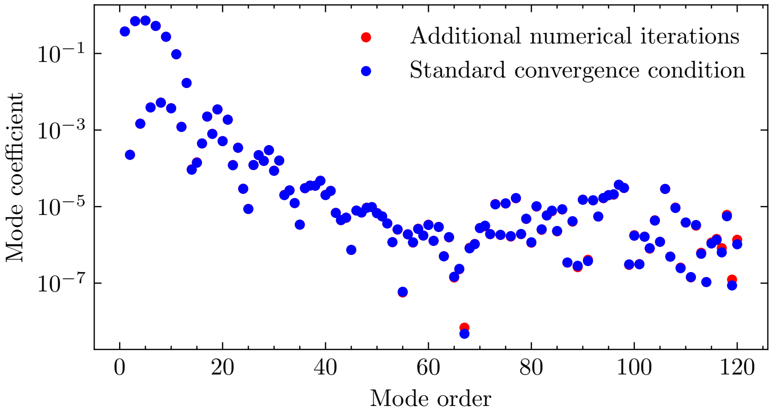

Figure 5.18: Using additional numerical iterations to resolve the coefficients of the mode more accurately. There is no significant change with additional numerical iterations, which means that the numerical convergence of the mode solver is good.

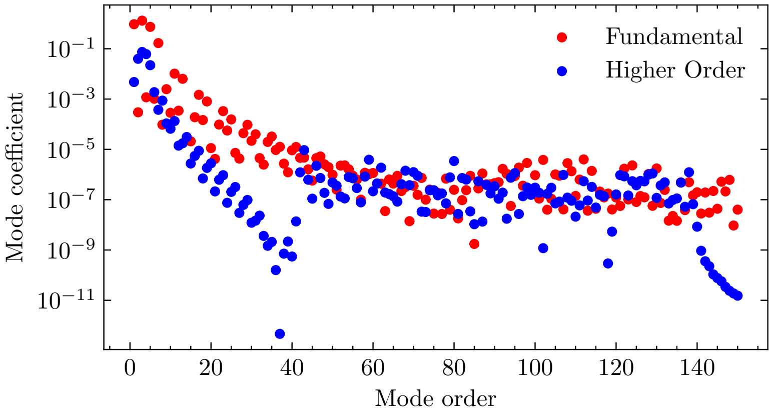

Figure 5.19: The fundamental and higher-order modes are represented in different bases.

5.5.5 Spontaneous emission coupling factor

When carriers recombine by spontaneous emission in the active region, the photons produced can be coupled to a lasing mode and the spontaneous emission coupling factor β represents the fraction of spontaneous emission that does so. In a simulated device β determines how much light is emitted from the top facet below the threshold and the sharpness of the turn-on, and a higher β results in a softer turn-on and a slightly lower threshold current. The value of β can be estimated from the ratio in slope efficiency below and above the threshold, as described in [51]. The ratio of the intercepts on a vertical line at the threshold of the L–I extrapolations on a log-log plot is approximately equal to β. However, this method requires measuring the modal light only, and measurements of the LIV performed with an integrating sphere also contain a large amount of scattered spontaneously emitted light. A spectrally-resolved LIV as shown in ref 5.20 finds a smaller amount of light below threshold, and so a higher value of β. However, this is still an overestimate of the value of β as it does not represent a measurement of the modal light only.

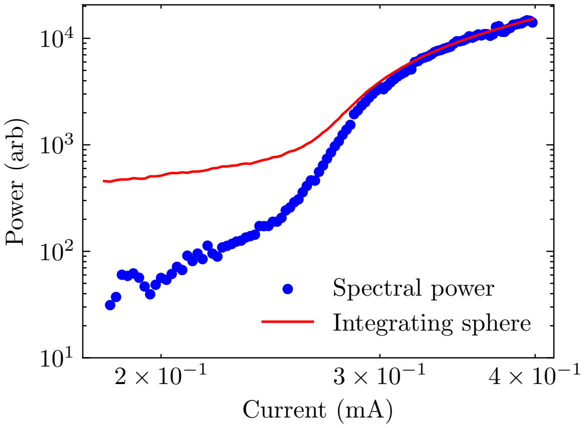

Figure 5.20: A spectrally-resolved measurement of power as an approximation to the modal power. The spectral resolution is 0.1 nm, which is much larger than the width of the mode. This measurement could be done using a scanning optical spectrum analyser to better constrain β but would still be an overestimate.

β can also be obtained from the density of optical modes per unit volume per unit frequency by integrating over the cavity volume and the bandwidth of the spontaneous emission to find the number of optical modes that must contain the total spontaneous emission. It can also be found by considering from the rate equations for a laser the emission rate into one mode and the total emission rate. These methods, both presented in [68], and using the values the confinement and cavity dimensions in VCSELs give a β of 2×10^{-4}, and so this is the value used for simulations. β has a small effect on the threshold current and no effect above the lasing turn-on so its exact value is not critical.

5.5.6 Simulating a VCSEL using multiple optical modes

Multi-mode VCSELs can have higher quantum differential efficiency than single-mode ones, as modes of different orders fill different parts of the cavity, and higher-order modes have maxima closer to the edge of the aperture. Figure 5.22 shows the measured higher differential efficiency of larger aperture apertures. Multi-mode VCSEL simulations are discussed further in the next chapter in the context of high-temperature simulations, where higher-order modes dominate the lasing.

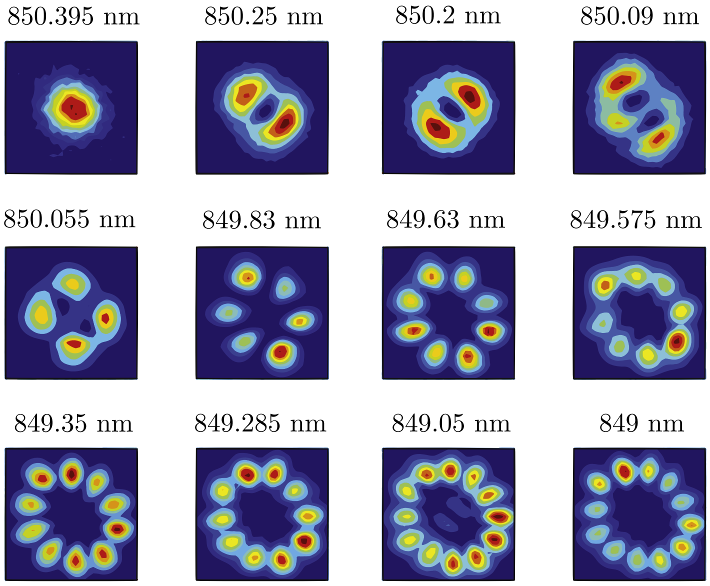

850.395 nm
850.25 nm
850.2 nm
850.09 nm
850.055 nm
849.83 nm
849.63 nm
849.575 nm
849.35 nm
849.285 nm
849.05 nm
849 nm

Figure 5.21: A spectrally-resolved near-field measurement from [139] shows the different modes that lase, and how they have intensity maxima in different parts of the cavity region.

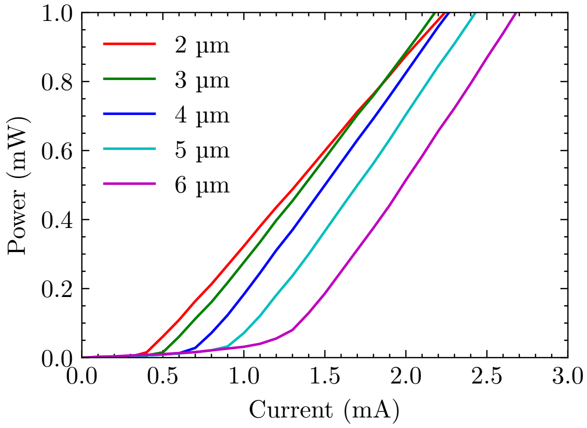

Figure 5.22: Pulsed measurements of different aperture radius emitters shows a higher external differential quantum efficiency for larger apertures. The 2 µm radius emitter is predominantly single-mode, and has a lower differential efficiency than the larger-aperture multimode devices.

5.6 Simulation of thermal resistance

The maximum optical output power of a VCSEL is limited by the thermal rollover, which results in a rapid drop-off of optical power at high internal temperatures. The properties of devices can be investigated using a pulsed current supply to approximate isothermal operation, but generally, VCSELs are tested and operated with a CW power supply.

The decrease in optical power at high temperatures is due to a relative detuning of the cavity wavelength and the peak of the gain spectrum, and an increase in Auger recombination, free carrier absorption, and leakage current. These mechanisms are discussed further in Section 2.3. The majority of heat generation is concentrated in the active region, which becomes much hotter than the rest of the device. The increase in temperature as a function of the injection current is due to the power conversion efficiency and the thermal resistance of the device. In this section, the measurement and simulation of thermal resistance are discussed, then the effect of a temperature increase on the operation of the device is discussed in the next chapter.

The thermal resistance of the semiconductor material is a bulk material property, but in a VCSEL there is additional thermal resistance due to phonon scattering at material interfaces in the DBRs [140]. There are also thermal resistances associated with the contact between the backside of the wafer and the heatsink. The simulation uses bulk thermal resistances and does not account for phonon scattering at interfaces, and so underestimates the thermal resistance of the VCSEL. The thermal resistance of the simulation model can be adjusted as necessary to match the experimentally measured resistance by changing the boundary thermal resistances.

The heat generation in the mirrors is also due to the material interfaces, which introduce heterobarriers between the mirror layers that increase the electrical resistance, and increased carrier concentration that causes free carrier absorption, which leads to light being absorbed as heat into the lattice. The p-DBR in particular is responsible for a significant amount of the total heating of the device [141], and higher output powers require optimisation of the mirror structure and doping through features such as modulation doping [142]. A simulation can be used to manage the tradeoff between the heat generation, the thermal resistance, and the optical properties of the mirrors.

5.6.1 Temperature distribution

In a steady-state condition, the flow of heat in the device is described by Poisson's equation, which relates the temperature gradient to the thermal conductivity. A simple model for a VCSEL can be created to visualise the heat flow and reason about the dimensions of the thermal domain for the purpose of solving a multiphysics model.

$$\nabla^2 T(\mathbf{x}) = -\sigma(\mathbf{x})/k. \tag{5.6}$$

where $\sigma(\mathbf{x})$ is a source term and k is the thermal conductivity. This equation can be solved numerically, or a simple model for the temperature distribution in a VCSEL can also be found analytically using the fundamental solution for a point source where the temperature decays as $1/|\mathbf{x}|$. The solutions to Poisson's equation are linear, and so by using an arrangement of source and mirror heat sources, the insulating top of the sample and the conducting substrate can be represented in a cylindrically symmetrical 3D model. An infinite line of alternating image sources and sinks defines the necessary boundary conditions for the VCSEL model, which are an insulating top surface and a conducting bottom surface. The heat flow $q(\mathbf{x})$ is related to the temperature distribution by

$$q(\mathbf{x}) = -k\nabla T(\mathbf{x}) \tag{5.7}$$

This vector field can be visualised as lines of heat flux, showing the direction of thermal transport. In Figure 5.23 it is shown how the heat spreads with a thick substrate. Heat spreads infinitely through the substrate, with the heat flux per area decaying with distance. By integrating the heat flux radially, the necessary size of the thermal domain to capture a proportion of the heat transport through the bottom of the substrate can be calculated. A thermal domain with a significantly larger radius than the thickness (in the case of these simulations, by a factor of 3) captures almost all the heat transport. Similar arguments can be made to determine the radius of the electrical domain.

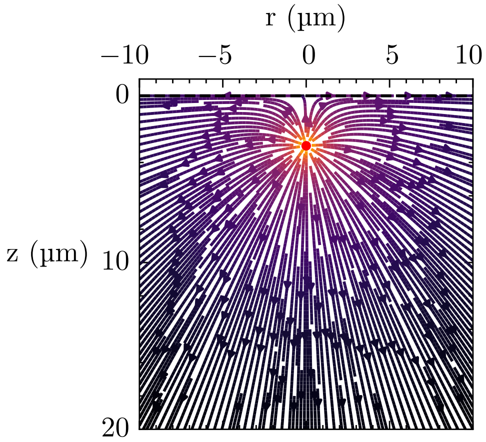

Figure 5.23: An analytical model for the thermal transport showing the heat flux direction away from the active region, indicated in red at a depth of 3 µm. The size of the active region is up to ≈ 10 µm, whereas the substrate is hundreds of microns thick, so a point heat source is a reasonable approximation to the VCSEL. By integrating the flux through the bottom of the model, the impact of the simulation domain radius on the thermal simulation can be determined.

5.6.2 Thermal resistance of AlGaAs and VCSEL DBRs

Heat capacity and conduction in a semiconductor are due to both the lattice (via phonons) and electrons. The VCSEL stack is made from $\mathrm{Al}_x\mathrm{Ga}_{1-x}\mathrm{As}$, and the thermal conductivity varies by more than an order of magnitude depending on the aluminium fraction x. A simple relationship for the thermal conductivity k is from [52], and is given by

$$k = 550 - 212x + 248x^2 \tag{5.8}$$

where k has units of $\mathrm{W\,m^{-1}\,{}^\circ C^{-1}}$.

Thermal conductivity in thin layers of material is reduced by the scattering of phonons at material boundaries. This happens due to mismatches in the lattice constant, and scattering from material defects which occur at material interfaces. This boundary resistance is called the Kapitza resistance. Time-resolved thermal imaging of VCSELs in [140] suggests that this effect could result in a reduction in the thermal conductivity in the z direction towards the substrate by as much as an order of magnitude. Calculating phonon scattering can be done ab initio to calculate the bulk thermal conductivities of materials [143], and methods have been proposed to simulate the Kapitza resistance [144].

5.6.3 Boundary thermal resistance

The thermal contact resistance between the chuck and the back side of the wafer is due to the incomplete contact between the materials, and depends on the microscopic roughness of the interface and the vacuum pressure. The thermal contact can also vary on a very local scale, for example due to particulate contamination. The measurements carried out on the probestation use vacuum pressure to secure the wafer to the chuck. Measurements of this thermal resistance for a gold-metal contact suggest that the range of values is in the range of $0.1\,{}^\circ\mathrm{C\,W^{-1}\,cm^2}$ to $1\,{}^\circ\mathrm{C\,W^{-1}\,cm^2}$ [145].

The effect of heat spreading and contact resistance can be modelled using results from [146]. Higher thermal contact resistance results in increased heat spreading. The VCSEL can be approximated as a point heat source on top of a disc of radius R_0 and thickness d with thermal conductivity k, in contact with a reservoir of heat with a thermal contact resistance h at the interface. The radial temperature distribution in the disc is given by equation 5.9 for a point source.

$$T(r) = \frac{Q}{2\pi k d}\left[K_0\left(\sqrt{B_i}\frac{r}{R_0}\right) - \frac{K_0(\sqrt{B_i})}{I_0(\sqrt{B_i})} I_0\left(\sqrt{B_i}\frac{r}{R_0}\right)\right] \tag{5.9}$$

where B_i is the Biot number

$$B_i = \frac{hR_0^2}{kd} \tag{5.10}$$

where I_0 and K_0 are modified Bessel functions of the first and second kind, respectively. Varying the thermal contact resistance within the range of values that [145] suggests are possible indicates that the effect of thermal contact resistance increases the overall thermal resistance by less than 10%.

Heat can also escape from the top of the sample by radiation and convection. Radiative heat transfer is described by black-body radiation. The power P per unit area is given by

$$P = \sigma \Delta T^4, \tag{5.11}$$

where the Stefan-Boltzmann constant σ is $5.7 \times 10^{-8}\,\mathrm{W\,m^{-2}\,K^4}$. A $1000\,\mathrm{\mu m^2}$ area (approximately the size of a typical VCSEL mesa) with a 10 K temperature difference from ambient conditions dissipates less than 1×10^{-12} W through radiation. The temperature difference needs to be at least an order of magnitude higher for radiative heat loss to become relevant. The convective cooling coefficient h_c of dry air at ambient temperatures is approximately $10\,\mathrm{W\,K^{-1}\,m^{-2}}$ [147], around 0.1% the conductivity of the wafer-chuck interface. Based on the same assumption about the device size and temperature, around 10×10^{-7} W might be dissipated by air convection. Radiation and convection therefore do not contribute significantly to the heat dissipation.

5.6.4 Simulated heat flow

The heat flow and temperature profile can be visualised using a simulation. Figure 5.24 shows the simulated heating in the device, showing how most of the temperature increase is in the active region of the device, and the temperature dropping quickly to the ambient temperature outside of this region. As the model does not account for the increased thermal resistance between layers, it overestimates the thermal conductivity, particularly in the vertical direction.

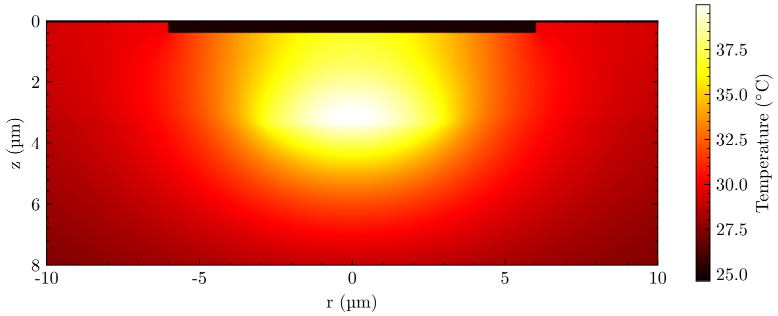

Figure 5.24: The simulated temperature profile in the device. The hottest region of the device is the active region in the centre, where most of the heat is generated. Outside of the active region, the temperature quickly approaches the background temperature. As the optical mode is mostly concentrated in the active region, the wavelength shift can be used as a good measure of this temperature.

5.6.5 Measurements of thermal resistance

The thermal resistance of a VCSEL is the ratio of the thermal power to the increase in temperature in the device. The temperature can be taken as the temperature of the cavity, which is the hottest part of the device, and has a temperature that can be measured directly from the shift in the cavity resonance. The thermal resistance R_{therm} is given by

$$R_{\text{therm}} = \Delta T_{\text{cavity}} / P_{\text{therm}} \tag{5.12}$$

where the thermal power P_{therm} is the electrical input power minus the optical power.

$$P_{\text{therm}} = IV_{\text{external}} - P_{\text{optical}} \tag{5.13}$$

The thermal resistance of a device can be is measured from a wavelength shift at different injection currents using the established temperature-wavelength coefficient of $0.068\,\text{nm}\,\text{K}^{-1}$. Measurements for a device with a 6 µm aperture are shown in Figure 5.25.

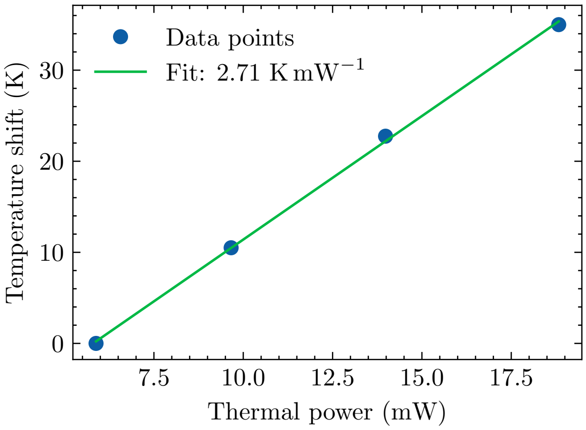

Figure 5.25: The relationship between the thermal power P_{therm} and the wavelength of the same mode. The gradient of this is the thermal resistance R_{therm}, for this 6 µm aperture diameter device 2.71 mW K^{-1}.

5.6.6 Simulated thermal resistance

The self-heating of a device with 6 µm diameter aperture as measured can be simulated. Using a large radius substrate (of 2000 µm and thickness 675 µm), and top and bottom boundary resistances as described above, finds a thermal resistance of 0.93 mW K^{-1} as shown in Figure 5.26. The simulation using bulk material values for the thermal resistivity under-estimates the thermal resistance of the VCSEL by a factor of 3, which is consistent with the experimental measurements in [140]. By adjusting the boundary thermal resistance, the thermal resistance of a model can be adjusted to match experimental results.

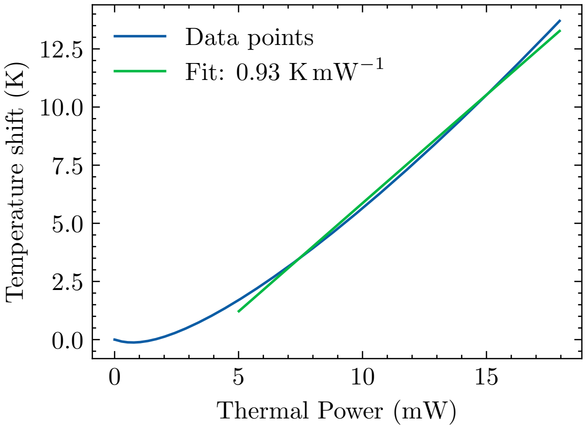

Figure 5.26: The cavity temperature (temperature weighted by optical mode intensity) as a function of the dissipated power P_{therm}. The part of this fit above the lasing threshold current is the thermal resistance comparable to the measured one. The slight dip in the temperature is a simulation artefact that arises from the simulation attempting to account for all the energy in all the mechanisms taking place.

5.7 Conclusions

The simulation of VCSELs is used as a design tool and as a way to better understand the internal physics. Edge-emitting lasers can be simulated in a 1D or 2D x, y software package, but the geometry of VCSELs means that a r, z coordinate system is more appropriate for simulating them, and the Photon Design Harold package is used for this purpose.

The effect of fabrication variations in the dimensions of the p-contact and the doping concentration on the simulation model is shown. This is necessary to understand the validity of comparisons between measurements and simulation outputs. Most of the electrical series resistance is in the p-DBR and p-contact, and so this is where the highest accuracy is required for a faithful representation of the device. It is shown that the total amount of dopant atoms in the p-DBR, as measured using SIMS analysis, is within 4% of the nominal amount. Variations in the p-contact within the range of fabrication uncertainty result in changes in the series resistance of up to $2\,\Omega$, compared to a total resistance of around $50\,\Omega$. The impact on the simulation results on the selection of different boundary conditions was discussed, and values for the thermal and electrical boundary resistances were determined.

The multiphysics model consists of various functional parts that describe the operation of different aspects of the device. Numerical simulation of semiconductors and optoelectronic devices is well-established, such as the k.p model used to simulate the active region [148] and the thermionic emission model to model the current flow across heterointerfaces [149]. These models have been validated against experimental measurements, and their use is well-established. The use of different optical mode solvers to find the lasing modes in VCSELs is also well-understood [55].

A full-device simulation combines uncertainties from all different parts of the model as well as simplifications due to aspects of the physics that are not simulated. The overall accuracy of the model is limited by the uncertainty of the most uncertain parts [150] but there is limited literature on the approximate magnitude or the dominant sources of this error. In [151], a VCSEL design process is presented where measurement results are fitted to simulation results at each design iteration. Adjustment of the simulation parameters in this way maintains a close fit between measured and simulated values, although thermal effects are still difficult to resolve because they affect all asepcts of the physics. Other work such as [48] has investigated the use of fitting procedures to find parameters that minimise the difference between measured and simulated results. However, we have not found any literature that describes the effects of material and fabrication variations on the relationship between measured and simulated results, as examined in this chapter.

The range of numerical parameters required to simulate the optical mode are established. It is shown that fine discretisation in the z-direction of the graded layers in the mirrors is not necessary, but that a large basis of fibre modes is required to prevent spurious modes from being found. Using these parameters it is possible to find the fundamental mode and a number of higher-order modes, which are required for simulating the device at high temperatures. As a result of this work the size of the optical mode solver domain in Harold was decoupled from the size of the electrical and thermal solvers.

The thermal resistance R_{therm} of a VCSEL can be measured from the wavelength shift with temperature. Heat transport in a simulation is found using the material thermal conductivity values, and the location of the heat generation in the model. In VCSEL structures, thermal boundary resistance between layers significantly increases the vertical and lateral heat transport [140], and the model does not account for this effect, leading to an under-estimate of the thermal conductivity by a factor of 3. By adjusting the boundary thermal resistance, the thermal resistance of a model can be adjusted to match experimental results as required.

There are uncertainties in the models that describe the effects that reduce the efficiency of the VCSEL. As these mechanisms are internal, their effects cannot be isolated. At high internal temperatures the losses cause thermal rollover. In the next chapter the effect of aperture size on the rollover current is discussed.

Chapter 6

Measurement and modelling of thermal effects at high temperature

The maximum optical output power of a VCSEL is limited by the thermal rollover, which occurs due to self-heating of the active region. The power conversion efficiency (PCE) is reduced at high internal temperatures by increases in the leakage current, optical absorption, and non-radiative recombination of carriers. For applications such as arrays with high substrate temperatures due to heating, or atomic sensors and fibre-optic datalinks where the device is at a high operating temperature due to the application, the high-temperature characteristics of VCSELs are critical to their overall performance.

Smaller apertures have been observed to turn off at higher internal temperatures than larger ones, and measurements are presented that show this effect. This difference in turnoff temperature is also shown to occur in a simulation model, and an explanation is given in terms of the different profile of the optical modes. Gain spectra at different temperatures are measured using the segmented contact technique, and compared to simulations.

The better performance of small apertures at high temperatures makes them suitable for use in arrays. Using oxide apertures defined by etched posts is a way to define small apertures close together, and the scaling of the maximum optical output power with the number of emitters is discussed.

6.1 Turnoff mechanisms

With an increasing internal temperature, the external differential efficiency drops below 0 and the optical output power rolls over and decreases to zero. Several physical mechanisms, namely the barrier leakage current, Auger recombination, free carrier absorption, and gain peak detuning, are responsible for the drop in efficiency with increasing temperature, and these are discussed in more detail in Section 2.3. The detuning of the gain peak from the peak of the cavity resonance can be found from measurements of the gain spectrum, but the effect of the other mechanisms cannot be straightforwardly quantified from device measurements as they all have the effect of reducing the quantum differential efficiency and increasing the threshold current.

A multiphysics simulation can be used to find the balance of physical mechanisms inside the device. There is a large amount of uncertainty in the descriptions of the physical models and the literature is not settled on which mechanism is principally responsible for the turnoff of VCSELs [47]. As the device becomes less efficient at high temperatures the carrier concentration in the active region increases which further increases the losses, so the turnoff is due to a runaway effect of increasing carrier concentration and falling efficiency.

6.1.1 Stability of high temperature laser output

Close to the lasing turnoff, hysteresis can be observed in the optical power as a function of injection current, depending on which direction the injection current is swept in. This shows that there may be multiple operating regimes for a VCSEL close to turnoff and that high-temperature lasing operation may be unstable. The hysteresis of a VCSEL turnoff with forward and backward-running Light-Current-Voltages (LIVs) is shown in Figure 6.1. For a given injection current, two different operating regimes are possible. These are a lasing condition where the optical output dissipates a significant fraction of the electrical input power, and a higher-temperature non-lasing condition where all of the electrical input power is converted to heat. The potential instability of lasing at high temperatures means that we have to use some care when considering the behaviour of VCSELs at high temperatures.

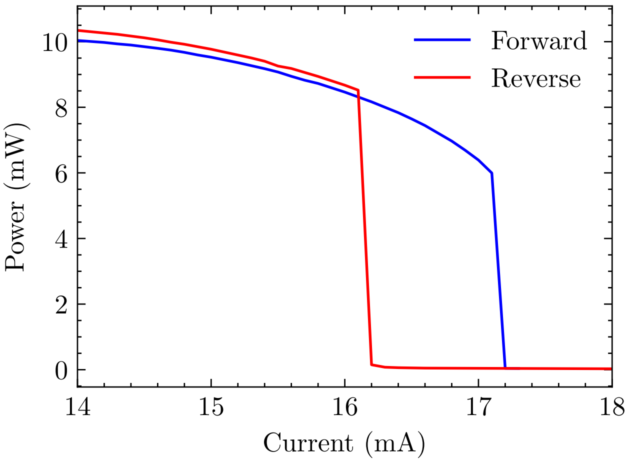

Figure 6.1: Hysteresis in the LI around the rollover and turnoff, showing the forward and backwards running P-I measurements from changing the direction of the sweep on the current source. The presence of this hysteresis means that there are bistable operating conditions around the turnoff point of the laser.

6.2 Measurement of high-temperature characteristics

In [152] it is shown that the junction temperature T_{jcn} and cavity temperature measured by the wavelength shift T_{cav} are within 5 K of each other for a range of VCSEL sizes. Rapid modulation of the injection current, faster than the characteristic thermal response time, is used to measure the external differential efficiency at a constant junction temperature. This is compared to the external differential efficiency for a LI taken in the usual way, with points of constant wavelength found by the dips due to gas absorption lines.

As the substrate temperature increases, the lasing threshold current increases and the rollover and turnoff currents decrease. The intersection of these points is the maximum CW operating temperature $T_{\mathrm{max,cw}}$.

6.2.1 Effect of aperture size on temperature performance

The threshold current, maximum power conversion efficiency, rollover, and turnoff temperature depend on the oxide aperture size. High temperature measurements were performed by Dr. Jack Baker on 940 nm VCSELs with similar characteristics and quantum well properties to the 850 nm structures discussed in the rest of this thesis. These devices were used because the lifetime at high temperatures of the 850 nm devices was too poor to perform a complete set of measurements, possibly due to issues with the contact.

The threshold current, rollover current and maximum maximum power conversion efficiency (PCE) for a range of aperture sizes as a function of heatsink temperature are shown in Figures 6.2, 6.3 and 6.4 respectively. Measurements of the maximum PCE show that larger devices drop off faster with increasing heatsink temperatures. Between 25 and 125 °C the maximum PCE of a large (14.4 µm diameter aperture) device decreases from 40% to 16%, but a smaller (14.4 µm aperture) goes from 37% to 26%. At temperatures above 80 °C, the smaller aperture devices have higher power conversion efficiency. This is within the range of operating temperatures that might be reached in array applications [153].

The maximum CW substrate operating temperature can be found from the intersection of the threshold, rollover and turnoff temperatures. The T_{off} as defined in [152] is found from the intersection of the continuation of the trends of the rollover and turnoff currents with the x-axis. Figure 6.5 shows this for small and large aperture devices. Difficulties in measuring devices at high temperatures mean the data has to be extrapolated to find the turnoff temperature, but it is found to be around 30 °C higher for small (3 µm diameter aperture) compared to larger ones (10 µm).

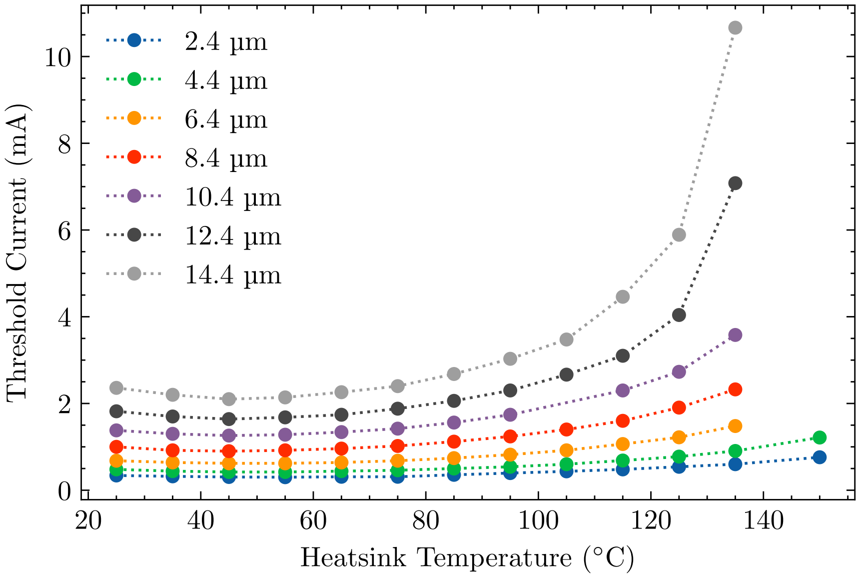

Figure 6.2: The relationship between threshold current and substrate temperature for a range of aperture sizes. The initial decrease in the threshold current is due to the gain spectrum and the cavity wavelength coming into alignment.

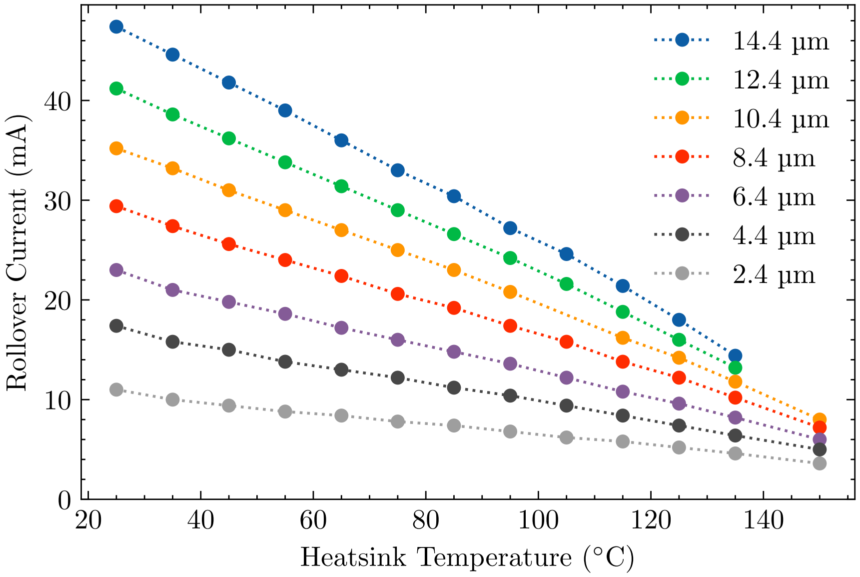

Figure 6.3: The relationship between rollover current and substrate temperature for a range of aperture sizes.

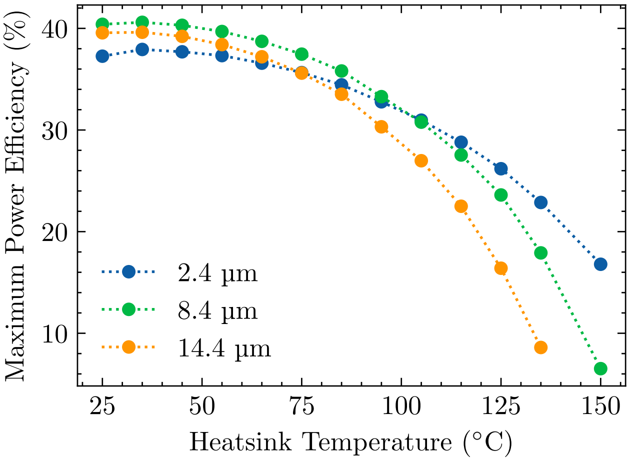

Figure 6.4: The maximum PCE as a function of temperature for different aperture sizes.

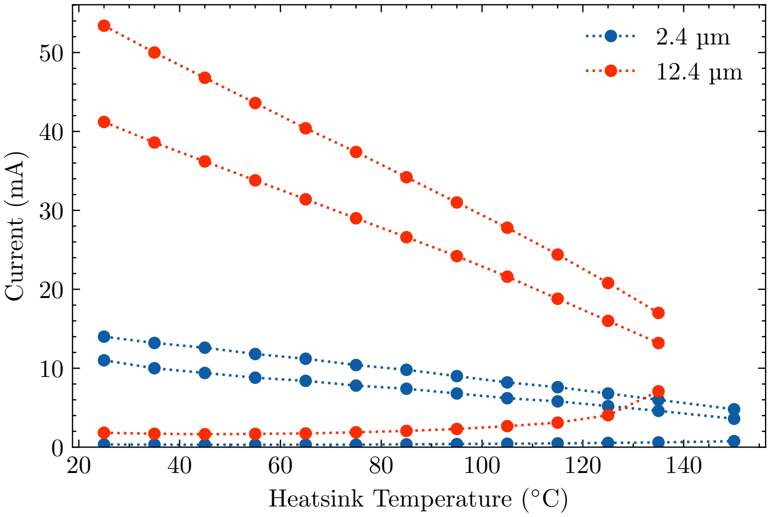

Figure 6.5: The value of $T_{\mathrm{cw,off}}$ can be found from the intersection of the threshold, rollover and turnoff currents at a given substrate temperature. These are shown for aperture sizes of 2.4 and 12.4 µm.

6.2.2 Thermal resistance dependence on aperture size

The thermal resistance of a VCSEL depends on its aperture size. The thermal conductivity is due to heat spreading in 3 dimensions, with the heat generation concentrated in a thin disk-shaped volume corresponding to the active region. Heat is dissipated vertically through an area corresponding to the aperture size, and radially through an area that scales with the circumference so $\propto \sqrt{A}$. The Kaptiza boundary resistance increases the thermal resistance in the vertical direction. Figure 6.6 shows the relationship between the aperture size and the thermal resistance. Smaller apertures have a lower thermal resistance per unit of active region area.

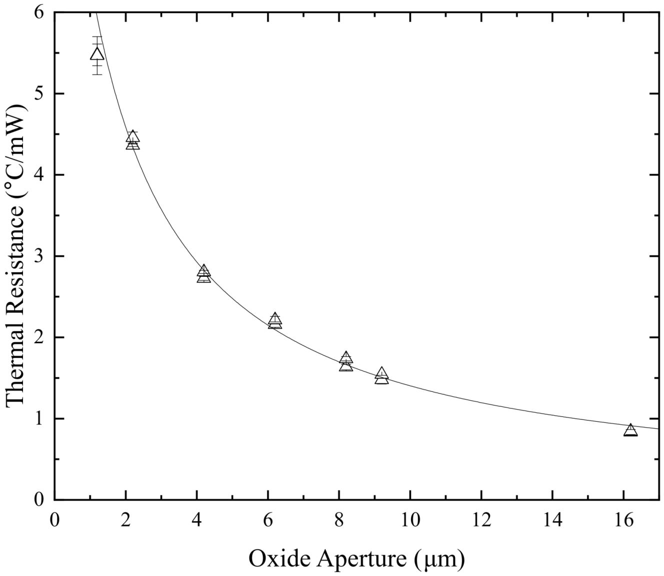

Figure 6.6: The scaling of the thermal resistance with the aperture diameter for 940 nm devices measured above, adapted with permission from [154]. The fit is of the form $1/(2a(x-b))$.

6.3 Measurement and simulation of quantum well gain spectra

The single-pass gain spectra of the multiple quantum well active region can be measured using the segmented-contact technique [117]. Measurements by this method show how the gain characteristics of the quantum well change as a function of temperature and carrier density, and this can be compared to simulations of the gain characteristics. The temperature characteristics of VCSELs are due in part to the detuning of the gain spectrum from the cavity resonance wavelength at elevated temperatures. VCSELs are designed so that the gain spectrum aligns with cavity resonance at the intended operating temperature, Figure 6.2 shows how the threshold current initially decreases with increasing temperature as the gain spectrum and the cavity wavelength align.

6.3.1 Segmented contact method for gain measurements

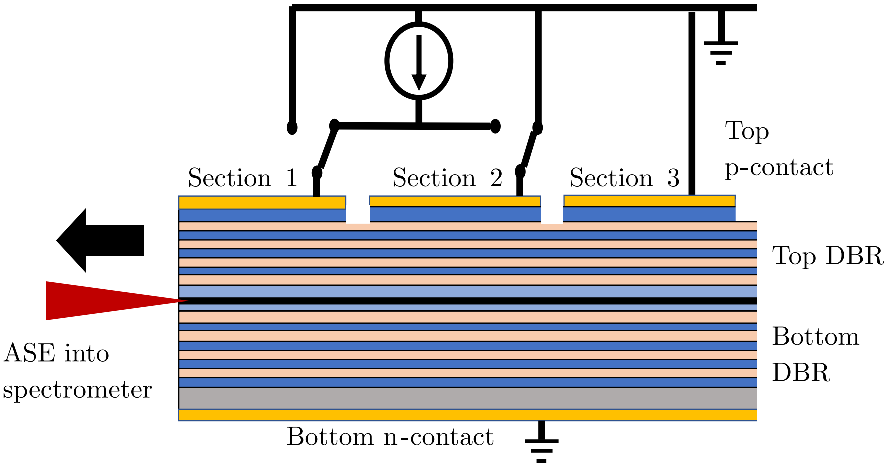

Figure 6.7: The multiple sections of the segmented contact device that was fabricated, adopted from [117].

A structure as shown in Figure 6.7 was fabricated, with ion implantation used to achieve electrical isolation between the sections. Sections of the device are pumped first individually and then simultaneously to change the pumped stripe length, and the optical emission spectrum that outcouples from the end of the device is measured. The net modal gain $G - \alpha_i$ can be calculated from the measured amplified spontaneous emission spectra I_{meas} with a single (1) and then with two (1+2) pumped sections pumped at the same current density. The net modal gain is given by

$$G - \alpha_i = \frac{1}{L} \ln \left(\frac{I_{\text{meas}}\ (1+2)}{I_{\text{meas}}\ (1)} - 1 \right) \tag{6.1}$$

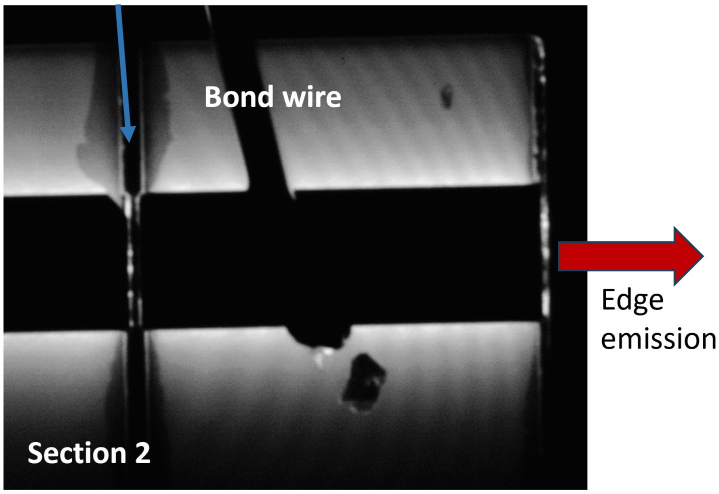

Figure 6.8: A view of the top of the sample with both sections pumped. The light emitted from the sides of the contacts is due to current spreading. The dark region indicated with the blue arrow corresponds to the ion implantation isolation between the sections.

The absorption α_i accounts for the unknown material and free carrier absorption effects. At long wavelengths below the band edge, there are no available transitions, and so the gain and absorption spectra converge to α_i. α_i can vary with carrier density, temperature, wavelength, and the waveguide and mode profile, and so is a significant source of uncertainty.

As shown in Figure 6.8, the ion implantation has a significant effect on the optical output of the device. There are a number of possible reasons for the lack of optical emission from the area of the ion implantation. H^+ ions can cause deep trap states, which provide a route for non-radiative recombination [155]. The active region may be damaged by too-deep ion implantation, preventing optical emission. The ion implantation could mean that the regions under the implantation are not being pumped at all. Implantation can introduce subbandgap absorption, which could result in very strong optical absorption of the emitted light [156]. These effects mean there is some uncertainty in the injection current of the measured results, as there could be significant additional loss of carriers.

6.3.2 Profile of the in-plane optical mode

The modal gain is that experienced by the in-plane mode due to its overlap with the active region of the device. The in-plane mode of the VCSEL structure is due to the waveguiding effect of the higher-index part of the structure around the active region. Figure 6.9 shows the mode and the quantum wells where the Al-fraction goes to 0. This in-plane optical mode is quite different from a vertical VCSEL mode, which has nodes with 0 intensity.

Ideally, only one in-plane mode is guided, so that light coupled to only a single mode is being collected. Its profile can be imaged to verify that it matches the predicted profile, and that spontaneously emitted photons are principally coupled into this mode and not into other modes that can exist in the structure.

The net modal gain $G - \alpha_i$ is related to the material gain g_w by the confinement factor Γ_w.

$$G - \alpha_i = \sum_w \Gamma_w g_w \tag{6.2}$$

The confinement factor relates the values of the modal and material gain. The propagation of the mode is affected by the gain, and so the confinement factor for this purpose is defined in terms of the power flux in the z-direction and the refractive index profile $n_r(y)$. Γ_w is given by [157]

$$\Gamma_w = \varepsilon_0 c_0 \cdot \frac{\int n_r(y) \cdot E^2(y)\, dy}{\int P_z(y)\, ds} \tag{6.3}$$

Γ can also be estimated as the fraction of the square magnitude of the mode profile that overlaps with the quantum wells. For the optical mode profile shown in Figure 6.9, Γ is found to be 0.065 from the overlap of the static field intensity. From a simulation, the ratio between the modal and material gain is found to be 0.062, using the definition in Equation 6.3. The confinement factor given in [117] is between 0.035 and 0.04, for a similar VCSEL structure.

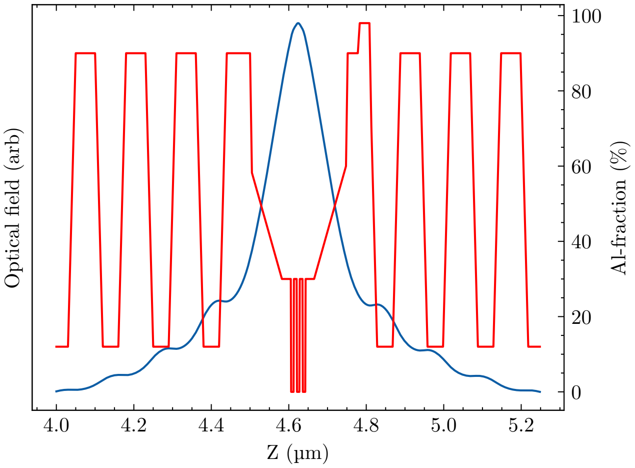

Figure 6.9: The optical intensity of the mode (blue) and the Al-fraction of the stack, showing the quantum wells where the Al-fraction is 0. The confinement factor is the overlap between the optical mode intensity and the quantum wells.

6.3.3 Measurements of gain

A typical threshold current for a 3 µm diameter VCSEL in this material at ambient temperatures is 150 µA, giving a threshold current density of around $2\,\mathrm{kA\,cm^{-2}}$. A test sample from a VCSEL wafer was fabricated with sections 292 µm long with a gap of 8 µm between each one. The sections have a width of 50 µm and a current spreading factor of approximately 0.8 (determined from imaging the near-field of the sample), which increases pumped area. With an effective pumped area of $1.825 \times 10^{-4}\,\mathrm{cm^2}$, the threshold current density corresponds to a current in a section of this area of 365 mA. Measurements were performed at currents from 50 mA to 500 mA in 50 mA steps.

Figure 6.10 shows the measured gain at 50 °C (the approximate intended operating temperature of these VCSELs). The gain increases at all wavelengths with increasing injection current. Figure 6.11 shows the gain spectrum with a current of 500 mA at temperatures of 30, 50 and 70 °C, showing the red-shifting of the peak of the gain spectrum.

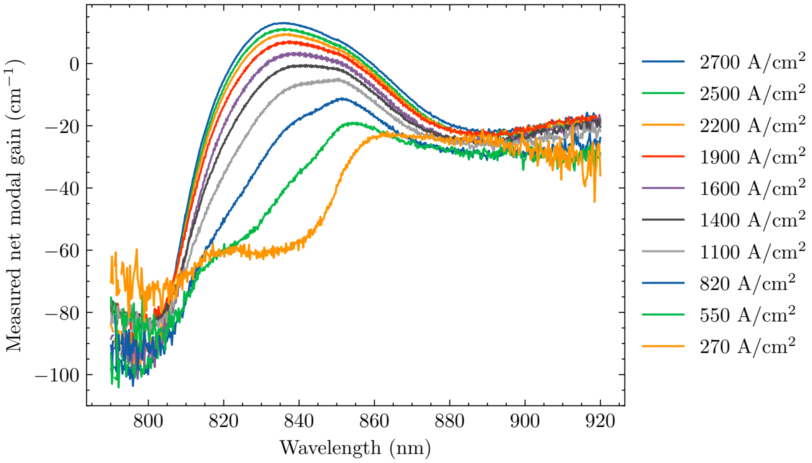

Figure 6.10: At 50 °C (the approximate intended operating temperature of these VCSELs), the measured modal gain spectrum is shown at a range of current densities. The gain increases at all wavelengths with increasing injection current. At longer wavelengths the measured spectra are not representative due to reducing spontaneous emission and different absorption characteristics, and so do not converge to α_i.

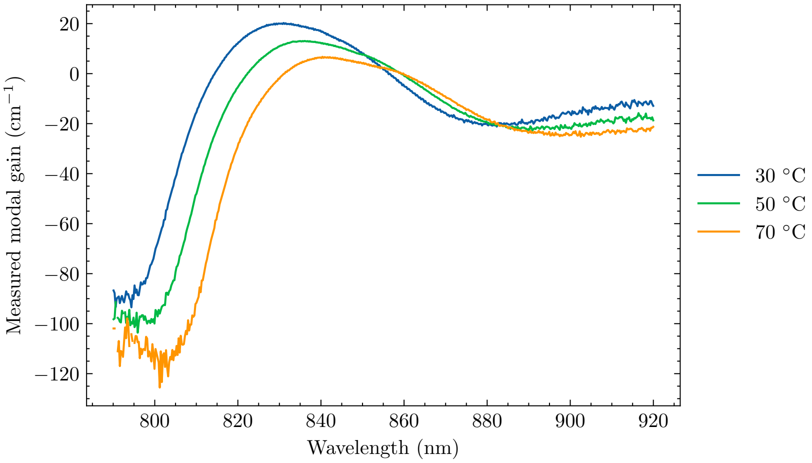

Figure 6.11: The gain spectra at a current of 500 mA (corresponding to a current density of 2700 A cm^{-2}, for temperatures of 30, 50 and 70 °C. At higher temperatures the gain peak broadens, and the peak shifts to longer wavelengths and reduces in magnitude.

6.3.4 Simulation of gain

The segmented contact measurement structure can be represented in a simulation model. A laser diode model with facet reflectivity ≈ 0 is an approximation to the segmented contact structure, as the low facet reflectivity minimises stimulated recombination. The dimensions of the model are the same as the fabricated structure, with the width increased to account for the current spreading factor. The model is solved in one dimension in an isothermal simulation.

The material and modal gain can be found from the simulation. A k.p gain model is used to model the energy transitions in the active region that are responsible for the gain, and so the gain spectrum can be calculated in this way. The k.p model used in the simulation is described in [158]. An α_i of $40\,\mathrm{cm}^{-1}$ is used, as this is the value found in [117].

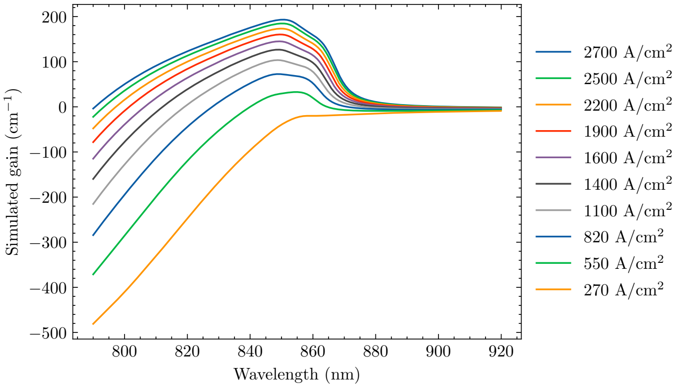

Figure 6.12: The simulated gain spectrum at a temperature of 50 °C for a confinement factor of 0.063 and an α_i of $40\,\mathrm{cm}^{-1}$.

6.3.5 Comparison of measurement and simulation

A comparison can be made of the measured and simulated changes in the gain spectra with injection current and temperature. This shows that the simulation captures the gain-peak detuning from the cavity resonance at elevated operating temperatures. The absolute gain values found from measurement and simulation are different due to uncertainties in the model and the measurement. In the model, there are significant uncertainties in the simulation of the non-radiative recombination, and the optical absorption and scattering. In the measurement, there are uncertainties in the measurement of the current spreading and degree

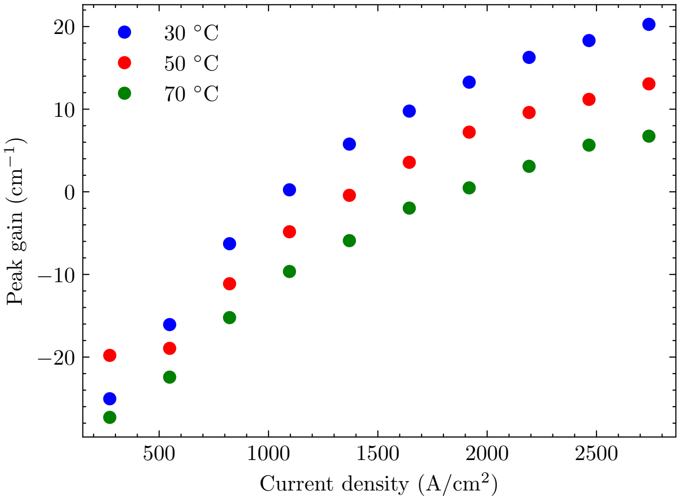

Figure 6.13: The measured peak modal gain, at temperatures of 30, 50 and 70 °C, for a range of injection current densities.

of isolation between sections, and of the loss (through optical absorption or current leakage) due to the ion implantation.

Figure 6.13 shows the measured value of the peak gain for temperatures of 30, 50 and 70 °C. Figure 6.14 shows the comparable simulated result. The absolute values of the gain are very different between the measurement and simulation. Figure 6.15 shows the wavelength of the gain peak with increasing temperature. The measured wavelength shift is $0.24\,\mathrm{nm\,K^{-1}}$, compared to a simulated temperature shift of $0.25\,\mathrm{nm\,K^{-1}}$. There is however a significant offset between the measured and simulated gain peaks of 15 nm.

The gain values obtained in [117] are more consistent with the gain values simulated here. Samples in that work had electrical isolation by a shallow etch instead of ion implantation. An aim of this work was to establish whether ion implantation could be used to perform a more representative gain measurement by preserving more of the material.

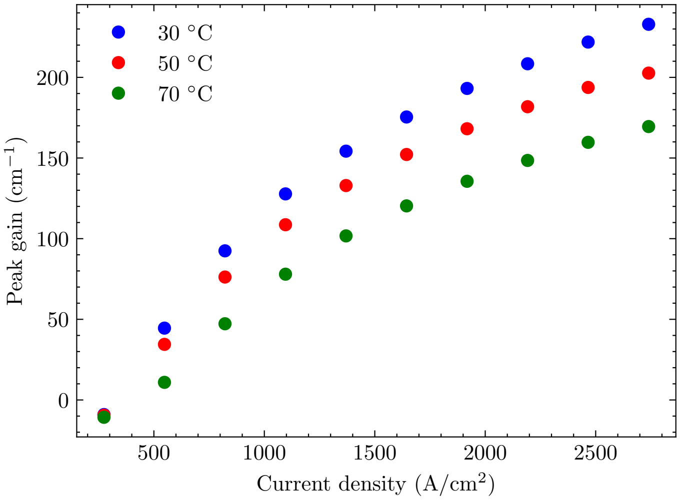

Figure 6.14: The simulated peak gain, at temperatures of 30, 50 and 70 °C.

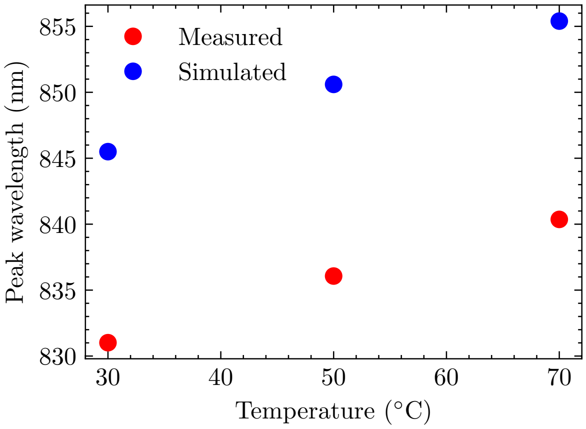

Figure 6.15: The wavelength of the gain peak at a current of 500 mA for the simulations and measurements, showing the change with temperature.

6.4 Simulation of VCSEL rollover

A simulation of the thermal rollover and turnoff can be used to show the effect of self-heating on the optical power output of the device. The rollover and turnoff are determined by the balance of radiative and non-radiative recombination, and the optical loss of the modes. The observed difference of the turnoff temperature between small and large apertures has not been fully explained in the literature and here we attempt to demonstrate the effect with a simplified simulation model.

The optical modes are static throughout the simulation and are calculated for the optical properties of the material at 150 °C. No adjustment of the mode is made to account for thermal lensing or the effects of carrier concentration, or the change in the cavity wavelength. The optical modes also do not represent the full set of optical modes, in particular in the largest device where many modes may lase but the simulation only searches for a limited set. However, the simulated and experimentally observed optical field both show a donut profile in the total optical field, which is the weighted sum of the lasing optical modes. The thermal resistance of the model is controlled by the boundary thermal resistance, and as discussed in the previous chapter in Section 5.6, the use of bulk material values to represent the thermal conductivity results in an underestimate of the device thermal resistance.

Even with this simplified model, we find a 20 °C difference in the rollover temperature for small (3 µm diameter) and large (12 µm diameter) apertures in a simulation. This is broadly consistent with observed results, and suggests that the difference in the turnoff temperature can be explained in terms of the optical field overlap with the carriers in the active region, rather than effects of thermal lensing or some other aperture size-dependent effect, as these are not represented in this simulation.

As the temperature increases the device transitions from the optical power being dominated by laser output to being dominated by spontaneous emission. The simulation only considers modal light outcoupled from the top mirror, whereas the measurement by the integrating sphere also includes some spontaneously emitted light not coupled into a cavity mode. This simulation does not have a temperature-dependent free carrier absorption, whereas some literature suggests that increasing FCA at high temperature could be responsible for a large part of the turnoff [47][159]. The power measurements close to the turnoff are therefore not directly comparable with simulations.

6.4.1 Simulated turnoff

As the device approaches the turnoff temperature, the turn-on becomes softer and the maximum power conversion efficiency is very low. Figure 6.16 shows the modal power of a large-aperture multi-mode VCSEL at a temperature close to the turnoff temperature. This simulation uses 12 optical modes, and it is seen that all of the optical modes undergo thermal rollover at approximately the same current.

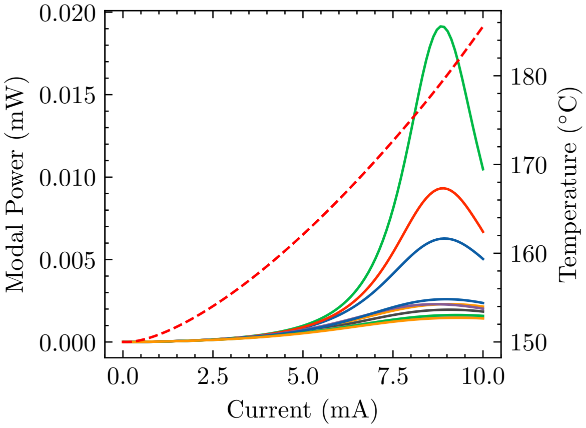

Figure 6.16: A modally-resolved simulated PI for a device with a 12 µm diameter aperture close to turnoff, showing the optical power in different modes. The temperature is shown with a red dashed line and increases superlinearly with injection current due to the increasing voltage across the device. The peak power coincides with a temperature of 180 °C, and this can be determined to be the rollover temperature.

The temperature rises with the thermal power P_{therm}, which is approximately the same as the electrical input power when the power conversion efficiency is low. Once the diode has turned on and the voltage across the device is dominated by the series resistance, the thermal power is approximately $I^2 R_{\text{series}}$, and so the temperature increase from ambient is $I^2 R_{\text{series}} R_{\text{therm}}$. This means that the temperature rises superlinearly with the injection current.

The relationship between the injection current and the internal temperature can be changed by varying the thermal boundary resistance of the model. Figure 6.17 shows the optical power as a function of injection current for a range of thermal boundary resistances. Marked in red is the point of thermal rollover,

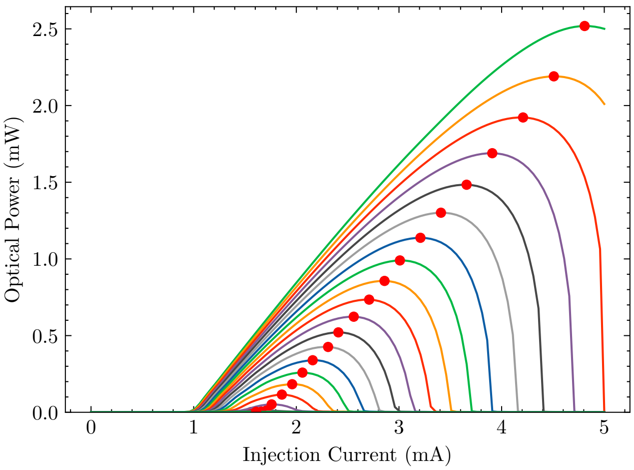

Figure 6.17: The optical power as a function of current for a range of boundary thermal resistance values.

at the maximum optical power, which happens at a range of injection currents. The optical output power can be expressed in terms of the cavity temperature, and is shown in Figure 6.18 for the same device.

This shows that the rollover is due to temperature and not carrier density. Small and large-aperture devices roll over at approximately 195 and 180 °C respectively in the simulation. The rollover temperature cannot be measured experimentally in a rigorous way, but approximately this same temperature difference is observed in the turn-off, which in measured devices occurs at a slightly higher temperature. Figure 6.18 and 6.19 show the optical output power of 3 and 12 µm diameter apertures at a range of temperatures.

These figures show the optical power as a function of temperature for a range of thermal boundary resistances. Marked in red is the point of maximum optical power, or output power decreases to 0. The maximum optical power happens at a different injection current for each thermal boundary resistance but approximately the same temperature, in agreement with the observation in [152] that there is a constant characteristic turnoff temperature for a VCSEL.

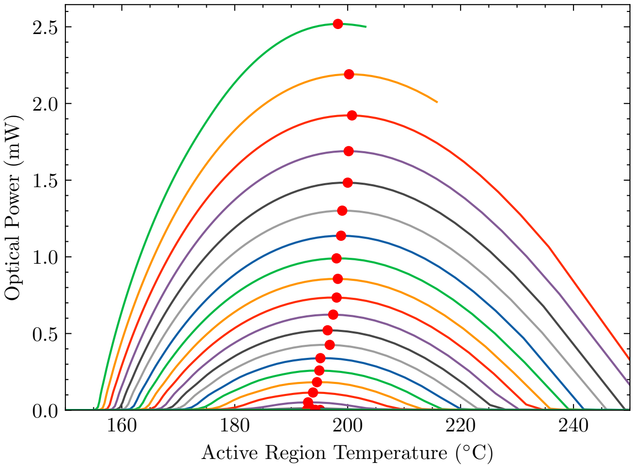

Figure 6.18: The optical power as a function of temperature for a range of thermal boundary resistances for a 3 µm diameter aperture.

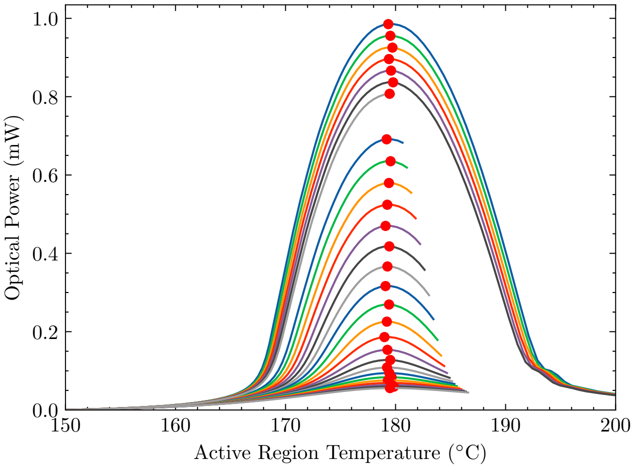

Figure 6.19: The optical power as a function of temperature for a range of thermal boundary resistances for a 12 µm diameter aperture.

6.4.2 Overlap of optical modes with carrier density

The difference in the turn-off temperature of small and large aperture VCSELs can be explained in terms of the different profiles of the optical modes. The electric field is made up of the weighted sum of the power in each of the lasing optical modes. Larger devices, where higher-order modes make up a larger part of the total optical field, have minima and maxima in the field inside the aperture. The lowest order LP11 mode, the fundamental Gaussian mode, has no azimuthal variation, and decays radially from a maximum in the centre of the aperture. In contrast, higher-order modes have minima inside the aperture. Figure 6.20 shows the far-field of large-aperture VCSEL at high current, with a lasing mode that is concentrated around the edge of the aperture with a minima in the middle.

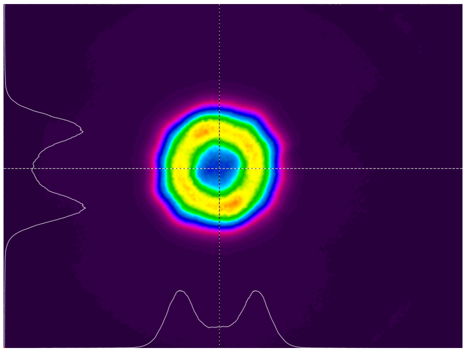

Figure 6.20: The measured far-field profile of a large-aperture VCSEL at high current, showing how the power is concentrated a combination of donut-profiled modes.

Figure 6.21 shows the confined electron density in the quantum wells, and the intensity of the total optical field profile, for large and small aperture VCSELs. The larger-aperture device has a number of minima in the optical mode in regions of high carrier concentration. Stimulated emission is proportional to the intensity of the mode, so where there are minima in the mode non-radiative recombination of carriers is more favourable. In the simulation, mode selection can be influenced by the capture/ escape model in the quantum wells [160].

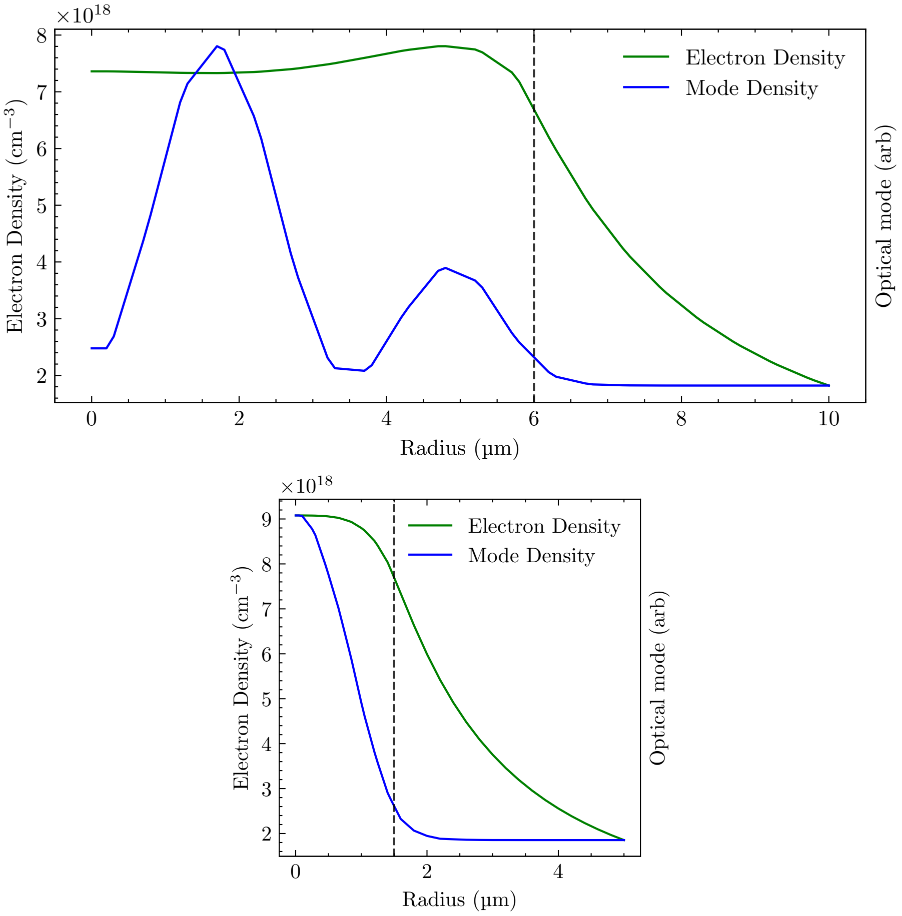

Figure 6.21: The carrier concentration and optical field for small and large aperture device. The edge of the aperture is marked with a black dashed line.

6.5 Use of arrays for increased VCSEL output power

The higher turn-off temperature of small aperture emitters, and lower thermal resistance relative to their active area, means that arrays of small emitters can have favourable high-temperature performance characteristics compared to other types of VCSEL array. The maximum output power of of multiple-emitter “multicellular” designs, as introduced in Section 4.3, is discussed. These use etched posts to define nearly-circular apertures close together, with improved thermal conductivity compared to fully etched mesas with the same spacing as less material is removed.

6.5.1 Scaling of rollover characteristics and thermal resistance with increasing number of emitters

The optical power rollover characteristics with increasing number of emitters is shown in Figure 6.22. The maximum optical power per emitter drops off slightly with increasing numbers of emitters, going from 1.98 mW for a single emitter to 6.72 mW for four emitters (1.68 mW per emitter.)

This can be understood in terms of the thermal resistance per emitter, which is a measure of how much the individual emitters mutually heat each other. The thermal conductivity of the arrays can be measured by tracking output wavelength of one of the emitters. This is shown in Figure 6.23. The thermal conductivity per emitter goes from 0.21 to 0.17 mW/K when scaling from 1 to 4 emitters.

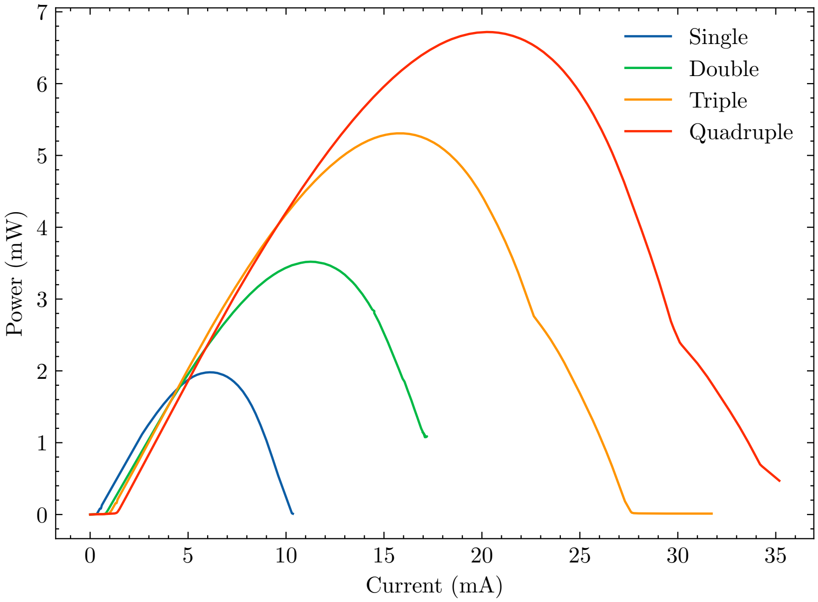

Figure 6.22: With 1-4 emitters, the rollover current and maximum optical power increases nearly linearly.

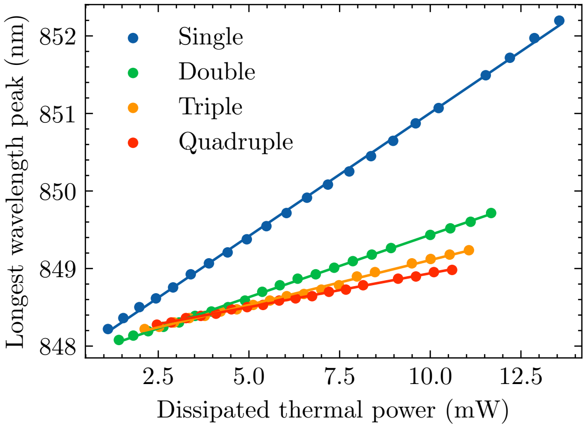

Figure 6.23: The wavelength of 1, 2, 3, and 4 emitter devices as a function of dissipated power, from which R_{therm} can be calculated. At injection currents well below the rollover, the temperature of the emitters tracks and so the temperature distribution in the device is staying the same. Tracking the same feature in each spectrum (the highest-wavelength peak, corresponding to a fundamental mode) is used as a measure of the internal temperature.

6.5.2 Optical properties of multiple emitter designs

At lower currents the temperature distribution in the whole mesa remains even and the temperature of each emitter rises by the same amount, as seen by tracking the wavelengths of the peaks of each emitter. At higher powers, the peaks diverge as one of the diodes draws an increasing amount of power. Figure 6.24 shows the emission wavelengths from each emitter of a 2-aperture device, showing how one of the emitters has a different wavelength shift at a dissipated power above 30 mW, corresponding to the thermal rollover. This behaviour is different between different devices, depending on the characteristics of the individual emitters. These effects are attributed to thermal runaway in one of the diodes, as the diode voltage drops with increasing temperature causing more current to flow by that path. 3 and 4 aperture designs show similar characteristics, but it is harder to resolve the individual peaks than where there are 2 emitters.

6.5.3 Use of small emitters in arrays

These samples were thinned and mounted on a header so their thermal resistance cannot be directly compared to other VCSEL devices. However, the scaling of the thermal resistance with increasing active area can be compared to that shown in Figure 6.6 for single-aperture VCSELs of various aperture sizes. Multiple small apertures have a lower thermal resistance for an equivalent active area than a single-aperture VCSEL. Using the wavelength shift shown in Figure 6.23, the thermal resistance as a function of the effective aperture diameter (corresponding to the diameter of an equivalent active-area single emitter) is shown to scale much better than for single-aperture devices.

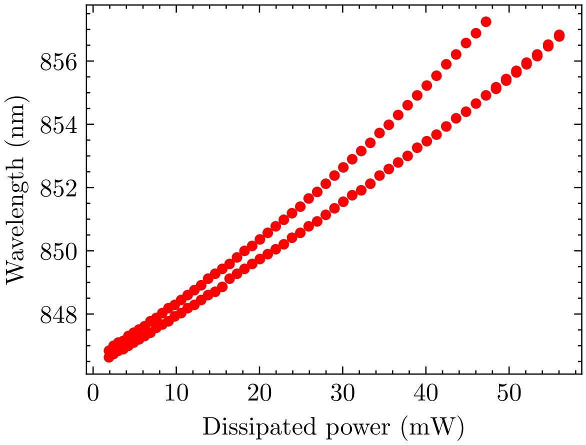

Figure 6.24: For a 2-emitter device, the wavelengths of the 2 peaks are shown as a function of dissipated thermal power. The wavelengths initially track each other as the power increases, and then one of the emitters begins to heat faster and the difference between the emission wavelengths increases.

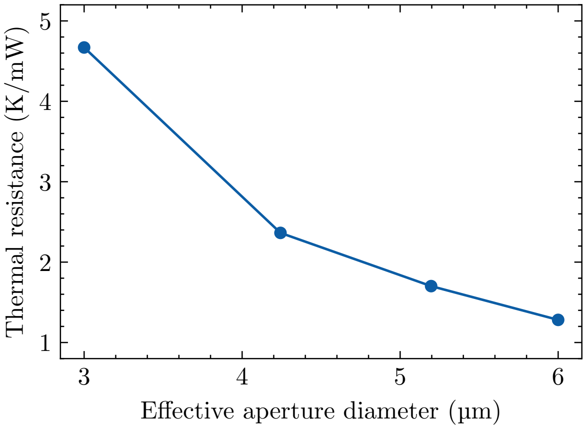

Figure 6.25: The effective aperture area of a array is the aperture diameter of a single-emitter device with the same active area. The scaling of the thermal resistance with the effective aperture area shows that it drops much more rapidly than the thermal resistance of a single emitter with increasing aperture diameter, as shown in Figure 6.6.

6.6 Conclusions

Measurements of VCSELs of different aperture diameters show that small aperture devices have better power conversion efficiency at heatsink temperatures above 100 °C, as well as a higher maximum CW operating temperature.

The gain characteristics can be measured and simulated as a function of temperature. The segmented contact measurement can be used to measure the gain spectrum in a stripe structure, and an equivalent model can be used to find the gain with the k.p model. There are significant uncertainties, in particular in the flow of current to the right part of the structure, and the value of the losses α_i, but the change of the gain peak with temperature is shown to be the same for the measurement and the simulation. The shifting of the gain peak is one of the factors that determines the high-temperature performance of VCSELs, causing a reduction in the power conversion efficiency at temperatures outside of the intended operating range.

The simulation of VCSELs at high temperatures is not straightforward. The internal losses increase exponentially with temperature, and the models that are used to describe these effects have significant uncertainties. A simple model can be used to show a difference in the rollover temperature between small and large devices, suggesting that the difference can be explained in terms of the optical mode profile and the overlap with the carrier concentration in the active region. The changes in this overlap are responsible for many of the effects seen in VCSELs at high temperatures and operating currents, in particular the selection of which modes will lase [54][161]. Current crowding, which is the concentration of the current density at the edge of the aperture, remains a problem in large-diameter VCSELs and this motivates the use of small-aperture emitters for high temperature applications [162].

The better high-temperature performance of small emitters makes them promising for use in arrays, where the substrate temperature is high. An array of small apertures can be defined using etched posts from which the oxide front propagates, whereas typically VCSELs are defined with an etched mesa. This design means the emitters can be defined more closely together while retaining as much material as possible, to reduce the thermal resistance. Although an arrangement of parallel diodes is unstable around threshold and rollover, in the operating regime where the I-V of the diode is linear, this arrangement is stable and power is balanced approximately equally between the emitters. It is shown that arrays of this kind have favourable power scaling characteristics due to better high-temperature characteristics of small emitters. This motivates the investigation of different array designs with small emitters, which may be well-suited to applications where optical power is required at high substrate temperatures.

Chapter 7

Conclusions and future work

This thesis has examined approaches to VCSEL design that could better meet the application requirements for atomic sensors, particularly for higher optical output power. The properties of laterally coupled emitters with conventional epi-material and fabrication techniques were explored. Simulations of VCSELs were compared to measured results to determine the sources of discrepancies between them. The high-temperature characteristics of VCSELs as a function of aperture size were examined, and the results were compared to those of the simulations to try and identify the mechanisms that lead to the thermal rollover. This leads to conclusions about the viability of different ways to achieve increased optical output power and indicates that arrays of small emitters have advantageous scaling properties for use in arrays.

7.1 Conclusions

7.1.1 Use of arrays for increased optical power

Attempts to evanescently couple closely-spaced emitters together did not result in a stable interaction between their individual modes that provided enhanced single-wavelength power. An experiment similar to that performed in [83], was carried out with evanescently coupled emitters defined with oxide apertures. With two emitters spaced 12 µm apart, only a very weak effect was observed, and only for a small number of emitters. The spacing between the apertures is critical for evanescently coupled emitters using conventional VCSEL epimaterial, but the use of oxide apertures to define the emitters places restrictions on the possible geometries.

Different approaches have been investigated in the literature to extend the size of a single-mode VCSEL device in the lateral direction. Larger structures have also been demonstrated, such as large multi-element emitters [127] and arrays using perpendicular facet elements to enhance the horizontal propagation [128]. A general review of methods for lateral coupling of VCSELs is given in [37]. VCSELs for use in atomic sensors have a number of requirements on the quality of the output light in addition to the power and wavelength [15], as well as requirements related to the packaging and integration [15], and so these restrictions will determine the direction of future work on laterally coupled VCSELs.

Closely-spaced arrays of emitters can be defined using etched posts. The rate-limiting step of the thermal oxidation process used to define the oxide aperture is the diffusion and chemical reaction at the oxide front, and so only a small area is needed for the oxidation to spread from. Other work such as [119] has also investigated the use of etched posts to define the shape of the oxide aperture.

In the work described in this thesis, single-mode apertures were patterned less than 15 µm apart on a single mesa, with nearly-circular oxide apertures shown to have similar properties to conventionally-defined apertures. Emitters of this type, with multiple single-mode apertures, have optical output over a narrower range of wavelengths than equivalent-area conventional devices. Experiments suggest that in devices of this type, where the wavelengths align there is no or only a very weak evanescent coupling effect. Measurements of the far-field profile show that the emission is on-axis, because the output of the emitters is not coherent, so there is no interference pattern. This way of pattering emitters is scalable and can be used to define dense arrays of small-aperture emitters. Although devices of this type are not suitable for atomic sensor applications due to the emission at a range of wavelengths, this type of array could be suitable for other applications, in particular due to the better high-temperature performance of small apertures. Arrays of VCSELs are being investigated for a number of applications due to the potential for high optical output powers and simplicity of integration due to the vertical emission of light from the substrate [163]. Future work could be carried out to investigate the scaling of small-aperture emitters, in particular, using short oxide extents to overcome difficulties with oxidation extent non-uniformity.

Variation in the output wavelength between emitters can be determined from the difference in wavelength between adjacent nominally identical devices. From scans of the cavity wavelength across the wafer the expected variation between emitters is $\approx 0.001\,\text{nm}$, but a median variation of $0.25\,\text{nm}$ is observed. This is attributed to fabrication variations, which presents a challenge for fabricating multiple emitters to emit at the same wavelength. The variation in the measured cavity resonance of the material is orders of magnitude smaller than the wavelength of the fabricated emitters, which indicates that the variation in wavelength is due to fabrication variations. For applications that have strict requirements on the output wavelength, variations introduced by the fabrication process are an additional challenge to the yield of devices that meet the specification, and a challenge when fabricating multiple emitters where the wavelengths align to permit coupling.

Photonic crystals are a way to introduce loss for higher-order modes to maintain single-mode lasing for larger apertures at higher currents. Single-mode performance is achieved over a wide range of injection currents, but the higher threshold current means that the power conversion efficiency is low. Using a photonic crystal allows the single-mode aperture size to be increased from 3 to $4.25\,\mu\text{m}$. Further work is required to establish what set of design parameters could lead to a photonic crystal VCSEL that better meets the application requirements of an atomic sensor, in particular the optical power and power conversion efficiency. The power conversion efficiency of the photonic crystals examined here, as well as that of others reported in the literature, is lower than that of conventional oxide-confined VCSELs due to the higher threshold current [164]. This presents an obstacle to their use in miniaturised atomic sensors, where low power consumption of the optical source is required to reach the target size, weight and power.

7.1.2 Simulations

The simulation of VCSELs is used as a design tool and as a way to better understand the internal physics. This is necessary for understanding the operation of VCSELs at the high substrate temperatures required in an atomic sensor, and to understand the effect of variations in the epitaxy and the oxide aperture dimensions on the output wavelength of the device.

The uncertainties in the fabrication of the device can be accounted for. A SIMS analysis of the composition can be used to show that the material was grown as specified. The range of numerical parameters required make finding the optical modes tractable was established. Heat transport in a simulation is found using the material thermal conductivity values, and the location of the heat generation in the model. In VCSEL structures, thermal boundary resistance between layers significantly increases the vertical and lateral heat transport [140], and the model does not account for this effect, leading to an under-estimate of the thermal conductivity by a factor of 3.

The comparison of simulated and measured results and the resulting discussion with the developers of the Harold software resulted in some improvements to the VCSEL module. A thermionic emission model was ported from the Harold-XY module to model the current transport over heterointerfaces, and the optical and electrical/thermal simulation domain sizes were decoupled.

There are uncertainties in the models that describe the effects that reduce the efficiency of the VCSEL and lead to the thermal rollover in the optical power at high temperatures. As these mechanisms are internal, their effects cannot be isolated, and so there is significant uncertainty in how well the simulation describes the regime around the thermal rollover. The thermal rollover mechanisms in VCSELs are discussed in the literature, but there is not a clear consensus on which mechanisms are principally responsible for the thermal rollover [47][159].

7.1.3 Thermal effects

Measurements of VCSELs of different aperture diameters show that small aperture devices have better power conversion efficiency at heatsink temperatures above 100 °C, as well as a higher maximum CW operating temperature. Additionally, small apertures have relatively lower thermal resistance for their active region area, as the heat spreads in 3 dimensions. Most of the thermal resistance is due to the material in the immediate vicinity of the device.

The gain characteristics can be measured and simulated as a function of temperature. The segmented contact measurement can be used to measure the gain spectrum in a stripe structure, and an equivalent model can be used to find the gain with the k.p model. There are significant uncertainties, in particular in the flow of current to the right part of the structure, and the value of the losses α_i, but the change of the gain peak with temperature is shown to be the same for the measurement and the simulation.

The simulation of VCSELs at high temperatures is not straightforward. The internal losses increase exponentially with temperature, and the models that are used to describe these effects have significant uncertainties. A simple model can be used to replicate the observed difference in the rollover temperature between small and large devices, suggesting that the difference can be explained in terms of the optical mode profile and the overlap with the carrier concentration in the active region. Current crowding, which is the concentration of the current density at the edge of the aperture, is a problem in large-diameter VCSELs and this motivates the use of small-aperture emitters for high temperature applications [162].

The better high-temperature performance of small emitters makes them promising for use in arrays, where the substrate temperature is high. An array of small apertures can be defined using etched posts from which the oxide front propagates, whereas typically VCSELs are defined with an etched mesa. This design means the emitters can be defined more closely together while retaining as much material as possible, to reduce the thermal resistance. Although an arrangement of parallel diodes is unstable around threshold and rollover, in the operating regime where the I-V of the diode is linear, this arrangement is stable and power is balanced approximately equally between the emitters. It is shown that arrays of this kind have favourable power scaling characteristics due to better high-temperature characteristics of small emitters. The thermal conductivity per emitter goes from 0.21 to $0.17\,\mathrm{mW\,K^{-1}}$ when scaling from 1 to 4 emitters. A large part of the thermal resistance of a VCSEL is due to material in the immediate vicinity of the active region, and devices patterned in this way could have useful scaling properties, and better high-temperature performance than arrays defined with larger emitters.

7.2 Future work

Research on improved VCSEL performance has a number of different directions. At present, major commercial applications of VCSELs are in telecommunications (for short-range optical links), in LiDAR for illumination and ranging, and for atomic sensors. Future applications include for neural networks [165], where the non-linear spiking properties of VCSELs are used as artificial neurons, and in materials processing using the high power densities that can be achieved with arrays [163].

In all these applications, higher optical power, a wider range of operating conditions, and control of the characteristics of the optical modes are required. Methods used to achieve this in the literature include surface relief and induced disorder, which suppress the lasing of higher-order modes. Experiments described in this thesis point towards some other routes that could also be investigated.

7.2.1 Stacked junction VCSELs

Extension of the device in the vertical dimension can be achieved by using a stacked junction VCSEL. Tunnel junctions are used to recycle carriers, resulting in higher quantum efficiencies, and higher power conversion efficiencies. A typical structure is shown in Figure 7.1. At present this type of device has been commercialised at wavelengths at 980 nm for LIDAR applications [43], and studied at wavelengths including 850 nm [44]. The longer photon lifetime of these devices may also have favourable linewidth properties. Such devices also achieve excellent power output efficiency, with values being reported as high as 60%, compared to less than 50% for conventional VCSEL designs.

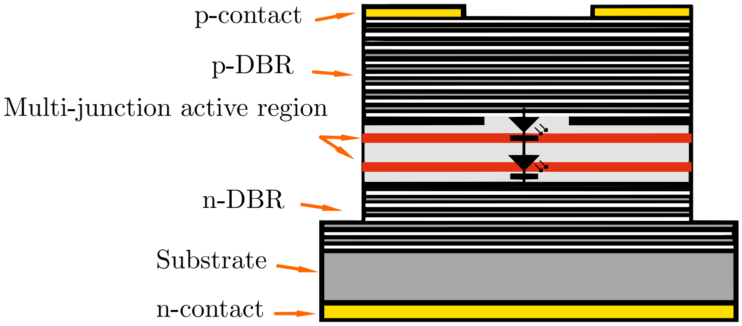

Figure 7.1: Typical buried tunnel VCSEL structure.

In the AlGaAs material system, tunnel junctions can be realised with a contrast between high material that is oppositely doped. Band-to-band tunnelling can occur, so that electrons move from the valence to the conduction band at the interface. This type of structure can be grown using MOVPE, and fabricated using conventional VCSEL processing techniques.

Typically multiple oxide apertures are required, because current spreading in the tunnel junctions reduces their performance. This increases the confinement strength, potentially meaning that this type of device has a larger number of lasing modes. Using photonic crystal mode control with stacked junction material, and using ion implantation to define the flow of the carriers into the active region, could result in a device with high SMSR and narrow linewidth, which is required for atomic clock applications.

7.2.2 Closely-spaced arrays defined using surface relief

Surface relief etches could be used to define the location of the emission apertures. Closely-spaced emitters similar to the multicellular devices could be patterned on an extended device, similar to that proposed in [166] but spaced so as to not achieve optical coupling between the emitters. The use of a surface relief allows the oxide aperture to be extended while retaining single-mode lasing in each emitter, improving the thermal performance and longevity of the device.

7.2.3 Arrays patterned using etched posts

Different array configurations can be patterned using etched posts. The hexagonal cell layout of emitters shown in Section 4.3 is scalable to an arbitrarily large number of emitters. Arrays of this type have the advantage of on-axis optical power output due to the Gaussian mode in each of the emitters, and better high-temperature due to the better high-temperature of small VCSEL apertures compared to larger ones.

As an array becomes larger, the thermal resistance will become dominated by the substrate thermal resistance, and so the potential scaling advantages of this type of array with small emitters will be lost. As the array becomes larger, the uneven heating broadens the range of emission wavelengths [167]. Arrays with uneven spacing of emitters, or arrays of small groups of emitters, could be used to balance the heating and maintain optical emission over a narrow range of wavelengths.

7.2.4 Improved thermal characteristics using etched posts

The thermal resistance of a VCSEL is determined by the amount of material through which heat can be dissipated into the substrate. The Kapitza thermal boundary resistance increases the resistance in the vertical direction, and measurements suggest this increase could be by up to an order of magnitude

[140]. Making the mesa diameter larger will improve the thermal resistance, but controlling the oxide extent becomes more challenging for larger mesas. Non-uniformity in the oxide due to crystal-axis dependent progression rates, and rate non-uniformities across the wafer, make achieving a particular aperture size challenging. Using etched posts, more of the mesa can be preserved to retain thermal mass, with a short oxide extent allowing better control of the dimensions.

7.2.5 Polarisation control using etched posts

The use of etched posts to define the oxide aperture result in a slightly non-circular oxide shape. This effect could be employed to introduce an anisotropy that fixes the lasing polarisation direction. The devices fabricated in this project have the axes of symmetry offset from the crystal axes, similar devices would need to be rotated by 45° to examine this effect. The use of a sub-wavelength grating to define the polarisation is well established, but this requires additional processing steps with e-beam lithography.

7.2.6 Simulations

From collaborating with Photon Design, some changes were introduced to the Harold VCSEL module, such as a thermionic emission model previously available on the XY solver, and the ability to have a smaller mode solver radius from the rest of the model.

Other changes could be made to the simulation software. Control of the m, p quantum numbers that describe the basis of modes that are searched for would allow examination of particular classes of modes. Numerical improvements could be made such as using more transverse modes around the aperture region, where the optical mode is the most intense and the aperture scattering takes place.

The thermal model does not account for the boundary resistance between materials, which measurements show increases the thermal resistance in the vertical direction by up to an order of magnitude [140]. This is known as the Kapitza resistance and is due to the effect of phonon scattering at the material interface [168]. Introducing thermal resistances would mean that the software could be used for more representative investigations of the thermal resistance and self-heating of different devices, such as to investigate the effect of varying the mesa diameter on the thermal resistance of a VCSEL. Ab-inito simulations of the thermal conductivity of crystalline materials is possible but computationally expensive, and so the simplest approach is likely to be some scaling of the thermal resistance of the VCSEL mirrors to account for the phonon scattering [169].

The loss parameters that describe the leakage current, Auger recombination, and FCA are derived from measurements of material properties, and from empirical and semi-empirical arguments. Automatic fitting of these parameters can be performed to fit experimental measurements to simulation results [48]. This would allow further work to be done to better understand the performance of VCSELs at high temperatures and develop a robust explanation for the dependence of the turnoff temperature on the aperture size.

Bibliography

[1] Hui Li et al. “Vertical-Cavity Surface-Emitting Lasers for Optical Interconnects”. In: *SPIE Newsroom* (2014).

[2] Thomas P Heavner and Steven R Jefferts. “The Realization of the SI Second and Generation of UTC(NIST) at the Time and Frequency Division of the National Institute of Standards and Technology (NIST) +”. In: (2007).

[3] David B. Newell. “A More Fundamental International System of Units”. In: *Physics Today* 67.7 (2014), pp. 35–41.

[4] John Kitching, Svenja Knappe, and Elizabeth A. Donley. “Atomic Sensors – A Review”. In: *IEEE Sensors Journal* 11.9 (2011), pp. 1749–1758.

[5] J. Kitching et al. “A Microwave Frequency Reference Based on VCSEL-driven Dark Line Resonances in Cs Vapor”. In: *IEEE Transactions on Instrumentation and Measurement* 49.6 (2000), pp. 1313–1317.

[6] R. Lutwak et al. “CSAC - the Chip-Scale Atomic Clock”. In: *Frequency Standards and Metrology*. World Scientific, 2009, pp. 454–462.

[7] M Haji et al. *Holdover Atomic Clock Landscape Review*. Tech. rep. National Physical Laboratory, 2024.

[8] P. Bevington, R. Gartman, and W. Chalupczak. “Inductive Imaging of the Concealed Defects with Radio-Frequency Atomic Magnetometers”. In: *Applied Sciences* 10.19 (2020).

[9] Ryan M. Hill et al. “A Tool for Functional Brain Imaging with Lifespan Compliance”. In: *Nature Communications* 10.1 (2019), p. 4785.

[10] V. Ligeret et al. "High Power Al-Free DFB Laser Diode for Atomic Clocks: Narrow Line-Width and Demonstration of Saturation Spectra of the Cesium D2 Line". In: *Semiconductor Lasers and Laser Dynamics III*. Vol. 6997. International Society for Optics and Photonics, 2008, 69971T.

[11] N. von Bandel et al. "DFB-Ridge Laser Diodes at 894 nm for Cesium Atomic Clocks". In: *Quantum Sensing and Nano Electronics and Photonics XIII*. Vol. 9755. International Society for Optics and Photonics, 2016, 97552K.

[12] Darwin K. Serkland et al. "Mode Selection and Tuning of Single-Frequency Short-Cavity VECSELs". In: *Vertical-Cavity Surface-Emitting Lasers XXII*. Vol. 10552. SPIE, 2018, pp. 18–28.

[13] Huiyao Yu et al. "Key Technologies in Developing Chip-Scale Hot Atomic Devices for Precision Quantum Metrology". In: *MICROMACHINES* 15.9 (2024), p. 1095.

[14] C. Johnson, P. Schwindt, and M. Weisend. "Multi-Sensor Magnetoencephalography with Atomic Magnetometers." In: *Physics in medicine and biology* (2013).

[15] D. K. Serkland et al. "VCSELs for Atomic Sensors". In: *Vertical-Cavity Surface-Emitting Lasers XI*. Vol. 6484. International Society for Optics and Photonics, 2007, p. 648406.

[16] Ahmed Al-Samaneh. "VCSELs for Cesium-Based Miniaturized Atomic Clocks". PhD thesis. Universität Ulm, 2014.

[17] Pingping Qiu et al. "Fabrication and Characterization of Low-Threshold Single Fundamental Mode VCSELs with Dielectric DBR Mirror". In: *IEEE Photonics Journal* 13.4 (2021), pp. 1–6.

[18] *UK Quantum Technologies Challenge*. Tech. rep. UKRI, 2022.

[19] Jack Baker. "Material and Device Characterisation in the Volume Manufacture of VCSELs". PhD thesis. Cardiff University, 2023.

[20] "Remembering the Laser Diode". In: *Nature Photonics* 6.12 (2012), pp. 795–795.

[21] H. Kroemer. "A Proposed Class of Hetero-Junction Injection Lasers". In: *Proceedings of the IEEE* 51.12 (1963), pp. 1782–1783.

[22] R. Dingle, W. Wiegmann, and C. H. Henry. “Quantum States of Confined Carriers in Very Thin AlGaAs-GaAs-AlGaAs Heterostructures”. In: *Physical Review Letters* 33.14 (1974), pp. 827–830.

[23] Kenichi Iga. “Forty Years of Vertical-Cavity Surface-Emitting Laser: Invention and Innovation”. In: *Japanese Journal of Applied Physics* 57.8S2 (2018), 08PA01.

[24] Haruhisa Soda et al. “GaInAsP/InP Surface Emitting Injection Lasers”. In: *Japanese Journal of Applied Physics* 18 (1979), p. 2329.

[25] Milton Feng, Chao-Hsin Wu, and Nick Holonyak. “Oxide-Confined VCSELs for High-Speed Optical Interconnects”. In: *IEEE Journal of Quantum Electronics* 54.3 (2018), pp. 1–15.

[26] Y.H. Lee, Y.G. Ju, and I.Y. Han. “780-nm VCSELs for CD applications”. In: *Conference Proceedings. LEOS’98. 11th Annual Meeting. IEEE Lasers and Electro-Optics Society 1998 Annual Meeting (Cat. No.98CH36243).* Vol. 1. 1998, p. 214.

[27] Dr Rüdiger Paschotta. “Vertical Cavity Surface-emitting Lasers”. In: *RP Photonics Encyclopedia* (2006).

[28] Tatsuo Hariyama et al. “High-Accuracy Range-Sensing System Based on FMCW Using Low-Cost VCSEL”. In: *Optics Express* 26.7 (2018), pp. 9285–9297.

[29] Lijuan Lan et al. “VCSEL-Based Atmospheric Trace Gas Sensor Using First Harmonic Detection”. In: *IEEE Sensors Journal* 19.13 (2019), pp. 4923–4931.

[30] Shuiying Xiang et al. “Computing Primitive of Fully VCSEL-Based All-Optical Spiking Neural Network for Supervised Learning and Pattern Classification”. In: *IEEE Transactions on Neural Networks and Learning Systems* 32.6 (2021), pp. 2494–2505.

[31] *Apple iPad Pro LiDAR Module.* Tech. rep. System Plus Consulting, 2020.

[32] Hai Huang et al. “Unveiling the Potential of Photonic Crystal Surface Emitting Lasers: A Concise Review”. In: *Semiconductor Science and Technology* (2025).

[33] Yuhki Itoh et al. “High-Power and High-Efficiency Operation of 1.3 µm-Wavelength InP-based Photonic-Crystal Surface-Emitting Lasers with Metal Reflector”. In: *Optics Express* 32.7 (2024), pp. 12520–12527.

[34] Antoine Pissis et al. “Efficient Tunnel Junction Lithographic Aperture 940 Nm VCSEL”. In: *IEEE Photonics Technology Letters* 35.7 (2023), pp. 389–392.

[35] Xiaoli Zhou et al. “High-Power Low-Divergence Single-Mode Multi-Junction Cascade VCSELs”. In: *IEEE Transactions on Electron Devices* (2024), pp. 1–5.

[36] Babu Dayal Padullaparthi, Jim Tatum, and Kenichi Iga. *VCSEL Industry: Communication and Sensing*. John Wiley & Sons, 2021.

[37] Dominic F. Siriani and Kent D. Choquette. “Chapter 6 - Coherent Coupling of Vertical-Cavity Surface-Emitting Laser Arrays”. In: *Semiconductors and Semimetals*. Ed. by James J. Coleman, A. Catrina Bryce, and Chennupati Jagadish. Vol. 86. Advances in Semiconductor Lasers. Elsevier, 2012, pp. 227–267.

[38] Johannes Michael Ostermann et al. “Surface Gratings for Polarization Control of Single- and Multi-Mode Oxide-Confined Vertical-Cavity Surface-Emitting Lasers”. In: *Optics Communications* 246.4 (2005), pp. 511–519.

[39] Patrick Su et al. “High-Power Single-Mode Vertical-Cavity Surface-Emitting Lasers Using Strain-Controlled Disorder-Defined Apertures”. In: *Applied Physics Letters* 119.24 (2021), p. 241101.

[40] Alessandro Massaro. *Photonic Crystals: Innovative Systems, Lasers and Waveguides*. BoD – Books on Demand, 2012.

[41] Péter Nyakas. “Honeycomb Photonic Crystal Vertical-Cavity Surface-Emitting Lasers: Coupled Cavities Enhancing the Single-Mode Range”. In: *Journal of the Optical Society of America B* 30.12 (2013), p. 3284.

[42] Dominic F. Siriani, Paul O. Leisher, and Kent D. Choquette. “Loss-Induced Confinement in Photonic Crystal Vertical-Cavity Surface-Emitting Lasers”. In: *IEEE Journal of Quantum Electronics* 45.7 (2009), pp. 762–768.

[43] *Vixar Launches High Efficiency Multi-Junction VCSEL*. compoundsemiconductor.net. 2020.

[44] P. S. Wong et al. “Tunnel Junction 850-Nm VCSEL for Aperture Uniformity and Reliability”. In: *Vertical-Cavity Surface-Emitting Lasers XXI*. Vol. 10122. SPIE, 2017, pp. 72–76.

[45] Yao Xiao et al. “Multi-Junction Cascaded Vertical-Cavity Surface-Emitting Laser with a High Power Conversion Efficiency of 74%”. In: *Light: Science & Applications* 13.1 (2024), p. 60.

[46] Alberto Tibaldi et al. “VENUS: A Vertical-Cavity Surface-Emitting Laser Electro-Opto-Thermal NUmerical Simulator”. In: *IEEE Journal of Selected Topics in Quantum Electronics* 25.6 (2019), pp. 1–12.

[47] Pierluigi Debernardi et al. “Probing Thermal Effects in VCSELs by Experiment-Driven Multiphysics Modeling”. In: *IEEE Journal of Selected Topics in Quantum Electronics* 25.6 (2019), pp. 1–14.

[48] Jung-Tack Yang, Hyewon Han, and Woo-Young Choi. “Deep Learning-based Extraction of Auger and FCA Coefficients in 850 Nm GaAs/AlGaAs Laser Diodes”. In: *Current Optics and Photonics* 8.1 (2024), pp. 80–85.

[49] Curtis Hentschel. “Device and Material Characterisation of Vertical Cavity Surface Emitting Lasers”. PhD thesis. Cardiff University, 2023.

[50] B. Romero et al. “Simple Model for Calculating the Ratio of the Carrier Capture and Escape Times in Quantum-Well Lasers”. In: *Applied Physics Letters* 76.12 (2000), pp. 1504–1506.

[51] P. Blood. *Quantum Confined Laser Devices: Optical Gain and Recombination in Semiconductors.* First edition. Oxford Master Series in Physics. Atomic, Optical, and Laser Physics 23. Oxford: Oxford University Press, 2015.

[52] Sadao Adachi. “GaAs, AlAs, and AlGaAs: Material Parameters for Use in Research and Device Applications”. In: *Journal of Applied Physics* 58.3 (1985), pp. 1–29.

[53] M. Linnik and A. Christou. “Optical Properties of AlGaAsSb, AlGalnP, AlGaInAs, and GaInAsP for Optoelectronic Applications”. In: *MRS Online Proceedings Library (OPL)* 579 (1999), p. 201.

[54] R. Michalzik and K. J. Ebeling. “Operating Principles of VCSELs”. In: *Vertical-Cavity Surface-Emitting Laser Devices.* Ed. by Takeshi Kamiya et al. Vol. 6. Berlin, Heidelberg: Springer Berlin Heidelberg, 2003, pp. 53–98.

[55] P. Bienstman et al. “Comparison of Optical VCSEL Models on the Simulation of Oxide-Confined Devices”. In: *IEEE Journal of Quantum Electronics* 37.12 (2001), pp. 1618–1631.

[56] D. Burak and R. Binder. “Cold-Cavity Vectorial Eigenmodes of VCSELs”. In: *IEEE Journal of Quantum Electronics* 33.7 (1997), pp. 1205–1215.

[57] G. Ronald Hadley. “Effective Index Model for Vertical-Cavity Surface-Emitting Lasers”. In: *Optics Letters* 20.13 (1995), pp. 1483–1485.

[58] E. R. Hegblom et al. “Scattering Losses from Dielectric Apertures in Vertical-Cavity Lasers”. In: *IEEE Journal of Selected Topics in Quantum Electronics* 3.2 (1997), p. 379.

[59] Jae-Heon Shin, Il-Young Han, and Yong-Hee Lee. “Very Small Oxide-Confined Vertical Microcavity Lasers with High-Contrast AlGaAs-Al(x)O(y) Mirrors”. In: *IEEE Photonics Technology Letters* 10.6 (1998), pp. 754–756.

[60] M.J. Noble, J.P. Loehr, and J.A. Lott. “Analysis of Microcavity VCSEL Lasing Modes Using a Full-Vector Weighted Index Method”. In: *IEEE Journal of Quantum Electronics* 34.10 (1998), pp. 1890–1903.

[61] B.R. Bennett, R.A. Soref, and J.A. Del Alamo. “Carrier-Induced Change in Refractive Index of InP, GaAs and InGaAsP”. In: *IEEE Journal of Quantum Electronics* 26.1 (1990), pp. 113–122.

[62] Chun-Yen Peng et al. “Investigation of the Current Influence on Near-Field and Far-Field Beam Patterns for an Oxide-Confined Vertical-Cavity Surface-Emitting Laser”. In: *Optics Express* 28.21 (2020), p. 30748.

[63] J. Talghader and J. S. Smith. “Thermal Dependence of the Refractive Index of GaAs and AlAs Measured Using Semiconductor Multilayer Optical Cavities”. In: *Applied Physics Letters* 66.3 (1995), pp. 335–337.

[64] A. K. Jansen van Doorn, M. P. van Exter, and J. P. Woerdman. “Elasto-Optic Anisotropy and Polarization Orientation of Vertical-Cavity Surface-Emitting Semiconductor Lasers”. In: *Applied Physics Letters* 69.8 (1996).

[65] Johannes Michael Ostermann and Michael C Riedl. *Polarization Control of VCSELs*. Tech. rep. 2003: University of Ulm.

[66] Lei Xiang et al. “VCSEL Mode and Polarization Control by an Elliptic Dielectric Mode Filter”. In: *Applied Optics* 57.28 (2018), pp. 8467–8471.

[67] J. Hader, J. V. Moloney, and S. W. Koch. “Beyond the ABC: Carrier Recombination in Semiconductor Lasers”. In: *Physics and Simulation of Optoelectronic Devices XIV*. Vol. 6115. SPIE, 2006, pp. 304–310.

[68] Larry A. Coldren, Scott W. Corzine, and Milan L. Mašanović. *Diode Lasers and Photonic Integrated Circuits*. 2nd ed. Wiley Series in Microwave and Optical Engineering. Hoboken, N.J: Wiley, 2012.

[69] S. Hausser et al. "Auger Recombination in Bulk and Quantum Well InGaAs". In: *Applied Physics Letters* 56.10 (1990), pp. 913–915.

[70] A. D. Andreev and G. G. Zegrya. "Auger Recombination in Strained Quantum Wells". In: *Semiconductors* 31.3 (1997), pp. 297–303.

[71] P. Grivickas et al. "Intrinsic Shape of Free Carrier Absorption Spectra in 4H-SiC". In: *Journal of Applied Physics* 125.22 (2019), p. 225701.

[72] JOACHIM Piprek, ed. *Semiconductor Optoelectronic Devices Introduction to Physics and Simulation*. Boston: Academic Press, 2003.

[73] J.-P. Weber. "Optimization of the Carrier-Induced Effective Index Change in InGaAsP Waveguides-Application to Tunable Bragg Filters". In: *IEEE Journal of Quantum Electronics* 30.8 (1994), pp. 1801–1816.

[74] K A Bulashevich et al. "Effect of free-carrier absorption on performance of 808 nm AlGaAs-based high-power laser diodes". In: *Semiconductor Science and Technology* 22.5 (2007), pp. 502–510.

[75] Abid Khan. "Vertical Cavity Surface Emitting Lasers: Design, Characterisation and Integration". PhD thesis. University of London, 1995.

[76] P. D. Floyd and J. L. Merz. "Effects of Impurity-free and Impurity-induced Disordering on the Optical Properties of GaAs/(Al,Ga)As Distributed Bragg Reflectors". In: *Journal of Applied Physics* 76.9 (1994), pp. 5524–5527.

[77] Joachim Piprek, ed. *Optoelectronic Devices: Advanced Simulation and Analysis*. New York: Springer, 2005.

[78] Jinhui Wang, Ioannis Savidis, and Eby G. Friedman. "Thermal Analysis of Oxide-Confined VCSEL Arrays". In: *Microelectronics Journal* 42.5 (2011), pp. 820–825.

[79] Yun Fei Liu et al. "Droplet-Shaped-Mesa Vertical-Cavity Surface-Emitting Laser Arrays with Narrow Linewidth and Small Beam Divergence". In: *Journal of Lightwave Technology* (2025), pp. 1–6.

[80] Yanhong Ma et al. "Phase-Locking Dynamics of a 2D VCSEL Hexagonal Array with an Integrated Talbot Cavity". In: *Optics Express* 30.6 (2022), p. 9892.

[81] Nasibeh Haghighi et al. “19-Element Vertical Cavity Surface Emitting Laser Arrays with Inter-Vertical Cavity Surface Emitting Laser Ridge Connectors”. In: *Journal of Physics: Photonics* 2.4 (2020), 04LT01.

[82] Elham Heidari et al. “Hexagonal Transverse-Coupled-Cavity VCSEL Redefining the High-Speed Lasers”. In: *Nanophotonics* 9 (2020), p. 437.

[83] William North et al. “Modal Characteristics of Coupled Vertical Cavity Surface Emitting Laser Diode Arrays”. In: *Journal of Applied Physics* 132.17 (2022), p. 173102.

[84] Hamed Dalir and Fumio Koyama. “High-Speed Operation of Bow-Tie-Shaped Oxide Aperture VCSELs with Photon–Photon Resonance”. In: *Applied Physics Express* 7.2 (2014), p. 022102.

[85] Erik Haglund et al. “High-Power Single Transverse and Polarization Mode VCSEL for Silicon Photonics Integration”. In: *Optics Express* 27.13 (2019), pp. 18892–18899.

[86] Kevin P. Pikul et al. “Utilization of Silicon Optical Coatings for Transverse-Mode Suppression in High-Power Oxide-Confined Vertical-Cavity Surface-Emitting Lasers”. In: *Applied Physics Letters* 126.20 (2025), p. 201107.

[87] Jingfei Mu et al. “5.3 mW at 80°C, Single-Mode High-Power 795 Nm VCSEL Achieved Solely through Intracavity Design”. In: *Optics Express* 33.11 (2025), p. 23865.

[88] Hans Wenzel et al. “Novel 900 Nm Diode Lasers with Epitaxially Stacked Multiple Active Regions and Tunnel Junctions”. In: *Electronics Letters* 57.11 (2021), pp. 445–447.

[89] Xingyuan Gan et al. “GaAs Tunnel Junction Grown Using Tellurium and Magnesium as Dopants by Solid-State Molecular Beam Epitaxy”. In: *Japanese Journal of Applied Physics* 53.2 (2014), p. 021201.

[90] Yoshihiro Akahane et al. “High-Q Photonic Nanocavity in a Two-Dimensional Photonic Crystal”. In: *Nature* 425.6961 (2003), pp. 944–947.

[91] Ansas Kasten et al. “Manufacturable Photonic Crystal Single-Mode and Fluidic Vertical-Cavity Surface-Emitting Lasers”. In: *Selected Topics in Quantum Electronics, IEEE Journal of* 14 (2008), pp. 1123–1131.

[92] Paul Leisher, Joshua Sulkin, and Kent Choquette. “Parametric Study of Proton-Implanted Photonic Crystal Vertical-Cavity Surface-Emitting Lasers”. In: *Selected Topics in Quantum Electronics, IEEE Journal of* 13 (2007), pp. 1290–1294.

[93] N. Yokouchi, A.J. Danner, and K.D. Choquette. “Two-Dimensional Photonic Crystal Confined Vertical-Cavity Surface-Emitting Lasers”. In: *IEEE Journal of Selected Topics in Quantum Electronics* 9.5 (2003), pp. 1439–1445.

[94] Microchemicals. *Spin-Coating of Photoresists*. Application Note.

[95] *Inductively Coupled Plasma - Reactive Ion Etching (ICP-RIE) — Corial*. https://corial.plasmatherm.com/en/technologies/icp-rie-inductively-coupled-plasma-reactive-ion-etching.

[96] Valerio Flavio Gili. “All-Dielectric Nonlinear Nanophotonics”. PhD thesis. 2018.

[97] Samuel Shutts. *Faster Feedback Refines VCSEL Production - News*. compoundsemiconductor.net.

[98] H. C. Casey, D. D. Sell, and K. W. Wecht. “Concentration Dependence of the Absorption Coefficient for N- and P-type GaAs between 1.3 and 1.6 eV”. In: *Journal of Applied Physics* 46.1 (1975), pp. 250–257.

[99] Björn Stuhrmann. “Self-Organized Active Biopolymer Networks in Migrating Living Cells”. PhD thesis. 2009.

[100] A. Piotrowska. “Ohmic Contacts to GaAs: Fundamentals and Practice”. In: *Acta Physica Polonica A* 84.3 (1993), pp. 491–504.

[101] Y. Feng et al. “A Study on the Law of Oxidation Rate in GaAs-based VCSELs”. In: *Optik* 125.18 (2014), pp. 5124–5127.

[102] K.D. Choquette et al. “Advances in Selective Wet Oxidation of AlGaAs Alloys”. In: *IEEE Journal of Selected Topics in Quantum Electronics* 3.3 (1997), pp. 916–926.

[103] B. E. Deal and A. S. Grove. “General Relationship for the Thermal Oxidation of Silicon”. In: *Journal of Applied Physics* 36.12 (1965), pp. 3770–3778.

[104] Pei-Cheng Ku and C.J. Chang-Hasnain. “Thermal Oxidation of AlGaAs: Modeling and Process Control”. In: *IEEE Journal of Quantum Electronics* 39.4 (2003), pp. 577–585.

[105] Ray D. Twesten, David M. Follstaedt, and Kent D. Choquette. “Microstructure and Interface Properties of Laterally Oxidized AlxGal-xAs”. In: *Vertical-Cavity Surface-Emitting Lasers*. Vol. 3003. SPIE, 1997, pp. 56–62.

[106] Gareth J Michell. “Characterisation and Advanced Applications of the Steam Oxidation of AIGaAs”. PhD thesis. Cardiff University, 2010.

[107] Robert Fabbro et al. “In-Situ Observation of Lateral AlAs Oxidation and Dislocation Formation in VCSELs”. In: *Micron* 158 (2022), p. 103264.

[108] J. Houska et al. “Overview of Optical Properties of Al2O3 Films Prepared by Various Techniques”. In: *Thin Solid Films* 520.16 (2012), pp. 5405–5408.

[109] S J Gillgrass et al. “Impact of Thermal Oxidation Uniformity on 150 Mm GaAs- and Ge-substrate VCSELs”. In: *Journal of Physics D: Applied Physics* 56.15 (2023), p. 154002.

[110] Majid Riaziat, David Reed, and Alex Kor. “Controlling the Parameters of Wet Lateral Oxidation for VCSEL Fabrication”. In: *Vertical-Cavity Surface-Emitting Lasers XX*. Vol. 9766. SPIE, 2016, pp. 87–95.

[111] V. Van Tuyen et al. “On the Study of Electrical Isolation of Multi-Layer GaAs Planar Doped Barrier Diode Structures by Proton Bombardment”. In: *The 10th IEEE International Symposium on Electron Devices for Microwave and Optoelectronic Applications*. Manchester, UK: IEEE, 2002, pp. 311–315.

[112] James F. Ziegler, M. D. Ziegler, and J. P. Biersack. “SRIM – The Stopping and Range of Ions in Matter (2010)”. In: *Nuclear Instruments and Methods in Physics Research Section B: Beam Interactions with Materials and Atoms*. 19th International Conference on Ion Beam Analysis 268.11 (2010), pp. 1818–1823.

[113] H. Boudinov, A. V. P. Coelho, and J. P. de Souza. “Electrical Isolation of P-Type GaAs Layers by Ion Irradiation”. In: *Journal of Applied Physics* 91.10 (2002), pp. 6585–6587.

[114] *Pulse Testing of Laser Diodes and Vertical Cavity Surface Emitting Lasers*. Tech. rep. Tektronix.

[115] Markus Daubenschuz. “Simplified Determination of the Thermal Resistance of Vertical-Cavity Surface-Emitting Lasers”. In: ().

[116] F. T. Albeladi et al. “Multi-Mode Interference Reflector Based InAs-QD Laser”. In: *2022 28th International Semiconductor Laser Conference (ISLC)*. 2022, pp. 1–2.

[117] C Hentschel et al. “Gain Measurements on VCSEL Material Using Segmented Contact Technique”. In: *Journal of Physics D: Applied Physics* 56.7 (2023), p. 074003.

[118] Łukasz Chorchos, Nikolay N. Ledentsov, and Jarosław P. Turkiewicz. “850 Nm Multiaperture Vertical Cavity Surface Emitting Lasers: Equivalent Circuit Modeling, Intrinsic Response, Transmission Performance and Comparison to Standard VCSEL Design”. In: *Journal of Lightwave Technology* 43.9 (2025), pp. 4331–4337.

[119] Si-Cong Tian et al. “Novel Energy-Efficient Designs of Vertical-Cavity Surface Emitting Lasers for the next Generations of Photonic Systems”. In: *Japanese Journal of Applied Physics* 61.SK (2022), SK0801.

[120] William North et al. “Analysis and Characterization of Photon-Photon Resonance in Coupled Dual-Element Photonic Crystal Vertical Cavity Surface Emitting Laser Arrays”. In: *Journal of Lightwave Technology* (2023), pp. 1–7.

[121] Nasibeh Haghighi, Philip Moser, and James A. Lott. “Power, Bandwidth, and Efficiency of Single VCSELs and Small VCSEL Arrays”. In: *IEEE Journal of Selected Topics in Quantum Electronics* 25.6 (2019), pp. 1–15.

[122] Nusrat Jahan et al. “Analysis of Supermode Dynamics of Coherent Dual-Element Photonic Crystal VCSEL Arrays”. In: *2022 IEEE Photonics Conference (IPC)*. 2022, pp. 1–2.

[123] Fansheng Meng et al. “High Power Multi-Junction 808 Nm Vertical Cavity Surface Emitting Lasers With High Efficiency”. In: *IEEE Photonics Technology Letters* 36.24 (2024), pp. 1489–1492.

[124] Nusrat Jahan, William North, and Kent D. Choquette. “Low Divergence Triangular Coupled VCSEL Array”. In: *2022 28th International Semiconductor Laser Conference (ISLC)*. 2022, pp. 1–2.

[125] Nusrat Jahan and K. D. Choquette. “Supermode Analysis and Characterization of Triangular Vertical Cavity Surface Emitting Laser Diode Arrays”. In: *IEEE Photonics Journal* (2023), pp. 1–7.

[126] Chun-Yen Peng et al. "Performance Analyses of Photonic-Crystal Surface-Emitting Laser: Toward High-Speed Optical Communication". In: *Nanoscale Research Letters* 17.1 (2022), p. 90.

[127] Meng Xun et al. "Nineteen-Element in-Phase Coherent Vertical-Cavity Surface-Emitting Laser Array with Low Side Lobe Intensity". In: *Optics Express* 27.2 (2019), pp. 774–782.

[128] Tatsushi Hamaguchi et al. "Spontaneously Implemented Spatial Coherence in Vertical-Cavity Surface-Emitting Laser Dot Array". In: *Scientific Reports* 12.1 (2022), p. 21629.

[129] Chia-Jui Chang et al. "Design of Low-Threshold Photonic-Crystal Surface-Emitting Lasers with Confined Gain Regions by Using Selective Area Intermixing". In: *Discover Nano* 18.1 (2023), p. 134.

[130] K.B. Kahen. "Two-Dimensional Simulation of Laser Diodes in the Steady State". In: *IEEE Journal of Quantum Electronics* 24.4 (1988), pp. 641–651.

[131] Markus-Christian Amann. *WSI Research Groups.* https://www.wsi.tum.de.

[132] Jack Baker et al. "Quick Fabrication of 940nm Emitting VCSEL Arrays for Commercial Wafer Characterization". In: *Vertical-Cavity Surface-Emitting Lasers XXV*. Vol. 11704. International Society for Optics and Photonics, 2021, p. 1170408.

[133] Kow-Ming Chang, Jung-Yu Tsai, and Chun Yen Chang. "New Physical Formulation of the Thermionic Emission Current at the Heterojunction Interface". In: *IEEE Electron Device Letters* 14.7 (1993), pp. 338–341.

[134] *Semiconductors and Semimetals.* 1967.

[135] Prashant Misra and J. Nagaraju. "Electrical Contact Resistance in Thin Gold Plated Contacts: Effect of Gold Plating Thickness". In: *IEEE Transactions on Components and Packaging Technologies* 33.4 (2010), pp. 830–835.

[136] R. Jones and S. Oberg. "Theory of Si Donor-Acceptor Complexes in GaAs". In: *Semiconductor Science and Technology* 9.12 (1994), p. 2291.

[137] Allan W. Snyder and John D. Love. *Optical Waveguide Theory.* Boston, MA: Springer US, 1984.

[138] P. Bienstman and R. Baets. “Optical Modelling of Photonic Crystals and VCSELs Using Eigenmode Expansion and Perfectly Matched Layers”. In: *Optical and Quantum Electronics* 33.4 (2001), pp. 327–341.

[139] Botao Zhang, David W. Snoke, and Albert P. Heberle. “Towards the Transverse Mode-Locking of Oxide-Confined VCSELs”. In: *Optics Communications* 285.20 (2012), pp. 4117–4119.

[140] V. G. Garcia and M. Farzaneh. “Transient Thermal Imaging of a Vertical Cavity Surface-Emitting Laser Using Thermoreflectance Microscopy”. In: *Journal of Applied Physics* 119.4 (2016), p. 045105.

[141] Xiangwei Zhang et al. “A Thermal Analysis of Stable-Polarization VCSELs”. In: *Optik* 157 (2018), pp. 203–207.

[142] M. Sugimoto et al. “Very Low Threshold Current Density in Vertical-Cavity Surface-Emitting Laser Diodes with Periodically Doped Distributed Bragg Reflectors”. In: *Electronics Letters* 28.4 (1992), pp. 385–387.

[143] Tao Fan and Artem R. Oganov. “AICON: A Program for Calculating Thermal Conductivity Quickly and Accurately”. In: *Computer Physics Communications* 251 (2020), p. 107074.

[144] J. Yvonnet et al. “A General and Efficient Computational Procedure for Modelling the Kapitza Thermal Resistance Based on XFEM”. In: *Computational Materials Science*. Proceedings of the 19th International Workshop on Computational Mechanics of Materials 50.4 (2011), pp. 1220–1224.

[145] Phil Diesing, David Gardell, and David Audette. “Liquid Interface at Wafer Test”. In: *Semiconductor Wafer Test Conference*. 2005.

[146] W L Johnson, R Balasubramaniam, and R Grotenrath. “Analysis of Heat Transfer from a Local Heat Source at Cryogenic Temperatures”. In: *IOP Conference Series: Materials Science and Engineering* 1240.1 (2022), p. 012013.

[147] Rajendra Karwa. *Heat and Mass Transfer*. Springer Nature, 2020.

[148] Doyeol Ahn and Shun-Lien Chuang. “Optical Gain in a Strained-Layer Quantum-Well Laser”. In: *IEEE Journal of Quantum Electronics* 24 (1988), pp. 2400–2406.

[149] Kazushige Horio and Hisayoshi Yanai. “Numerical Modeling of Heterojunctions Including the Thermionic Emission Mechanism at the Heterojunction Interface”. In: *IEEE Transactions on Electron Devices* 37.4 (1990), pp. 1093–1098.

[150] W. Nakwaski. “Principles of VCSEL Designing”. In: *Opto-Electronics Review* 16.1 (2008), pp. 18–26.

[151] Matthias Streiff. “Opto-Electro-Thermal VCSEL Device Simulation”. PhD thesis. ETH Zurich, 2004, 157 S.

[152] Andreas Hangauer, Jia Chen, and Markus-Christian Amann. “Vertical-Cavity Surface-Emitting Laser Light–Current Characteristic at Constant Internal Temperature”. In: *IEEE Photonics Technology Letters* 23.18 (2011), pp. 1295–1297.

[153] *Multi-Junction VCSEL Arrays.* lumentum.com.

[154] Jack Baker et al. “Thermal Performance of 940 Nm AlGaAs-Based VCSELs Grown on Germanium”. In: *IEEE Photonics Journal* 17.2 (2025), pp. 1–4.

[155] T.R. Jervis, D.W. Woodard, and L.F. Eastman. “Effects of Ion Implantation on Deep Levels in GaAs”. In: *Electronics Letters* 15.20 (1979), pp. 619–621.

[156] N. I. Klyui et al. “Effect of H+ Implantation on the Optical Properties of Semi-Insulating GaAs Crystals in the IR Spectral Region”. In: *Semiconductors* 51.3 (2017), pp. 305–309.

[157] T.D. Visser et al. “Confinement Factors and Gain in Optical Amplifiers”. In: *IEEE Journal of Quantum Electronics* 33.10 (1997), pp. 1763–1766.

[158] Chih-Sheng Chang and Shun Lien Chuang. “Modeling of Strained Quantum-Well Lasers with Spin-Orbit Coupling”. In: *IEEE Journal of Selected Topics in Quantum Electronics* 1.2 (1995), pp. 218–229.

[159] Prashant P. Baveja et al. “Assessment of VCSEL Thermal Rollover Mechanisms from Measurements and Empirical Modeling”. In: *Optics Express* 19.16 (2011), pp. 15490–15505.

[160] M.S Torre and C Masoller. “Effects of Carrier Transport on the Transverse-Mode Selection of Index-Guided Vertical-Cavity Surface-Emitting Lasers”. In: *Optics Communications* 202.4-6 (2002), pp. 311–318.

[161] C. Degen et al. “Transverse Modes in Thermally Detuned Oxide-Confined Vertical-Cavity Surface-Emitting Lasers”. In: *Physical Review A* 63.2 (2001), p. 023817.

[162] Feng Zhang et al. “Large Oxide Aperture High-Beam-Quality Vertical-Cavity Surface-Emitting Laser Array with Center Vertical Injection”. In: *Optics & Laser Technology* 193 (2026), p. 114310.

[163] Guanzhong Pan et al. “Harnessing the Capabilities of VCSELs: Unlocking the Potential for Advanced Integrated Photonic Devices and Systems”. In: *Light: Science & Applications* 13.1 (2024), p. 229.

[164] Yi-Yang Xie et al. “Low Threshold Current Single-Fundamental-Mode Photonic Crystal VCSELs”. In: *IEEE Photonics Technology Letters* 24.6 (2012), pp. 464–466.

[165] Matěj Hejda et al. “Spiking Behaviour in Laterally-Coupled Pairs of VCSELs With Applications in Neuromorphic Photonics”. In: *IEEE Journal of Selected Topics in Quantum Electronics* 29.2: Optical Computing (2023), pp. 1–10.

[166] Valerio Torrelli et al. “High-Power Emission via Large-Area VCSELs with Single High-Order Mode Operation”. In: *IEEE Photonics Journal* (2024), pp. 1–8.

[167] Dongyue Jin et al. “Thermal Design of VCSEL Arrays for Optical Output Power Improvement”. In: *IEEE Transactions on Electron Devices* 69.7 (2022), pp. 3761–3767.

[168] Riccardo Rurali et al. “The Thermal Boundary Resistance at Semiconductor Interfaces: A Critical Appraisal of the Onsager vs. Kapitza Formalisms”. In: *Physical Chemistry Chemical Physics* 20.35 (2018), pp. 22623–22628.

[169] Safoura Nayeb Sadeghi, Sangyeop Lee, and Keivan Esfarjani. “THERMACOND, a Code to Compute Lattice Thermal Conductivity from Harmonic and Anharmonic Force Constants”. In: *npj Computational Materials* 11.1 (2025), p. 303.